Development of Adsorbents for Selective Volatile Organic Compounds Removal from Diluted Gas Streams

PAR

Guillaume Bastien BAUR

Choisissez un travail que vous aimez et vous n'aurez pas à travailler un seul jour de votre vie.

Confucius

Remerciements

Au cours des quatre années nécessaires à la réalisation de ma thèse, en plus d'approfondir mes connaissances scientifiques, j'ai eu l'occasion de rencontrer différentes personnes qu'il est maintenant temps de remercier.

Mes remerciements vont tout d'abord à Prof. Lioubov Kiwi-Minsker, ma directrice de thèse, pour m'avoir accepté dans son laboratoire. Son soutien et ses conseils notamment rédactionnels m'ont été très précieux.

Je tiens à remercier Philip Morris pour avoir proposé un sujet de recherche et l'avoir soutenu financièrement. Plus particulièrement je souhaite remercier Gaëtan Couderc pour avoir orienté ma recherche et m'avoir donné l'opportunité de présenter oralement mes résultats au sein de Philip Morris.

Je remercie aussi les membres de mon comité de thèse à savoir la présidente du jury, Prof. Sandrine Gerber, ainsi que les rapporteurs, Prof. Jeremy Luterbacher, Prof. Antonio Palomares Gimeno et Dr. Gaëtan Couderc pour le travail de relecture effectué ainsi que pour les corrections suggérées.

Mes remerciements s'adressent également à Prof. Albert Renken pour sa curiosité scientifique, nos discussions ainsi que pour l'aide fournie pour certaines modélisations.

Abstract

Contamination of the environment by anthropogenic volatile organic compounds (VOC) became of major concern during the last decades. Present in gas streams of many industrial exhaust systems, they are harmful and detrimental for both human health and the environment even at low concentration. Several techniques have been developed and applied for VOC abatement, e.g.: absorption, condensation, bio-filtration, photo-, thermal or catalytic oxidation. Although good performances were reported, they suffer from different drawbacks such as low efficiency at diluted concentration, difficult handling or low throughput. In this sense adsorption appears to be the most efficient method for complete removal of VOC from diluted streams.

Various adsorbents were developed for VOC abatement such as activated carbon (AC), zeolites, silica or polymers. Although their efficiencies for certain VOC was shown, their abatement capacities can be reduced due to the lack of specific interactions. The approach taken in this thesis is based on the development of specific adsorbents towards VOC. The surface of commercial adsorbents is functionalized depending on the VOC physical properties aiming to create specific interactions.

Activated carbon is a widely used adsorbent and received great attention for VOC removal due to their low cost and versatility. Because of their well-developed microporosity AC show large abatement capacity for non-polar VOC such as benzene or toluene even at low

concentration. Generally used in the form of granules, powder or pellets, AC can present mass transfer limitations and flow mal-distribution (preferential gas passage or bypass through the adsorbent bed). To circumvent these drawbacks, activated carbon fibers (ACFs) consisting of arranged microfilaments are used in this work.

First, the adsorption of toluene, as a model of non-polar high boiling point VOC, was studied over ACFs. The influence of the ACFs microporosity on the toluene adsorption capacity was addressed using two samples with different microporosity but similar surface chemistry. The influence of the pore size on the enthalpy of adsorption was evaluated through the modelling of adsorption isotherms measured experimentally. The adsorption enthalpy was also evaluated using simulation of toluene temperature-programmed desorption (TPD). The values obtained from isotherms and TPD methods were then compared. Besides morphology, surface chemistry is known to influence the VOC adsorption capacity of ACFs. The influence of the surface oxygen content on the toluene and the acetaldehyde removal capacity was then evaluated. The increased concentration of O-containing groups reduces toluene adsorption whereas it promotes the acetaldehyde removal.

Specific functionalization of the ACFs surface was performed for the removal of polar VOC represented by formaldehyde and acetaldehyde. Taking advantage of their large specific surface area, ACFs were functionalized by diethylene triamine (DETA) via liquid layer deposition. ACFs with different DETA loading were synthesized and their adsorption capacity towards formaldehyde was evaluated. The influence of DETA loading on the adsorption capacity was measured and an adsorption mechanism was suggested.

The deposition of nano-particles (NPs) of basic metal oxide on the ACFs surface was used for increased acetaldehyde abatement. By combining the high intrinsic adsorption capacities of metal oxide NPs and the large specific surface area of ACFs, an effective

acetaldehyde adsorbent was synthesized. The influence of the MgO loading was evaluated as well as the effect of CO_2 in the adsorptive mixture. Finally, based on the TPD pattern, a mechanism of adsorption was suggested

In the last step, zeolites were used as adsorbents for the removal of butadiene, a model of low boiling point non polar VOC. The surface of commercial zeolites was modified aiming at the creation of specific adsorption sites. The surface was characterized and specific sites for butadiene adsorption were suggested based on an *in situ* FTIR study. The thermodynamic parameters of adsorption were calculated through the modelling of experimentally measured adsorption isotherms. The butadiene adsorption enthalpy obtained was compared to the value obtained by TPD methods.

Keywords: Adsorption, VOC, activated carbon fibers, zeolites, surface functionalization

Version Abrégée

La pollution de l'environnement par des composés organiques volatiles (COV) de source anthropogénique est devenue une problématique récurrente au cours des dernières dizaines d'années. Présents dans les effluents gazeux de nombre d'industries, les COV sont nocifs pour la santé humaine et dangereux pour l'environnement même à basses concentrations. Plusieurs procédés ont été développés pour la réduction de leurs émissions : l'absorption, la condensation, l'oxydation thermique, catalytique ou par plasma. Bien que de bonnes performances aient été reportées pour ces procédés, certaines limitations subsistent comme leurs efficacités à basse concentration, l'utilisation à l'échelle industrielle ou le faible débit d'effluents gazeux traité par unité de temps. L'adsorption apparaît donc comme une méthode efficace pour l'élimination totale des COV dilués. De nombreux adsorbants comme le charbon actifs, les zéolites, la silice ou certains polymères ont été développés pour le contrôle des émissions de COV. Bien que leur efficacité ait été démontrée, leur capacité d'adsorption peut être considérablement réduite selon le type de COV notamment à cause du manque d'interactions spécifiques entre les COV et l'adsorbant. Cette thèse est donc portée sur le développement d'adsorbant spécifique pour COV. La surface d'adsorbants commerciaux a été modifiée en fonction des propriétés physique du COV avec pour objectif de créer des interactions spécifiques.

Le charbon actif est un adsorbant largement utilisé dans le traitement des COV à cause de son bas coût de production et de sa polyvalence. Grâce à sa microporosité, le charbon actif

possède une grande capacité d'adsorption envers les COV apolaires comme le toluène ou le benzène même à basse concentration. Le charbon actif est généralement utilisé sous forme de granule ou de fine poudre pouvant ainsi créer des pertes de charge ou des phénomènes de transfert de masse menant à des limitations cinétique du procédés. Afin de palier à ces désavantages, des fibres de carbone activées sont utilisées dans cette thèse.

Dans un premier temps, l'adsorption de toluène, un COV apolaire à haut point d'ébullition, sur les fibres de carbone activées a été étudiée. L'influence de la microporosité sur l'adsorption du toluène a été menée en utilisant deux fibres de carbone activée présentant une chimie de surface similaire mais une microporosité différente. L'influence de la taille moyenne des pores sur l'enthalpie d'adsorption a été évaluée par le biais d'isothermes d'adsorption ainsi que de leurs modélisations. L'enthalpie d'adsorption du toluène a aussi été calculée sur la base de mesures expérimentales de désorption avec rampe de température qui furent par la suite simulées. Les valeurs obtenues selon les deux méthodes ont été comparées. A part leur morphologie, la chimie de surface des adsorbants peut aussi influencer la capacité d'adsorption des COV. L'influence des groupes oxygène contenu à la surface des fibres de carbone activées sur la capacité d'adsorption du toluène et de l'acétaldéhyde a été mesurée en utilisant des fibres contenant un nombre variable de groupes oxygène. Alors qu'une influence positive de la concentration d'oxygène à la surface des fibres a été remarquée pour l'acétaldéhyde, une diminution de la capacité d'adsorption du toluène a été mesurée.

L'introduction de fonctionnalités spécifiques à certain COV a été menée pour l'adsorption du formaldéhyde et de l'acétaldéhyde représentants les COV polaires. Les fibres de carbone activées ont été fonctionnalisées au moyen d'une déposition d'un film liquide de diéthylènetriamine (DETA). L'influence du DETA sur l'adsorption du formaldéhyde a été étudiée en variant la quantité de DETA déposé et un mécanisme d'adsorption est suggéré.

La déposition sur les fibres de carbone activées de nanoparticules (NPs) d'oxyde de métaux a été utilisée pour l'adsorption de l'acétaldéhyde. En combinant le haut potentiel d'adsorption des NPs d'oxyde de métaux à la grande surface spécifique des fibres de carbone activées, un adsorbant efficace envers l'acétaldéhyde a été synthétisé. L'influence de la quantité d'oxyde de magnésium ainsi que l'effet du CO_2 dans le flux gazeux a été évalué. Finalement un mécanisme d'adsorption basé sur la désorption avec rampe de température a été suggéré.

La dernière partie de ce travail de recherche est orientée sur le développement d'un adsorbant pour le butadiène. La surface de zéolites commerciales a été modifiée avec pour objectif la création de site d'interaction spécifique. La caractérisation de la surface de cet adsorbant a permis de suggérer des sites d'adsorption. Les paramètres thermodynamiques d'adsorption ont été calculés à partir des isothermes mesurées expérimentalement. Ces valeurs ont été comparées à celle obtenue par la méthode de désorption avec rampe de température.

Mots-clés : Adsorption, COV, fibres de carbone activées, fonctionnalisation de surface

Contents

List of Symbols

Abbreviations

AAS	Atomic absorption spectroscopy
AC	Activated carbon
ACF	Activated carbon fibers
CSTR	Continuous stirred tank reactor
EDX	Energy dispersive X-ray spectroscopy
DETA	Diethylene triamine
FTIR	Fourier transformed infrared spectroscopy
IR	Infrared spectroscopy
HRSTEM	High resolution scanning transmission electron microscopy
MOF	Metal-organic framework
MAS NMR	Magic angle spinning nuclear magnetic resonance
NMR	Nuclear magnetic resonance
NP	Nano-particle
PFR	Plug flow reactor
SEM	Scanning electron microscopy
SSA	Specific surface area

STP	Standard temperature and pressure	
TPD	Temperature-programmed desorption	
VOC	Volatile organic compound	
XPS	X-ray photoelectron spectroscopy	
XRD	X-ray diffraction	

Greek symbols

β	Affinity coefficient	[-]
γ	Temperature ramp	[K min^{-1}]
δ	thermal expansion coefficient of the saturation concentration	[K^{-1}]
Θ	Normalized time $\left(t/\overline{t}\right)$	[-]
θ	Fractional loading	[-]
ν	Liquid molar volume	[cm^3 mol^{-1}]
σ^2	Variance	

Roman symbols

ΔH_{ads}^{0}	Standard enthalpy of adsorption	[kJ mol^{-1}]
ΔH_{vap}	Enthalpy of vaporization	[kJ mol^{-1}]
A	Polyani adsorption potential	[-]
a	graphical area	[-]
C	BET constant	[-]
C$_{\%(w/w)}$	Mass adsorption capacity	[-]
c	Concentration	[mol m^{-3}]
D	Dispersion coefficient	[m^2 s^{-1}]

d_p	Pore diameter	[nm]
E_0	Characteristic energy of adsorption	[kJ mol^{-1}]
k_d	Kinetic constant of desorption	[s^{-1}]
$k_{d,0}$	Frequency factor	[-]
F	Normalized concentration	[-]
K	Langmuir adsorption constant	[Pa^{-1}]
L	Reactor length	[m]
M	Molar mass	[g mol^{-1}]
m	Order of reaction	[-]
$m_{adsorbent}$	Mass of adsorbent	[g]
N	Exponent of the D-A equation	[-]
n	Number of moles	[mol]
p	Pressure	[Pa]
p_0	Saturation pressure	[Pa]
q	Adsorption capacity	[mol kg^{-1}]
R	Gas constant	[J mol^{-1} K^{-1}]
R_d	Desorption rate	[mol g^{-1} s^{-1}]
T	Temperature	[K]
t	Time	[s]
$\bar{t}$	Mean residence time	[s]
u	Linear velocity	[m s^{-1}]
V	Volume	[cm^3]
V_m	Monolayer volume	[cm^3]
W	Adsorption capacity	[cm^3 g^{-1}]
Z	Adsorbed concentration	[mol g^{-1}]

Subscripts

ads	Adsorbed
in	At the inlet
L	Langmuir
max	Maximum
non-ads	Non-adsorbed
out	At the outlet
Tol	Toluene
tot	Total

1 Introduction

This introductory chapter presents a brief overview of the thesis. The subject is formulated underlying the main motivations and objectives of this research project. The structure of the thesis is also outlined.

1.1 Motivation and Objectives

Volatile organic compounds (VOC) are pollutants often encountered in industrial gas emissions. They are defined by the European council as compounds having a vapor pressure of 0.01 kPa or more at 293 K. Their release is subjected to legal limits due to their toxicity and their impact on the environment [1].

Although several VOC abatement strategies have been developed, adsorption is a widely used technique in industry, particularly for diluted streams [2]. In the last century the development of efficient adsorbent became of great importance and the first industrial companies producing activated carbon and zeolite were founded in 1911 and 1956 respectively [3]. Nowadays, modern technologies allow controlling the morphology and the chemistry of activated carbon [4] and zeolites [5] improving their adsorption capacities.

This thesis deals with the issues encountered during the adsorption of VOC. The efficiency of the adsorbent strongly depends on the VOC physical properties such as polarity and boiling point. Non-polar high boiling point VOC can be efficiently adsorbed on activated carbon due to its wide microporous structure. Different interactions are created in the micropores because of the identical chemical properties of non-polar VOC and activated carbon. However, much lower adsorption capacities are reported for lower boiling point VOC or polar ones due to the lack of interactions rendering the removal of such compounds particularly challenging.

The removal of polar VOC is generally achieved by rendering the original hydrophobic activated carbon surface more hydrophilic. This surface tuning allows the creation of hydrogen bonding between the polar adsorbate and the hydrophilic surface groups. Although large increase of the adsorption capacity is usually reported with this type of surface

functionalization, it remains lower than for non-polar VOC. Moreover the hydrophilic surfaces create interactions with all type of polar compounds including water.

The creation of specific adsorption sites is then required for the selective removal of polar or low boiling point VOC. Metal oxide nanoparticles have shown promising adsorption capacities with polar compounds such as ketones or aldehydes. However, it is very difficult to handle NPs as adsorbent in practical cases due to high pressure drop created during gas passage. Functionalization of activated carbon surface by nitrogen groups is another well-known technique for increase of aldehyde removal. The efficiency of nitrogen groups has been established but limited adsorption capacities were reported due to their low density on the activated carbon surface.

Besides activated carbon, zeolites represent valuable adsorbents due their well-developed crystalline structure presenting large microporosity. Surface acid sites creation can be easily achieved by ion exchange providing potential adsorption specific sites. Another type of adsorption sites could be obtained by transition metal-exchanged zeolite.

Hence the present work aims at developing efficient adsorbents with particular surface tuning for removal of VOC at low concentrations. The removal of different VOC such as toluene, acetaldehyde, formaldehyde and butadiene is studied over activated carbon fibers and zeolites. The ultimate goal is to maximize the adsorption capacity towards all these VOC. The strategy used for adsorbent development is focused on the creation of particular adsorbent-adsorbate interactions by modification of the surface properties of a commercial adsorbent. The final adsorbents should present large adsorption capacity and avoid strong mass transfer limitations or pressure drop.

1.2 Structure of the Work

In **Chapter 2**, the current state of the art in the field of VOC adsorption is reviewed. **Chapter 3** presents the procedure used for preparing the studied adsorbent as well as the characterization techniques employed throughout this work. The experimental setup developed for this project and the method used for calculating of the adsorption capacity are also presented in details.

Effect of ACFs morphology and surface chemistry on toluene and acetaldehyde adsorption

Chapter 4 presents the removal of toluene, chosen as a model of non-polar high boiling point VOC, on ACFs. Two different ACFs possessing different pore size and similar surface chemistry were tested. The effect of the ACFs morphology on toluene removal is studied via adsorption isotherms and temperature-programmed desorption (TPD). Based on the data obtained an adsorption mechanism is suggested and thermodynamic parameters calculated.

The ACFs surface chemistry being another important parameter for VOC adsorption, its effect on the removal of two types of VOC, toluene and acetaldehyde, chosen as model for polar VOC, is studied in **Chapter 5**. The morphology remains constant whereas the surface chemistry is modified to different extents by oxidative treatment. The effect of the oxidative treatment on toluene and acetaldehyde is evaluated and explained by the surface oxygen content.

Creation of specific sites on ACFs for formaldehyde and acetaldehyde adsorption

The surface of ACFs can be modified with specific functional groups for the creation of specific adsorbent-adsorbate interactions. **Chapter 6** presents the functionalization of ACFs surface by deposition of nitrogen containing groups. The removal of diluted formaldehyde,

representing polar low boiling point VOC, is studied over diethylene triamine (DETA) deposited on ACFs. The effect of the DETA amount on the formaldehyde adsorption capacity is studied as well as the adsorbent stability upon storage. Finally a mechanism of interactions between DETA and formaldehyde is suggested.

Chapter 7 reports the development of metal oxide functionalized ACFs for acetaldehyde adsorption. Metal oxide NPs were deposited on ACFs in order to combine the intrinsic adsorption capacity of the metal oxide NPs and the favorable macro-structure of the ACFs. The adsorption capacity towards acetaldehyde was evaluated for several metal oxide NPs and compared to the performance of oxidized ACFs (**Chapter 5**). Competitive adsorption with CO_2 was also carried out. Based on the TPD pattern different adsorption sites were identified.

Zeolite as specific adsorbent for butadiene

Butadiene is a non-polar low boiling point VOC. Because of its high volatility, butadiene adsorption in ACFs micropore is not efficient. Therefore, the use of zeolite as an adsorbent for butadiene is studied in **Chapter 8**. Specific adsorbate-adsorbent interactions involving the butadiene double bonds are presented. A detailed *in situ* FTIR study of butadiene adsorption is applied to gain insight on the adsorption mechanism. Butadiene adsorption isotherms and TPD experiments were carried out to obtain the thermodynamic parameters of adsorption.

Finally **Chapter 9** summarizes the results obtained throughout this study and presents the general conclusions and outlooks.

2 State of the Art

This chapter presents the current state of research in the field of fluid-solid adsorption. The first part is focused on the principles of adsorption with the description of the different adsorption isotherms. The second part is devoted to the main methods used for VOC removal with particular focus on adsorption. The influence of activated carbon porosity and surface chemistry for selective VOC removal is discussed. Chemisorption of VOC on zeolite and metal oxide nano-particles is also presented.

2.1 Adsorption: General Definitions and Terminology

Adsorption is a thermodynamically favorable phenomenon occurring at the interface of fluid and solid. It is defined as the enrichment of the solid surface by the fluid phase [6]. Adsorption depends on the size of the interfacial area. Therefore, the solid, called 'adsorbent', is usually highly porous with a large specific surface area. The counterpart of the adsorbent is the 'adsorbate'. The adsorbate is defined as the material in the adsorbed state whereas the 'adsorptive' is the adsorbable substance in the fluid phase. Depending on the nature of the adsorptive and the adsorbent, the temperature and the fluid phase composition, a considerable adsorbate concentration on the solid surface can be encountered. The term 'desorption' denotes the inverse of the adsorption process. Although solid-liquid [7] and solid-gas [8-10] interfaces are contained in the definition of adsorption only the solid-gas system is studied and presented in this thesis.

2.1.1 Definitions

The thermodynamic equilibrium between the amount adsorbed and its bulk phase concentration at constant temperature is defined as 'adsorption isotherm'.

The term 'surface area' is defined as the surface available for a certain adsorptive under specific conditions. It is generally referred on the mass of adsorbent and represents the specific area of the interface between gas and solid. Most of the solid adsorbents used in industrial applications have a large specific surface area. This is achieved through a complex porous structure consisting of pores of various shapes and width.

The pores are usually classified by the IUPAC in three groups according to their width. Micropores are defined as pores width smaller than 2 nm, mesopores are pores of 2-50 nm width and macropores represent pores with a diameter larger than 50 nm. Recently the

micropores were subdivided in ultramicropores $d_p < 1$ nm and supermicropores, d_p 1-2 nm [11].

Adsorption phenomenon occurring by interactions between the solid and the adsorptive can result either from van der Waals interaction and are defined as 'physisorption' or it can have properties closer to chemical bonding and are called 'chemisorption'. Physisorption can be compared to a condensation process of the adsorptive with a relatively low degree of adsorbent specificity. At high relative pressure, multilayer adsorption generally occurs. The identity of the adsorbed molecule is conserved and it returns to the fluid phase without transformation during desorption. The energy involved in a physisorption process is usually on the order of magnitude of the heat of condensation of the adsorptive although an appreciable enhancement can be observed during physisorption in micropores. Physisorption is always exothermic. On the opposite, chemisorption leads to monolayer coverage formed by interactions with specific adsorption sites. Chemisorbed molecules 'react' with the adsorbent and their desorption in the original form is usually not possible.

Table 2.1 Terms and definitions

Term	Definition
Adsorption	Enrichment of the solid surface by a fluid compound
Adsorbate	Substance adsorbed at the gas-solid interface
Adsorptive	Substance in the fluid phase
Physisorption	Adsorption without specific chemical bonding
Chemisorption	Adsorption with specific chemical bonding
Surface area	Extent of surface accessible to the probe molecule under given conditions
Pore	Cavity or channel in a solid
Micropore	Pore of internal width < 2 nm
Mesopore	Pore of internal width between 2 and 50 nm
Macropore	Pore of internal width > 50 nm
Ultramicropore	Pore of internal width < 1 nm
Supermicropore	Pore of internal width between 1 and 2 nm

2.1.2 Adsorption Isotherms

The amount of gas adsorbed on a solid surface depends on its pressure in the bulk phase, temperature and the nature of the gas-solid interaction with a dynamic equilibrium. The adsorption isotherm is defined as the relation between the amount adsorbed per unit of mass and the equilibrium pressure at given temperature:

$$n/m_{adsorbent} = f\left(p/p_0, T\right) \tag{1.1}$$

Adsorption isotherms usually have characteristic shapes. These shapes are important since they provide information about the pore structure of the adsorbent. The IUPAC classification proposes 6 characteristic isotherm shapes (**Figure 2.1**) [12].
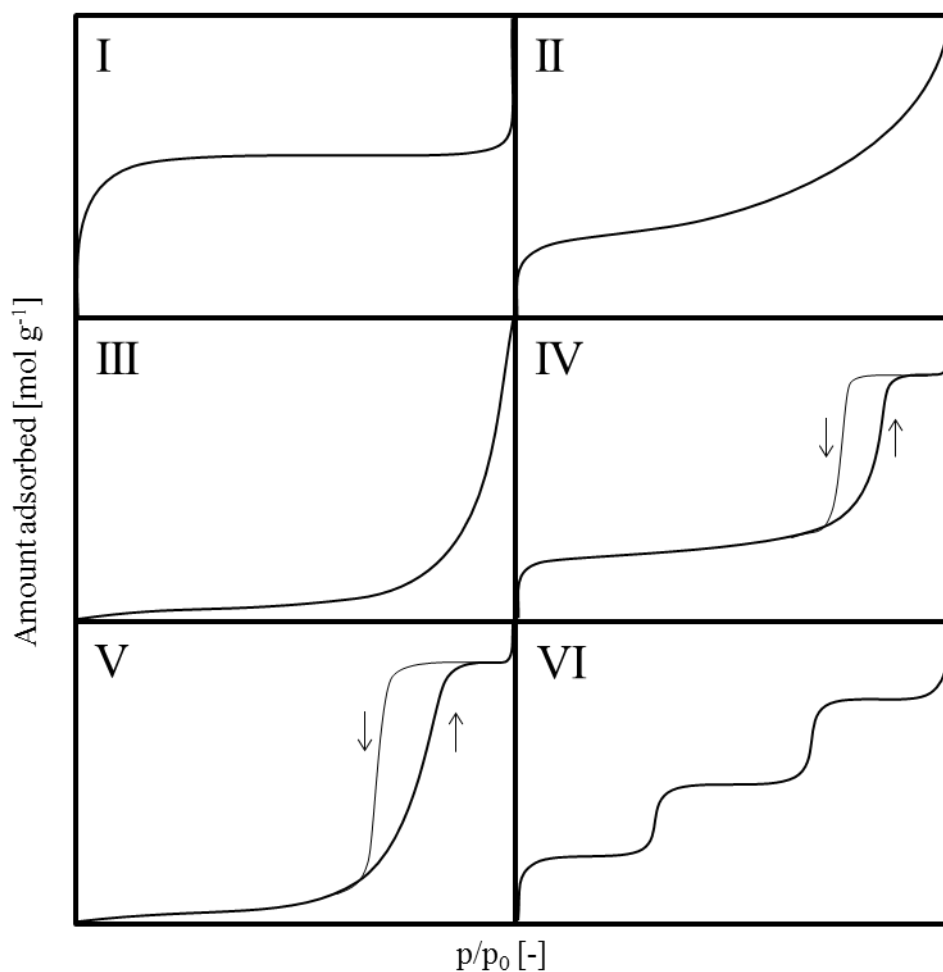
Figure 2.1 Classification of vapor adsorption isotherms

The type I isotherm is reversible and rises steeply at low relative pressure to reach a plateau signifying that the pores of the adsorbent are completely filled. Such isotherm is obtained with microporous adsorbent. Adsorbent-adsorbate interactions are enhanced in the

micropores due to the proximity of both pore walls. A decrease of the micropore width leads to a decrease of the relative pressure at which the micropore filling occurs.

The type II isotherm is concave to the p/p_0 axis. The amount adsorbed increases steeply at low partial pressure and then a moderate slope is observed until saturation. Such isotherm shape is obtained with a macroporous material where multilayer adsorption occurs. The knee of the isotherm, defined as the slope change at low partial pressure, represents the monolayer capacity.

The type III isotherm represents an adsorbate-adsorbent system with weak interactions on a macroporous solid

The type IV and V isotherms are obtained with mesoporous adsorbents. Type IV and type V isotherms have a shape related to type II and type III isotherms respectively although they exhibit a hysteresis loop. The lower branch of the isotherm is obtained during the adsorption (increase of the partial pressure) whereas the upper branch during desorption. The hysteresis loop is associated to the filling and emptying of the mesopores, called capillary condensation.

The type VI isotherm is known as a stepwise isotherm. It is associated to a layer-by-layer adsorption on a highly uniform surface.

The IUPAC classification was determined for ideal porous structure. However, in many cases the adsorbent has a complex nature rendering the interpretation of the isotherm obtained experimentally more difficult.

2.2 Removal of VOC by Conventional Methods

Volatile organic compounds (VOC) are common air pollutants encountered in industrial gas emissions [13]. They are toxic and environmentally detrimental even at low concentrations [1, 14, 15]. Because of the toxicity, their emission is subjected to legal limits [16]. Therefore, numerous VOC control strategies have been developed during the last century [2, 17].

Many different methods are available for VOC emission control [18]. Among them, thermal oxidation, catalytic and plasma oxidation [19-21], or bio-filtration [22, 23] are destructive ones whereas absorption [24], condensation, adsorption or membrane separation are considered as recovery ones. Thermal oxidation is carried out at high temperature (1100-1300 K) for 200 to 5000 ppmv VOC concentration range [25]. It is therefore energetically costly and not efficient for diluted streams (< 100 ppmv). Catalytic oxidation systems burn VOC similarly to thermal oxidation. The catalyst allows decreasing the combustion temperature and the VOC concentration range [21, 26] but total destruction of VOC into CO_2 and H_2O is generally not achieved [27]. Plasma oxidation systems have been also extensively studied for VOC removal [28-30]. However it is difficult to handle in practical cases and the formation of CO as a by-product renders this technology less environmental-friendly [31]. The use of bio-filtration for low concentration VOC abatement was also studied and high efficiency was reported at laboratory scale [32-34]. However, this technology is sensitive to concentration variation and high removal efficiencies cannot be achieved under variable VOC concentration [35]. Therefore the amount of bacteria in the bio-filter has to be constantly adjusted to the amount of VOC. Finally this technology requires a long residence time (1-3 min) which is a major drawback for practical applications [36].

Unlike destructive VOC abatement techniques, the recovery ones allow possible re-use of the VOC thereby valorizing them. Condensation is one of the well-known industrial techniques. It is efficient for VOC with boiling point above 300 K at high concentration (5000 ppmv). Although the recovered product is directly usable with this technology, the efficiency of this method is not greater than 80 % [25]. The recovery of more diluted or low-boiling VOC requires considerable cooling increasing drastically the operating costs.

Absorption, consisting of VOC transfer from a gas phase to a liquid solvent, also known as scrubbing, is extensively used in industry [37-39]. The VOC transfer takes place in an absorber tower designed to enhance the mass transfer [40]. Such a process is governed by the vapor liquid equilibrium. Recently, novel ionic liquid solvents were developed for absorption purpose and larger VOC affinity towards ionic liquids was reported [41]. Despite interesting results obtained at laboratory scale, ionic liquids remain expensive and therefore VOC concentration above 500 ppmv is suggested for efficient recovery process [42].

The recovery of VOC by membrane based separation such as gas permeation has been studied during the last decades [43, 44]. Various membranes were developed and their efficiency was mostly tested in a relatively high VOC concentration range (1000-10000 ppmv) [45, 46]. Despite good results reported, this technology is considered as a slow process with high cost associated with the permeation membrane. Moreover, no results were reported for VOC concentration below 1000 ppmv.

In summary, all recovery methods are efficient at VOC concentration larger than 1000 ppmv except adsorption. This technology is efficient for low VOC concentration and was developed in the second part of the 20th century for exhaust gas cleaning [47] using novel microporous adsorbents (zeolites, activated carbons, alumina, silica gels, polymeric adsorbent) [48]. VOC abatement by adsorption is based on the affinity between the VOC and

the adsorbent surface [8] and requires high specific surface area. Hence adsorbents usually present a well-developed porosity [49].

2.3 VOC Removal by Adsorption

Due to an increasing demand on VOC control technologies, development of adsorbents for VOC removal has been an important research subject during the last decades and the interest to this topic is still very high. The increase of adsorbent capacity, the understanding of the adsorption mechanism and the synthesis of selective adsorbents are the main objectives in this research field. The key to a successful adsorbent design is to combine adsorption sites specific towards the targeted VOC while keeping a high microporosity necessary for large adsorption capacity.

2.3.1 Role of Adsorbent Porosity

Porosity Characterization

Since adsorption is a surface phenomenon, the porosity of the adsorbent is a crucial parameter for high adsorption efficiency. Porous structures are present in different crystalline materials such alumino-silicate, zeolite or metal organic framework (MOFs) which are constituted of metal atoms connected by organic linkers [50, 51]. Amorphous porous structures are also of interest for gas adsorption, particularly activated carbons [52] and polymers [53, 54].

An important parameter of porous materials is their specific surface area. It is commonly calculated from the Brunauer-Emmett-Teller (BET) equation [55]. This equation is applied to the experimental isotherm of nitrogen adsorption on the material at 77 K [56, 57]. Experimentally the N_2 adsorption capacity is measured at different partial pressures until saturation. At a certain partial pressure depending on the porosity of the material, a N_2

monolayer is assumed by the model. By knowing the area of a nitrogen molecule and the monolayer amount adsorbed by the material, the specific surface area is calculated.

Although N_2 as a probe molecule for specific surface area measurement is widely used [58], adsorption of other gases such as argon [59] or carbon dioxide [60, 61] was also carried out. The same surface area range is usually obtained despite that slightly different results were reported [62]. Further characterization of porous material includes the type of porosity and the pore size distribution. Different types of porous structure are identified for VOC adsorbents: mesoporous and microporous materials [63]. These two types of porosity are identified by different N_2 isotherm shape [12].

The pore size is determined by more complex calculations using the adsorptive isotherm. In the case of mesoporous solid, the pore size distribution is usually determined by computing the nitrogen isotherm adsorption data with the BJH [64] or the Dollimore and Heal model [65] assuming capillary condensation in the mesopores. The pore size distribution of microporous material could be determined using the Horvath and Kawazoe (H-K) method [66]. This model relates the amount adsorbed at a given partial pressure to a micropore radius using the Lennard-Jones potential. However, since the nature of the adsorbent-adsorbate interactions are not taken into account for the pore size estimation, the reliability of the H-K method is limited [67]. Developed recently, density functional theory (DFT) is a powerful tool for the estimation of the pore size distribution in microporous structure [68, 69] but requires consequent computational tools [70].

Developed in the sixties, the α_s-method is another technique applied for pore size distribution determination [71, 72]. The α_s-plot is based on the comparison of the N_2 adsorption isotherms between a chemically similar non-porous reference adsorbent and the studied porous material [73]. Normalizing the N_2 amount adsorbed onto the nonporous

reference at different partial pressure by the amount adsorbed at $p/p_0 = 0.4$ gives the α_s reference. The amount adsorbed onto the studied adsorbent is then plotted against α_s at the corresponding relative pressure. Depending on the shape of the α-plot, the porosity of different samples can be compared [74]. In this way a semi-quantitative description of the pore structure is obtained [75]. This microporosity assessment technique was successfully applied for activated carbon [76, 77] and silica [78]. An example of an α_s-plot coupled with adsorption data is shown in **Figure 2.2**.
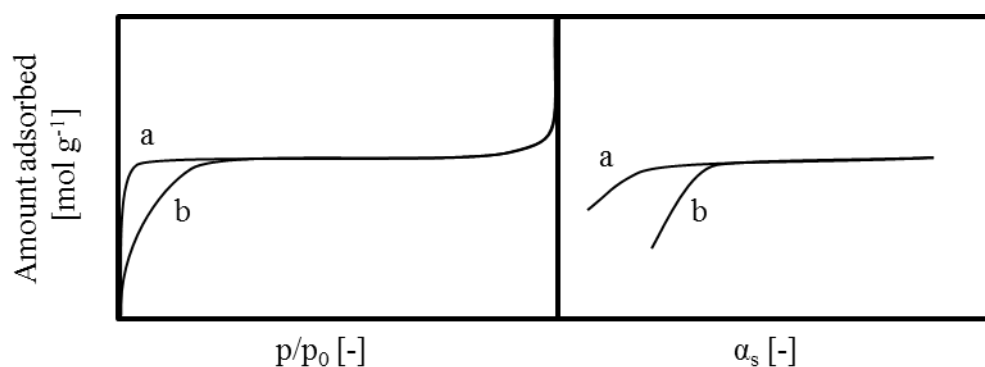
Figure 2.2 Example of α_s-plot for a sample with ultramicropores (a) and supermicropores (b)

The difference between material with ultramicropores (a) and supermicropores (b) is depicted in **Figure 2.2** as an example. Ultramicroporous adsorbent shows a constant adsorption capacity at lower partial pressure than supermicroporous material signifying complete filling of the ultramicropore at lower partial pressure (left part). The right part of **Figure 2.2** is the α_s-plot. As can be seen, the difference between the two microporous material is more evident. The curve slope change appears at different α_s values. Similarly to the adsorption graph a lower curve slope change is associated to narrower micropores.

Advantages of Microporosity

The effect of pore size on the VOC removal capacity was studied extensively over different mesoporous and microporous adsorbents such as silica [79], zeolite [80], polymers [81] and activate carbon [82, 83]. At high VOC relative pressure, large adsorption capacities were reported for mesoporous material taking advantage of a considerable pore volume of the adsorbent [84]. However, at lower VOC partial pressure, an increased adsorption capacity along with a mean pore diameter decrease was reported while comparing different mesoporous silica for toluene and benzene removal [85]. Similar results were reported for *n*-hexane on MCM-41 due to enhanced adsorbent-adsorbate interactions in the narrower pores at low *n*-hexane pressure [86]. Another study comparing the removal capacity of *n*-hexane and benzene over mesoporous (MCM-41) and microporous (activated carbon, Y zeolite and silicalite-1) showed a considerably higher adsorption capacity of the microporous adsorbent at low adsorptive partial pressure [87]. Since VOC are generally emitted at low partial pressure [85], efficient removal can only be achieved by microporous adsorbents such as zeolite or activated carbon [88].

Activated carbon can be used as adsorbent in several forms like granules, pellets, powders or fibers [89, 90]. Among them, activated carbon fibers (ACFs) consisting of microfilaments with high specific surface area, present smaller mass transfer limitations and lower pressure drop as compared to the other types of activated carbon [91, 92].

2.3.2   Adsorption by Activated Carbon: Microporosity

Numerous publications report microporous adsorbents as promising material for VOC removal at low concentration [93, 94]. The effect of the micropore size, the specific surface area and the total pore volume on the VOC removal capacity was studied for adsorbent optimization [95]. Activated carbon (AC) was extensively studied since it presents tunable

microporosity properties depending on the synthesis and the activation procedure [96-99]. Lillo-Ródenas *et al.* studied the effect of the micropore size for benzene and toluene adsorption on AC and activated carbon fibers (ACFs) [100, 101]. They noticed that the adsorption capacity for these two VOC was increasing with micropore volume and specific surface area. Moreover, a linear correlation between the VOC adsorption capacity and the narrow micropore volume ($d_p < 0.7$ nm) obtained by CO_2 adsorption at 273 K was reported. The authors concluded that the narrow micropores are effective for toluene and benzene removal at 200 ppmv.

The porous structure of AC was also studied for ethanol removal at 250 ppmv by Silvestre-Albero *et al.* [102]. They reported an increased adsorption capacity with the micropore volume up to a maximum before a decrease. This result was explained by a widening of the micropores when increasing the microporosity during the activation of the AC. They concluded that the total micropore volume governs the adsorption capacity along with the mean micropore size.

A comparative study of the adsorption capacity of ACFs with different microporosity towards *n*-butane at 50 ppmv revealed a larger abatement by the ACFs with the lower pore volume and the smaller micropore size [103]. At higher *n*-butane concentration (5000 ppmv), higher adsorption capacity of the ACFs with the larger micropore volume was reported. Such an inversion of the adsorption capacity for a given compound was referred to as a crossover regime. Similar results were obtained by Mangun *et al.* for the adsorption of light *n*-alkanes (methane to pentane) over ACFs with different pore size and micropore volume [104]. Depending on the VOC boiling point, the crossover regime is reached at different VOC partial pressure. For the lighter VOC, the crossover regime appears at high partial pressure, while for higher boiling point VOC, it takes place at extremely low partial pressure.

Finally Huang *et al.* tried to formalize and predict the adsorption capacity of a microporous adsorbent by developing an equation based on the pore size, the maximum adsorption capacity, the adsorbate partial pressure and a structural factor depending on the adsorbate properties [105]. However the structural factor is not clearly defined and is not predictable for a given adsorbate rendering this model difficult to use.

2.3.3   Adsorption by Activated Carbon: Surface Chemistry

Numerous publications reported the adsorption of a wide range of VOC over microporous adsorbents. However, depending on the VOC physical properties, the performance achieved by the adsorbent is extremely variable [106]. High adsorption capacity can be reached by activated carbon towards non-polar high boiling point VOC such as toluene [107], whereas much lower adsorption capacity was reported for acetone or acetaldehyde [108, 109]. In the case of activated carbon the hydrophobic properties of the micropore walls favor the interactions with chemically similar VOC such as benzene, toluene or long chain alkanes. The adsorption is governed by interactions of π-electron rich region of the graphene layers and the aromatic rings [110, 111].

The strategy commonly adopted for the removal of polar VOC is to modify the surface properties of AC in order to favor interactions with the adsorptive [112]. Commonly oxygen containing groups created by means of oxidative treatment in gas or liquid phase is performed [113]. A large number of functionalities present on the AC surface are schematically depicted in **Figure 2.3**.
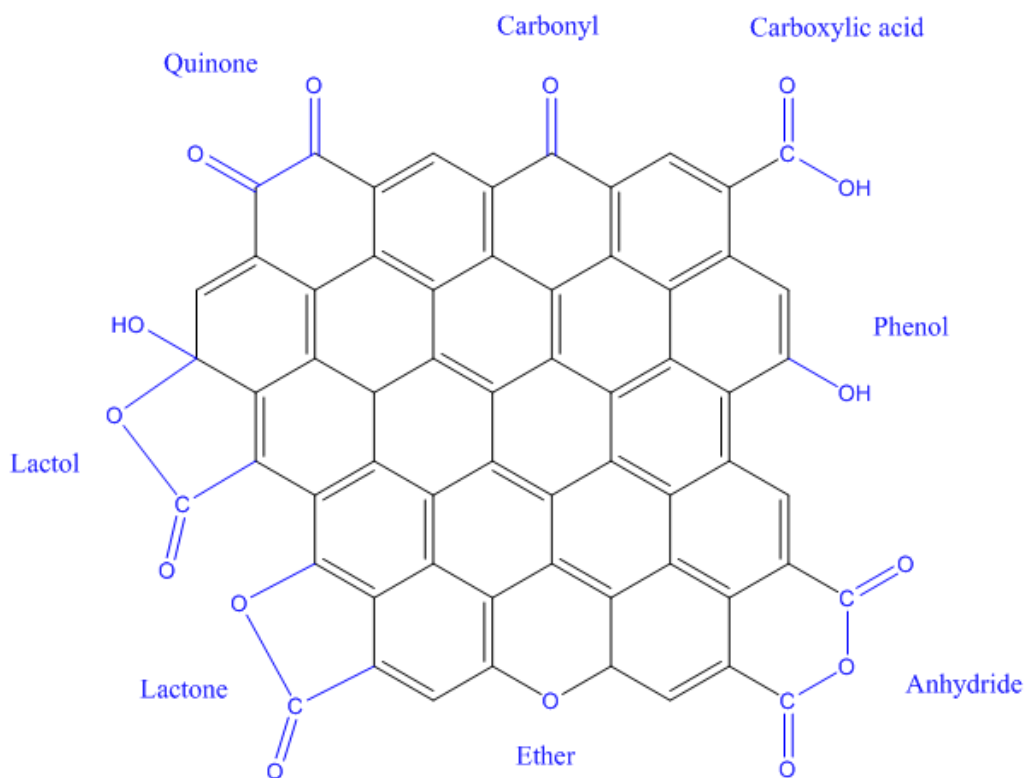
Figure 2.3 Oxygen surface functional groups

These oxygen functionalities were first characterized by titration methods [114]. Carboxylic, anhydride, lactones, lactol and phenol are considered as acidic groups whereas carbonyl and ether are neutral or slightly basic [115]. The identification of functional groups was also obtained qualitatively by infrared spectroscopy (IR) [116] whereas *in situ* X-Ray photoelectron spectroscopy (XPS) coupled with temperature-programmed desorption (TPD) [117, 118] can provide quantitative information on individual functional groups.

Although oxidative treatment of AC leads to the formation of different surface oxygen groups, depending on the oxidative agent their proportion may vary. Nitric acid oxidation leads mainly to the formation of carboxylic groups [119] whereas oxidation under diluted oxygen favors the creation of anhydride and lactone groups [117]. Hydrogen peroxide was also reported as a carbon oxidative agent [120, 121] as well as ammonium persulfate [122].

The removal of the oxygen functionalities can be achieved by heat treatment in an inert gas [123]. The effect of oxidative treatment on the carbon microporosity was studied showing both increase [117] and decrease [124, 125] of the specific surface area and the mean pore size.

The presence of oxygen functional groups on the AC surface for polar VOC removal was studied by several research groups [121, 126, 127]. Adsorption of acetone and ammonia on H_2SO_4/HNO_3 treated ACFs was reported with a significant increase upon oxidation whereas ACFs treated by H_2O_2 did not increase the acetone removal capacity [124]. Methanol removal efficiency over AC was increased upon oxidation by ammonium persulfate $(NH_4)_2S_2O_8$ for low methanol partial pressure, whereas at high partial pressure, the largest adsorption capacity was achieved by the ACs with the largest pore volume regardless of the surface chemistry [128]. Three different AC treated by nitric acid oxidation were studied for acetaldehyde removal [129]. In every case, the removal capacity was increased due to the hydrophilic surface obtained by the addition of oxygen functional groups. Variation of the adsorption enthalpy of acetaldehyde was also observed upon surface oxidation due to the creation of hydrogen bonding between oxygen containing groups and the aldehyde group. Finally a comparative study of polar and non-polar VOC removal over nitric acid treated ACF was reported by Dimotakis and co-workers [106]. An increase of acetone and acetaldehyde removal was noticed for oxidized fibers whereas lower adsorption was observed for benzene. Similarly to El-Sayed and Bandosz [129], the creation of specific chemical interactions was suggested to increase the adsorption capacity in the low pressure range for both acetone (25-1000 ppmv) and acetaldehyde (50-500 ppmv).

Besides O-containing groups, the presence of nitrogen functional groups on the carbon surface can create specific adsorption sites [130]. Several procedures were reported for the creation of such functional groups. The introduction of nitrogen functional groups on

activated carbon can be carried out by using an ACFs precursor composed partially by nitrogen [131]. The presence of pyrrolic and pyridinic nitrogen functional groups was reported using such precursor. The influence of N-functional groups on the adsorption of formaldehyde was addressed and a higher removal was observed for the N-functionalized ACFs.

Another method developed for the introduction of nitrogen containing groups on carbon surface consists of the formation of nitro group by carbon oxidation followed by a reduction to the amino group [132]. The oxidation step is usually carried out with nitric acid whereas several methods exist for the reduction step such as treatment with sodium hydrosulfite ($Na_2S_2O_4$) and ammonia [133], hydrochloric acid and iron mixture [134] or ammonia at high temperature [135]. The development of amine groups on the carbon surface was reported to increase the removal capacity of phenol, nitrous oxide and formaldehyde because of the strong adsorption potential of the amino groups.

The direct addition of nitrogen functional groups on ACFs by heat treatment in ammonia was developed by Mangun *et al.* [136] and Economy *et al.* [137]. A significant increase of the ACFs basic properties and a higher removal of HCl were observed with the addition of amino groups. Boudou used similar method to functionalize ACFs for SO_2 and H_2S removal and reported higher adsorption capacity due to basic groups creation [138]. Although the ACFs microporosity was kept, both authors reported a small increase of the mean pore size upon high temperature ammonia treatment. Addition of functional nitrogen groups on AC by urea impregnation followed by heat treatment was reported to create additional adsorption centers for acetaldehyde and hydrogen sulfide removal [130, 139]. Lower adsorption enthalpies of acetaldehyde on N-functionalized ACFs as compared to original material confirmed the other type of adsorption sites.

Another strategy developed for carbon surface functionalization is the deposition of a liquid layer on the carbon surface [140]. Several studies report the efficiency of this type of adsorbent for formaldehyde [141] and acetaldehyde removal [142]. Acetaldehyde adsorption on aminobenzoic acid modified AC was addressed [142]. A larger adsorption capacity was reported and aldehyde condensation over the acid group to form crotonaldehyde followed by a reaction between the aldehyde and the amine group was suggested. Ma *et al.* deposited hexamethylene diamine via vapor condensation to functionalize activated carbon for formaldehyde removal at low concentration [141]. The authors reported a large increase of the modified AC capacities compared to the original one. However, at high hexamethylene diamine loading, the formaldehyde removal capacity was reported to decrease due to pore blocking.

The functionalization of other supports with amine groups was also carried out for the removal of aldehyde [143]. Higher formaldehyde adsorption capacity was measured over functionalized silica supports (MCM-41 and SBA-15) as compared to their original counterparts using grafted 3-aminopropyltrimethoxysilane [144, 145]. 3-aminopropylethoxysilanes was also used to functionalize graphite oxide [146]. The amine-functionalized material showed a higher adsorption capacity as compared to non-functionalized material [147]. The formation of a Schiff base between the amine and the aldehyde group was suggested.

In conclusions, the addition of oxygen containing groups on the AC surface is an important strategy for increasing its hydrophilic character. Addition of oxygen functionalities by means of liquid or gaseous oxidative treatment increases the removal of polar VOC at low concentration demonstrating the importance of the adsorbent surface chemistry. The addition of nitrogen functionalities on the AC surface was achieved by several methods. The functionalities are either chemically bonded or supported on the surface. In both cases an

aldehyde removal enhancement is reported via the amine-aldehyde group interactions. The use of other nitrogen functionalized supports for aldehyde removal was also reported.

2.3.4   Adsorption by Metal Oxides

Unlike activated carbon where physisorption usually occurs, specific chemical bonds can be created between the VOC and the adsorbate for its removal [148]. Such specific interactions are generally achieved with metal oxides [149]. Adsorption of a wide range of VOC such as sulfur dioxide, hydrogen sulfide or ammonia was reported over metal oxides. The metal oxide can be used either as bulk [150] or supported [151] adsorbents. Enhanced adsorption capacity is reported for porous metal oxide nanocrystals with high specific surface [152, 153].

Porous magnesium oxide (MgO) prepared from aerogels was reported as efficient adsorbent for a large number of VOC such as methanol, ethanol and butanol at low partial pressures [154] or sulfur dioxide [155]. They showed a well-developed porosity and a small particle size. A comparison of the sulfur dioxide surface occupancy between commercial MgO powder and aerogels nanocrystals showed a higher occupancy of the latter suggesting specific adsorption sites on the edges and the corners of the nano-crystals. The adsorption of other VOC such as acetaldehyde, acetone, propionaldehyde and benzaledehyde on the same MgO adsorbent was also studied [156]. Higher adsorption capacity as compared to commercial MgO and AC was systematically reported. A dissociative acetaldehyde adsorption mechanism through the interaction of the carbonyl group with the surface sites was suggested.

Porous nanocrystals of CuO and NiO were synthesized for carbon tetrachloride and sulfur dioxide removal [157]. A destructive adsorption of carbon tetrachloride was reported on both CuO and NiO at high temperature. As compared to commercial particles, a larger

adsorption capacity was observed. Multilayer adsorption of SO_2 was reported on porous nanocrystals whereas only a monolayer was observed on commercial nano-particles indicating a higher intrinsic activity of the porous particles.

Jeevanandam *et al.* reported the selective removal of thiophenes from a hydrocarbon stream on Ag nano-particles supported on aluminum oxide [151]. The authors suggested the creation of Lewis acid sites through the silver nano-particles deposition. The comparison of the thiophene adsorption capacity revealed a 10-fold increase upon nano-particles deposition. Desulfurization of the hydrocarbon stream is suggested to occur via a π-complexation mechanism between the Ag^+ ions and the thiophene aromatic ring. In such a complexation mechanism, the cation forms σ bonds with its empty *s* orbital and its *d* orbital back-donates electron density to the antibonding (π*) orbitals of the thiophene ring [158]. Similarly the dispersion of CuCl on Na-X zeolite was reported for separation of olefin and paraffin mixtures [159]. A π-complexation adsorption mechanism is also suggested between the olefin and the adsorbent whereas no specific interactions are created with the paraffin.

The use of activated carbon fibers (ACFs) as a metal oxide support for ammonia and hydrogen sulfide adsorption was reported by Le Leuch *et al.* [160]. The deposition of Fe, Cu and Zn oxides, known for ammonia and hydrogen sulfide combustion, on ACFs was achieved and a comparative study of their removal capacity was carried out. Larger adsorption capacity towards hydrogen sulfide was reported for Cu oxide modified ACFs whereas Fe oxide modified ACFs was more efficient for ammonia removal. In both cases the adsorption capacity was found to be larger as compared to original ACFs.

In conclusions, the use of metal oxide nano-particles is a valuable alternative to common adsorbents such as activated carbon, zeolite or silica for VOC removal. To be efficient the metal oxide should present a very small size and a large porosity since corner and

edge sites are generally reported as adsorption sites. Unlike activated carbon where a physisorption mechanism is observed, metal oxide based adsorbents present chemisorption mechanism. Supported metal oxide nano-particles were also reported and can be considered as valuable adsorbents.

2.3.5   Zeolites as Adsorbents

Zeolites are microporous crystalline aluminosilicate structures. They generally show lower adsorption capacity as compared to activated carbon due to a lower total pore volume and a smaller specific surface area. However, they possess a tunable surface chemistry because of a negatively charged framework and a positively charged counter ion. Cation exchange can lead to the creation of specific adsorption sites. The presence of Lewis or Brønsted acid sites can also enhance adsorption capacity towards specific VOC.

The removal of sulfur containing compounds in petroleum refining streams such as aromatic thiophene or thiophene derivatives received great interest since new regulation appeared in several countries [158]. Their removal in liquid phase over metal exchanged zeolite was reported as very efficient and selective due to specific interactions with the exchanged metal [161]. Increased adsorption capacity was reported using Cu [162] and Ag-exchanged [163] cations. A π-complexation mechanism was suggested. For comparison the performance of activated carbon was evaluated in similar conditions and a lower adsorption capacity was reported confirming the importance of specific interactions that can be created with metal exchanged zeolites [164]. Other transition metal exchanged zeolite such as Ni and Zn were synthesized for sulfur compounds removal and specific interactions involving π-complexation were suggested [165, 166]. Velu *et al.* reported the efficiency of Ce-exchanged Y zeolite for thiophene removal without involving a π-complexation mechanism [167]. A higher adsorption capacity as compared to Ni exchanged zeolites was observed.

Separation of aromatic molecules from aliphatic ones by adsorption over zeolites was also investigated. Preferential interactions of aromatic molecules with the zeolite counter ion were reported for Na-Y and Ca-Y [168]. Stronger interactions were observed for divalent cations as compared to monovalent ones. An adsorption mechanism through interactions of benzene with both cation (Na^+ or Ca^{2+}) and oxygen atom of the framework was suggested [169]. The effect of the zeolite framework Al content on the removal capacity of aromatic compounds was studied and stronger interactions were reported for zeolite with low Si/Al ratio [169-171]. The selective removal of aromatic compounds via a π-complexation mechanism was proposed by Takahashi *et al.* [172]. A comparison of the adsorption potential of Ag-exchanged zeolites towards benzene and cyclohexane was carried out. Cyclohexane adsorption enthalpy over Na-Y and Ag-Y was identical whereas an increased adsorption enthalpy was reported for benzene on Ag-Y as compared to Na-Y indicating the importance of π-complexation in the removal of aromatic compounds.

Ag-X exchanged zeolite was reported as a promising adsorbent for olefin removal [173]. A π-complexation mechanism is suggested to occur between the olefin and the adsorbent. Original Na-X zeolites was used by Da Silva and Rodriguez for an adsorptive separation of light olefins from paraffin [174]. A 10-fold larger selectivity towards propylene was reported despite the absence of a π-complexation adsorption mechanism.

The removal of trichloroethylene over zeolites has created considerable interest over the last decade [175, 176]. The increase of the Si/Al ratio of the zeolite via dealumination was reported to increase its hydrophobicity due the formation of a hydrophobic siloxane surface [177, 178]. Guillemot *et al.* studied the influence of the dealumination level on the adsorption of trichloroethylene and concluded that medium dealumination (Si/Al ~17) was the most appropriate [179]. The influence of the counter ion at similar Si/Al ratio was analyzed by

Pires *et al.* and higher trichloroethylene adsorption capacity was reported for the acidic form of the zeolite (H^+ form) [180].

The separation of dienes from olefins has also found considerable interest in the petrochemical research. Similar to aromatic compounds, the electron density of the double bonds was considered to be involved in π-complexation mechanism. Ag and Cu(I) exchanged zeolites were reported as efficient adsorbents for butadiene removal due their ability for π-complexation [181]. The Ag content did not influence the butadiene amount adsorbed [182]. Hence, two possible π-complexation forms for butadiene with either one Ag^+ or two Ag^+ were suggested. Butadiene from liquid phase was also adsorbed over zeolite exchanged with transition metal polycations consisting of 0.4 to 1.6 nm nanoparticles [183]. The use of Mn, Cu and Zn was reported also aiming at a π-complexation mechanism with butadiene [184]. A mixed transition metal polycation cluster of Cu and Mn was reported as the most efficient. A π-complexation followed by a polymerization on the Brønsted acid sites was suggested as an adsorption mechanism.

In conclusions, zeolites are versatile adsorbents and were used towards a large number of compounds. Surface tuning can be carried out as:

- Zeolite exchange with a transition metal for π-complexation

- Dealumination for hydrophobic surface and Lewis site creation

- Counter ion exchange with hydrogen

- Transition metal polycations cluster

2.4 Conclusions

Adsorption is one of the most efficient methods for VOC removal at low concentration without energy consumption. The choice of the adsorbent depends on the nature of the VOC. Microporosity and surface chemistry has been identified as the key parameters for efficient VOC removal.

Activated carbon is therefore a valuable adsorbent because of its adjustable microporosity and versatility towards surface functionalization. For high boiling point VOC, microporous AC with a large pore volume is the most efficient. For lower boiling point VOC, AC with ultramicroporosity presents the highest capacity due to enhanced interaction with the pore walls. Efficient removal of polar VOC is usually achieved by the addition of oxygen or nitrogen functional groups on the AC surface.

Besides AC, zeolite and metal oxide nano-particles are efficient adsorbents. Metal oxide nano-particles can create specific interactions with VOC particularly on the edge and the corner sites whereas in transition metal exchanged zeolites, aromatics, thiophenes, olefins and dienes can be chemisorbed via different mechanism.

3 Experimental

In this chapter the raw materials used during the research project are listed and the syntheses of the adsorbents are presented in details. All the characterization techniques are also discussed. Finally, the experimental setup used for adsorption experiments is described including the calculations methods.

3.1 Materials

3.1.1 Activated Carbon Fibers

Original ACFs

Activated carbon fibers (ACFs) were purchased from by Kynol Europa GmbH (Hamburg, Germany). They are produced from Kynol novoloid (phenolic) precursor fibers by a one-step process combining both carbonization and chemical activation by water and/or CO_2. Two types of the fibers were used, namely: ACF-1 (SSA ~ 1000 m^2 g^{-1}) and ACF-2 (SSA ~ 2000 m^2 g^{-1}).

3.1.2 Modified ACFs

Oxidized ACFs

The oxidized ACFs were prepared by an immersion of original ACFs in a boiling 15% (v/v) aqueous solution of nitric acid (HNO_3 65% vol., VWR chemicals, AnalaR NORMAPUR) for different times (1, 15, 30 and 75 min) followed by a rinsing with demineralized water and drying in ambient air. The abbreviations for the samples are as following: ACF-2/HNO_3-30m means the ACF-2 sample treated by HNO_3 for 30 minutes.

Amines Functionalized ACFs

The ACFs were modified by deposition of a diethylenetriamine (DETA) (99% Sigma-Aldrich) via wetness impregnation. In a standard procedure, the fibers are dipped into a solution of DETA in ethanol (> 99.8% Fluka). The DETA concentrations were calculated using the ACFs wetness capacity to obtain several loadings. The impregnated fibers were then dried overnight in ambient air to remove ethanol.

Metal Oxide Deposition on ACFs

The ACFs were modified by deposition of metal oxide nanoparticles (NPs) via wetness impregnation of a precursor by immersion followed by its thermal decomposition. The precursors that were used included: $Mg(NO_3)_2 \cdot 6H_2O$, $Ca(NO_3)_2 \cdot 4H_2O$, $La(NO_3)_3 \cdot 6H_2O$, $Zn(NO_3)_2 \cdot 6H_2O$ $Al(NO_3)_3 \cdot 9H_2O$ and Ti(IV) bis(ammonium lactato)dihydroxide, were all provided by Sigma-Aldrich (> 98% purity). In a standard procedure the fibers were first dipped into a precursor solution of in ethanol (> 99.8%, Fluka) or water (Ti(IV) bis(ammonium lactato)dihydroxide). The precursor concentrations were calculated using the ACF wetness capacity to obtained the final metal loading of 5 wt.%. The wetness capacity is calculated by measuring the amount of solvent absorbed per unit mass of adsorbent. The impregnated fibers were then dried in air and thermally treated in a He (>99.99%, Carbagas, Switzerland) flow (50 ml min^{-1}, 10 K min^{-1}). The treatment temperature (673-773 K) was set higher than the decomposition temperature of the precursor.

3.1.3   Zeolites

The zeolites samples used in this study were prepared from commercial Na-X (Sigma-Aldrich, 13X, pellets 1.6mm, Switzerland). The pellets were grinded in a Fritsch centrifugal ball mill (Germany) at low rotation speed for 2 minutes. Milled Na-X pellets were then sieved in Fritsch Analysette (Germany) to obtain a pellet size fraction of 350 to 600 μm.

Na-X-H_2O was prepared by treatment of 1 g of Na-X in 100 ml of deionized water during 120 min in a beaker placed in a bath at 373 K. The samples were filtered and dried to remove the excess water then placed in a horizontal quartz tube furnace heated to 573 K at 10 K min^{-1} under 100 cm^3 min^{-1} in N_2 (>99.99%, Carbagas, Switzerland) and calcined at 573 K for 1h.

3.2 Characterization Techniques

3.2.1 Brunauer-Emmett-Teller Surface Area

The specific surface area (SSA) and pore volume were determined by physical adsorption of N_2 at 77 K using a Sorptomatic 1990 (Carlo Erba Instruments). Prior to analysis, the samples of zeolites, original ACFs and ACFs with nanoparticles were outgassed at 523 K for 2h under vacuum ($7 \cdot 10^{-2}$ bar) whereas oxidized and amine functionalized ones were outgassed at 373 K for 3h under vacuum ($7 \cdot 10^{-2}$ bar). N_2 adsorption/desorption isotherms were recorded at 77 K over the relative pressure range of $0.00005 \leq p/p_0 \leq 0.98$. The specific surface area was calculated using BET equation [55].

$$\frac{p}{V(p_0 - p)} = \frac{1}{V_m C} + \frac{C-1}{V_m C}\frac{p}{p_0} \tag{3.1}$$

Where p is the N_2 partial pressure, p_0 is the saturation pressure, V is the amount adsorbed in volume STP (cm^3 g^{-1}) and C is an empiric parameter indicating the energetics of the adsorption process. The N_2 monolayer volume (V_m) is obtained by the linearization of equation 3.1. The pore volume was calculated with the N_2 volume adsorbed at $p/p_0 = 0.98$.

3.2.2 Temperature-Programmed Desorption

The characterization and quantification of oxygen-containing groups on the ACFs surface was performed via TPD experiments. An ACFs sample (~100 mg) loaded in a quartz reactor connected to a mass spectrometer was heated in a He flow (50 cm^3 min^{-1}) up to 1223 K (10 K min^{-1}). Prior to the experiment, the reactor was purged by He for 30 min at room temperature. The gases evolved from the ACFs sample (CO and CO_2) due to decomposition of O-containing groups were analyzed via mass spectrometry. Calibrated mixtures 3% (v/v)

CO/He and 2% (v/v) CO_2/He (Carbagas, Switzerland) were used for concentration profiles integration.

Quantitative acid site characterization of zeolite was obtained by pyridine TPD monitored by a TCD on a Micromeritics Autochem 2920 II. The zeolite sample was dried under He flow at 773 K (10 K min^{-1}) for 1 h. After cooling down to 373 K, a He flow with 0.1 bar pyridine was passed through the sample using a vapor generator. Flow was switched back to N_2 and a TPD was recorded.

3.2.3   Scanning Electron Microscopy

Scanning electron microscopy (SEM) was carried out using a Carl Zeiss MERLIN FE-SEM equipped with two, annular and Everhart-Thornley secondary-electron, detectors operated at an accelerating voltage of 5-30 keV with a beam current of 1.0-3.0 nA and using ZeissSmartSEM software for data acquisition/manipulation.

3.2.4   Transmission Electron Microscopy

FEI Tecnai Osiris instrument was used for acquiring the scanning transmission electron microscopy (STEM) images. The high angle annular dark field (HAADF) and energy-dispersive X-ray spectroscopy (EDX) detectors were employed. Measurements were carried out at the maximum accelerating voltage of 200 keV. Samples were prepared by embedding the ACFs in epoxy resin followed by ultramicrotomy (diamond grade) and eventual deposition on a holey carbon/Cu grid (300 Mesh).

3.2.5   Atomic Absorption Spectroscopy

The elemental composition of the zeolites were carried out by atomic adsorption spectroscopy (AAS) analysis using a Shimadzu AA-6650 spectrometer with a flame supplied

by an N_2O-acetylene mixture (for Si or Al) or an air-acetylene mixture (for Na). The samples were prepared by zeolite dissolution in boiling aqua regia (1:3 v/v HNO_3/HCl) under reflux followed by the addition of NH_4F.

3.2.6   Infrared Spectroscopy

Infrared spectra of zeolites were recorded on a Perkin Elmer Spectrum II spectrometer equipped with a nitrogen cooled MT detector. Samples were placed into the Harrick Ultra High Vacuum DRIFT cell where they can be treated under gas flow or vacuum with temperature control. Typically, 24 scans were accumulated for each spectrum at a resolution of 4 cm^{-1}.

Zeolite acid sites were characterized by TPD of pyridine. The sample was placed in the DRIFT cell, treated at 373 K under N_2 flow for 1 h, cooled down to room temperature and contacted with a N_2 stream saturated with pyridine vapor pressure. Flow was switched back to N_2 to remove physisorbed pyridine and DRIFT was recorded. Temperature was gradually increased and DRIFT spectra were recorded at different temperatures to characterize acid strength.

3.2.7   Solid State Nuclear Magnetic Resonance

Nuclear Magnetic Resonance (NMR) spectroscopy 1H magic angle spinning (MAS), ^{13}C cross-polarization (CP)-MAS solid-state NMR spectra were recorded on Bruker 800 MHz spectrometers with a conventional double resonance 2.5 mm CP-MAS probe. In all experiments, the rotation frequency was set to 15 kHz unless otherwise noted. Chemical shifts are given with respect to tetramethylsilane as the external reference for both $_1$H and $_{13}$C NMR. The zeolite spectra were recorded at room temperature.

3.2.8   X-ray Diffraction

Powder X-ray diffractograms were recorded on a Bruker/Siemens D500 incident X-ray diffractometer using Cu Kα radiation. The samples were scanned at a rate of 0.02º step^{-1} over the range 5-40º. Diffractograms were identified by direct comparison with the JCPDS-ICDD reference standards, *i.e.* Na-X (045-0946).

3.3   Measurements Errors and Fittings

Measurements errors are occurring during every scientific experiment. The sources of experimental errors result from the experimenter or analytical tools imprecisions. To evaluate the errors, the measurements were reproduced. The results reported in this thesis are the mean value of the different measurements and the error was estimated based on their variance.

Besides errors on the measurements, linear or non-linear regression provides additional uncertainties. They are coming from the fitting of the models on the experimental data. The quality of the fitting of the statistical model on the experimental data is described by the coefficient of determination (R^2). However this parameter does not give reliable information on the equation parameters. The determination of the equation parameters of linear or non-linear model was performed with Matlab program using the "fittype" function. The errors obtained on the parameters are directly calculated by Matlab. The errors indicated on the values calculated from data fitting represent the 95% confidence bounds.

3.4   Experimental Setup and Procedures

3.4.1   Setup

The setup used for adsorption study via a transient response method is shown in **Figure 3.1**. It consists of a gas generator (FlexStream Base Permeation Unit, Kin-Tek), two

pneumatic actuators connected to a spool valve (Asco Numatics), a quartz tubular reactor (length – 25 cm, inner diameter – 3 mm) and a sensitive mass spectrometer (Hiden Analytical HPR 20 QIC). The reactor charged with an adsorbent is placed in a tubular oven (Carbolite MTF 10/25/130) for temperature control.

Pressurized air (6 bar) was connected to a spool valve (solenoid air pilot operated - spring return) controlled with a numerical unit (National Instrument 6009) equipped by the LabView software. Depending on the spool valve position, pressurized air is directed to one of the two outlets and then to both pneumatic actuated three-way valves (Whitey, double acting mode, 180° actuation) via ¼ inches stainless steel tubing (Swagelok). The position of the pneumatic actuated three-way valves (*i.e.* reactor or by-pass line) depends on which pneumatic actuator inlet was under pressure. Due to the pressure, a piston in the actuator chamber moves from one position to another creating an inversion of the connected three-way valves. To insure simultaneous switch of both three-way valves, tubes length between the spool valve and both pneumatic actuators are identical. With the described valves system, the switch from the bypass to the reactor line or inversely was reproducible and sufficiently quick to avoid any disturbance of the gas flow.

The gas generator providing a diluted toluene or acetaldehyde (ppm, ppb) flow was composed of a gas line with a mass flow controller connected to a permeation tube and an oven. A permeation tube with a calibrated permeation membrane filled with liquid toluene (99.9% VWR Chemicals, AnalaR NORMAPUR) or acetaldehyde (99.5% Sigma–Aldrich, Fluka Analytical) or with paraformaldehyde (Kin-Tek) was placed in the oven at desired temperature. Thus, the adsorbate permeation rate was controlled by the oven temperature (303-333 K ± 0.01 K). Its concentration (10-100 ppmv) was adjusted at a fixed flow rate (100-1000 cm^3 min^{-1}). For butadiene (1000 ppmv in He) and concentrated acetaldehyde (1300 ppmv in He) gas bottles (Carbagas, Switzerland) were used instead of the gas generator.

The reactor outlet was continuously monitored by an online mass spectrometer with short sampling time (<500 ms), high sensitivity (500 ppb) and stability (< ± 0.5% variation over 24 h).
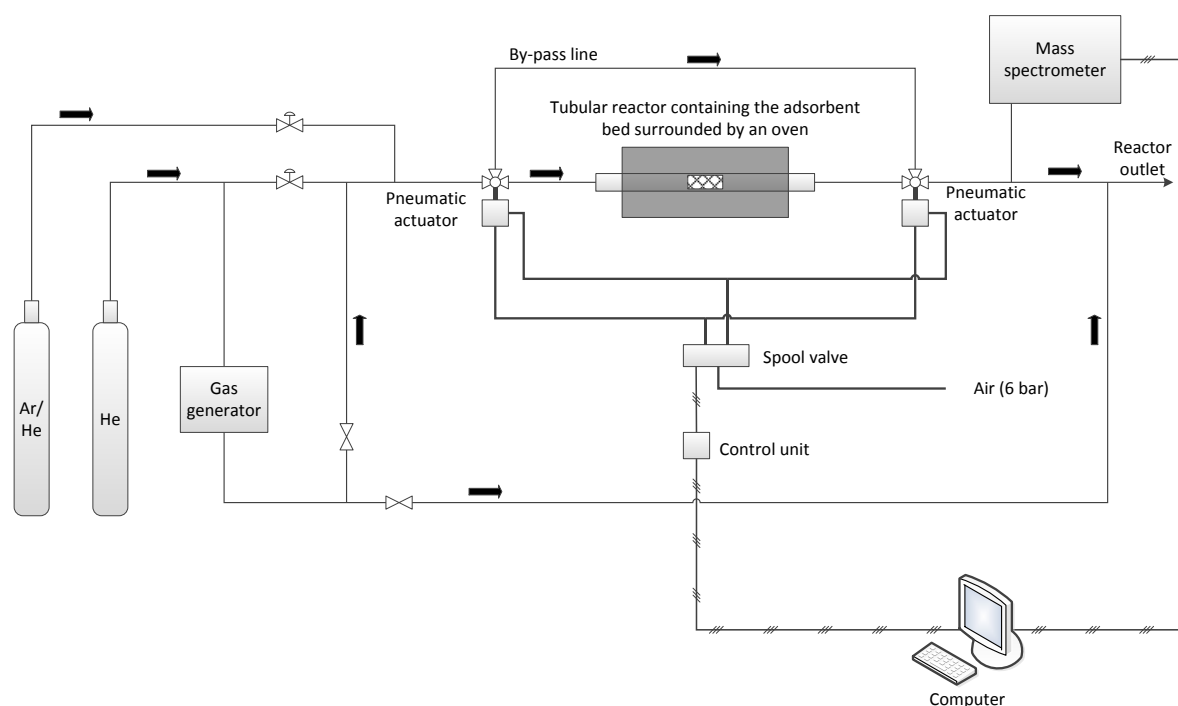
Figure 3.1 Experimental setup for adsorption experiment

3.4.2 Transient Response Method

The adsorption dynamics of the developed adsorbent were studied by a transient response method [185-187]. This methodology was originally developed for kinetic studies of catalytic reactions [188] but is easily adapted for adsorption. It is based on the monitoring of the response at the tubular reactor outlet to a quick change of concentration at the reactor inlet for example a step concentration change. "Dynamic column method" is used to measure the adsorption capacity. This method requires a constant VOC flow through a sorbent bed and a

continuous monitoring of the downstream concentration. In this way breakthrough curves are obtained. The adsorption capacity is calculated by numerical integration of the area defined between the breakthrough curve of an inert tracer (Ar) and the adsorbate [189].

3.4.3 Dynamic Adsorption Measurements

Before measurements, the adsorbent samples placed in the central part of the quartz tubular reactor were outgassed at 298 K in a He (99.999% Carbagas Switzerland) flow (40 cm^3 min^{-1}) unless otherwise noted. The adsorption experiments were carried out at 298 ± 1 K and with gas flow rate of 300 cm^3 min^{-1} (linear velocity ~0.5 m s^{-1}). The gaseous mixtures contained various concentrations of VOC in He. The inert tracer signal (Ar 2% (v/v) in He) was obtained in a separate experiment.

The adsorption capacity measurements consist of the following steps:

1. Stabilization of the gas mixture (VOC in He) flow through the bypass to measure the initial VOC concentration.

2. After a switch to the reactor, the gas mixture flows through the adsorbent bed until the outlet VOC concentration attains the initial one measured during the stabilization step. In such a manner a breakthrough curve was obtained.

The Ar (inert tracer) breakthrough curve was used to characterize the flow pattern and the residence time distribution in the reactor. The Ar-He mixture was injected through the reactor pre-purged by He using a switch from the bypass to the reactor line.

The area defined between the Ar and the VOC breakthrough concentration curves was numerically integrated and the adsorption capacities (wt.%) were calculated as follow.

The adsorption points are numerically integrated by using the trapezoid rule. For two successive measurements c_i, c_{i+1}, the area a_i (in counts) corresponding to the interval delimited by their corresponding time t_i and t_{i+1} is given by:

$$a_i = (t_{i+1} - t_i)\frac{(c_{i+1} + c_i)}{2} \tag{3.2}$$

The total area under the breakthrough curve corresponds to the amount of non-adsorbed VOC during the experiment. For n measurements, it is given by:

$$a_{non-ads} = \sum_{i=1}^{n} a_i \tag{3.3}$$

Therefore the area related to the quantity of adsorbate retained by the adsorbent is:

$$a_{ads} = a_{total} - a_{non-ads} \tag{3.4}$$

The area corresponding to the total amount of VOC injected is given by:

$$a_{total} = c_{VOC} \cdot t_{ads} \tag{3.5}$$

Where c_{VOC} is the response of the last measurement and corresponds therefore to the upper baseline value.

Before obtaining the capacity from the total amount of VOC adsorbed, the volume of VOC injected during the adsorption, V_{VOC}, is calculated with total flow rate $\dot{n}$, the inlet VOC concentration (in ppmv) and the time of adsorption t_{ads}:

$$V_{VOC} = \dot{n} \cdot c_{VOC} \cdot t_{ads} \tag{3.6}$$

From the ideal gas law the number of VOC moles is obtained:

$$n_{VOC} = \frac{p \cdot V_{VOC}}{R \cdot T} \tag{3.7}$$

Where p and T are the standard temperature and pressure R is the gas constant. As the mass of adsorbent is considered for the calculation of capacity, the moles of VOC injected are converted to the corresponding mass $m_{VOC,total}$ with the molecular mass m_{VOC}.

$$m_{VOC,total} = n_{VOC} \cdot M_{VOC} \tag{3.8}$$

The mass of VOC adsorbed $m_{VOC,ads}$ can be calculated from the total area and the one related to adsorbed VOC.

$$m_{VOC,ads} = m_{VOC,total} \frac{a_{ads}}{a_{total}} \tag{3.9}$$

Eventually the capacity of the adsorbent toward a given VOC can be calculated by knowing the mass introduced in the reactor:

$$C_{\%(w/w)} = 100 \cdot \frac{m_{VOC,ads}}{m_{adsorbent}} \tag{3.10}$$

3.4.4 Temperature-Programmed Desorption

TPD experiments were carried out in the same setup used for toluene adsorption. Prior to desorption experiment ACF samples were saturated by the VOC at 298 K before being

heated in a He flow (100 cm^3 min^{-1}) at different temperature ramps (3-30 K min^{-1}). The outlet concentration of desorbed VOC was continuously monitored by a mass spectrometer (Hiden Analytical HPR 20 QIC) and plotted as a function of temperature. Numerical integration of the VOC desorption peak was carried out to calculate the adsorption-desorption mass balance.

3.4.5   Characterization of Reactor Flow Pattern

The characterization of the tubular reactor used for adsorption experiment is carried out using the dispersion model. The dimensionless group used to characterize the residence time distribution in the real tubular reactor is the vessel dispersion number:

$$\frac{D}{uL} \tag{3.11}$$

where D is the dispersion coefficient, u is a linear velocity in the reactor and L is a length of the reactor.

If this number tends to 0, the dispersion is negligible, hence a plug flow behavior can be assumed. A vessel dispersion number tending to infinite means a large dispersion or a complete back-mixing behavior. In practical cases 0.01 is the threshold value under which a tubular reactor can be treated as ideal plug flow.

The vessel dispersion number was obtained using step-wise injection of an inert tracer (Argon) into He flow through the reactor. Different gas flow rates were applied. The Ar concentration at the reactor outlet was monitored by the mass spectrometer (**Figure 3.2 A**).
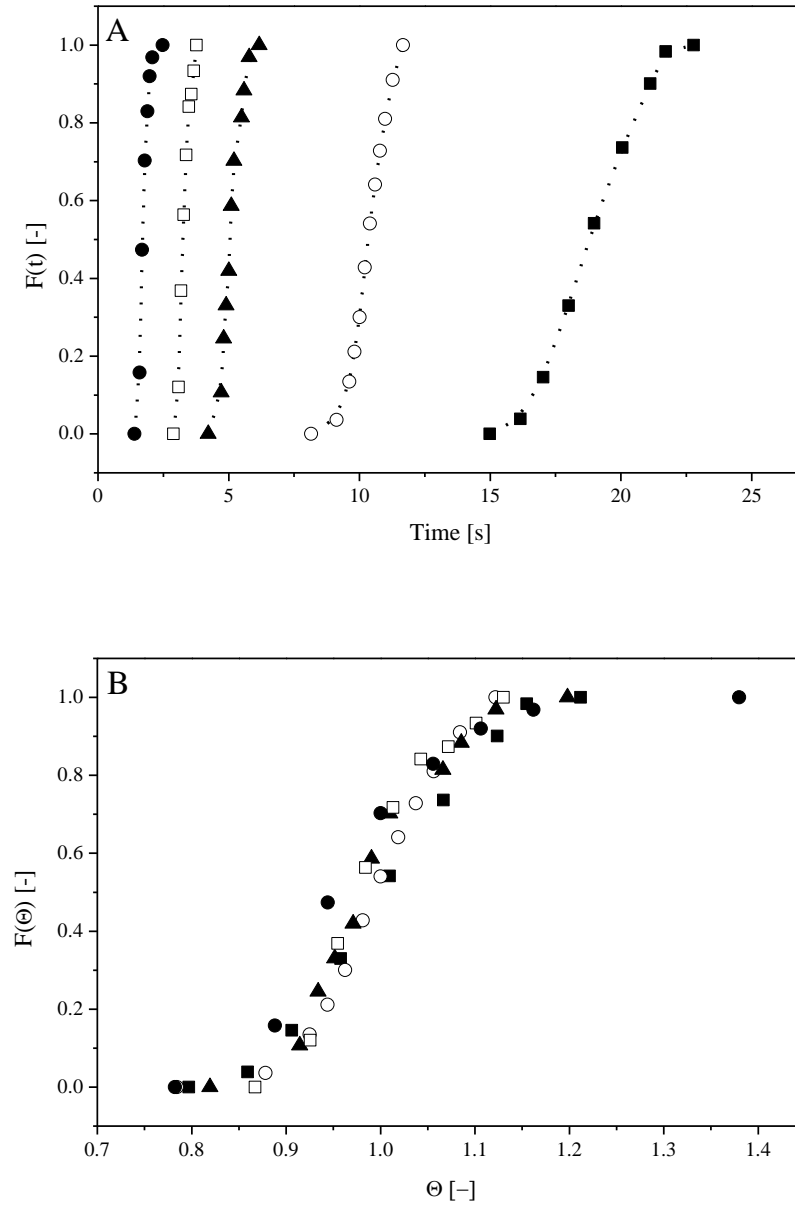
Figure 3.2 Reactor outlet response to a step-wise injection of Ar (inert tracer) at the reactor

inlet as function of time (**A**) and dimensionless time (Θ) (**B**) at different flow rate: 25 cm^3

min^{-1} (■) 50 cm^3 min^{-1} (○) 100 cm^3 min^{-1} (▲) 200 cm^3 min^{-1} (□) 400 cm^3 min^{-1} (●)

The mean residence time, $\bar{t}$, and the variance around the mean, σ^2, are subsequently

calculated:

$$\bar{t} = \int_0^1 t\,dF = \sum_0^1 t_i \Delta F_i \tag{3.12}$$

$$\sigma^2 = \int_0^1 (t - \bar{t})^2\,dF = \sum_0^1 (t_i - \bar{t})^2 \Delta F_i \tag{3.13}$$

ΔF_i was obtained by normalizing the tracer concentration:

$$F(t) = \frac{c_i}{c_0} \tag{3.14}$$

where c_o is an inlet Ar concentration and c_i is a concentration at time t.

The vessel dispersion number for small extents of dispersion was obtained by combining equation 3.12 and 3.13 [190]:

$$\sigma_\Theta^2 = \frac{\sigma^2}{\bar{t}^2} = 2\left(\frac{D}{uL}\right) \tag{3.15}$$

The obtained values are presented in **Table 3.1**. It can be seen that for all flow rates >10 cm^3 min^{-1} the vessel dispersion number is < 0.01. A "piston type" flow pattern is therefore insured at all flow rates. The rector response to a stepwise injection normalized by its mean residence time is presented in **Figure 3.2 B**. It shows that an identical flow pattern is obtained for the different flow rate.

Table 3.1 Dispersion number as a function of gas flow rate

Flow rate [cm^3 min^{-1}]	Dispersion number $\left(\frac{D_{ax}}{L_t u}\right)$ [-]
7.5	0.0122
10	0.0087
25	0.0034
50	0.0023
100	0.0019
200	0.0025
400	0.0040

4 Effect of ACFs Morphology on Toluene Adsorption

In this chapter the effect of the micropore structure of activated carbon fibers (ACFs) on the adsorption of toluene at low concentration (10-80 ppmv) was studied over two microporous types of ACFs. The ACFs present similar surface chemistry but different porous structure. Toluene adsorption isotherms were determined for both ACFs at different temperatures. Different adsorption model such as Langmuir, Dubinin-Radushkevich and Dubinin-Astakhov were fitted to the experimental data. The enthalpy of adsorption was subsequently calculated. The enthalpy of adsorption was also calculated from toluene desorption experiments. Both values were compared and the influence of the ACFs microporosity on the toluene adsorption enthalpy was studied.

4.1 Introduction

As shown in **Chapter 2**, high boiling point VOC are efficiently removed from diluted gas streams using activated carbon due to their large microporous volume and their hydrophobic surface character. However as described in **Chapter 2** at diluted VOC concentration the mean micropore size can influence the efficiency of the adsorbent.

The removal of toluene was often reported over microporous AC [82, 100, 191-195] or ACFs [92, 101, 196-198] however, the influence of the microporosity on toluene adsorption is not clearly established. The influence of the adsorption temperature on the adsorption capacity and the adsorption thermodynamic data are often missing, limiting the understanding of the adsorbent-adsorbate interactions. The adsorption thermodynamic data are also crucial for the design of an efficient adsorbent bed. It allows forecasting its life time between regenerations.

The present chapter investigates the effect of microporosity on toluene adsorption at low concentration (<100 ppmv) over two commercial ACFs. The adsorption isotherms were obtained at different temperatures (298-353 K) by varying toluene partial pressure (1-8 Pa). The experimental results were compared to Langmuir [199], Dubinin-Radushkevich (D-R) [200] and Dubinin-Astakhov (D-A) [201] adsorption models by varying model parameters to fit the experimental data. The Langmuir model assumes monolayer coverage of the adsorbent whereas the D-R and the D-A equations are semi-empirical models based on the 'pore filling mechanism' [202, 203]. This study analyses the differences in the adsorption thermodynamics for two microporous adsorbents in the low VOC concentration range. The enthalpy of adsorption has been determined from adsorption isotherms using D-R and D-A models. Temperature-programmed desorption (TPD) of toluene for both adsorbents was performed and simulated as another method for enthalpy of adsorption measurement. The enthalpies of adsorption values determined by both methods were then compared.

4.2 Experimental

Materials

All materials are presented in detail in **Section 3.1.1**. Prior to adsorption measurements the samples were heated at 673 K (He 40 cm^3 min^{-1}) during 30 minutes to remove the oxygen containing groups from the ACFs surface.

Adsorbents Characterization

The ACFs morphology was characterized by N_2 adsorption at 77 K. The ACFs surface chemistry was assessed by TPD of the oxygen-containing groups of the oxidized ACFs monitoring CO and CO_2. Detailed description of the apparatus used and the conditions applied can be found in **Section 3.2**.

Adsorption-Desorption Measurements

Toluene adsorption isotherms on the ACF-1 and ACF-2 (10 mg ± 0.1) were obtained by measuring the adsorption capacity at different temperatures (298-353 K) and toluene partial pressures (10-80 ppmv). The experimental setup used for adsorption experiments was presented in **Section 3.4.1** and the calculation details in **Section 3.4.2**.

The temperature-programmed desorption (TPD) experiments were carried out as described in **Section 3.4.4**. In all cases the adsorption-desorption mass balance was larger than 95 wt.%.

4.3   Results and Discussion

4.3.1   Characterization of ACFs

Morphology

The ACFs materials consist of elementary filaments of ~10 μm diameter. The representative SEM image of the adsorbents is shown in **Figure 4.1**. Due to the small diameter of the fibers fast mass transfer within micropores is expected. Moreover a large void fraction of the filaments network results in permeability and low pressure drop during gas passage. The network of filament can be seen at the lowest magnification. More detailed pictures of elementary filament are obtained with increased magnification. White spots (500 nm) become distinguishable on the filament surface (15000x magnification). They are probably residue of salt used at the activation stage of the ACFs synthesis. Such particles are probably not influencing the adsorption of VOC due to their large size compared to ACFs micropores (~2 nm). At the higher magnification some holes in the filament structure are visible. Similarly to the activation metal salts residue they are not supposed to influence the adsorption process because of their large size (300-400 nm).
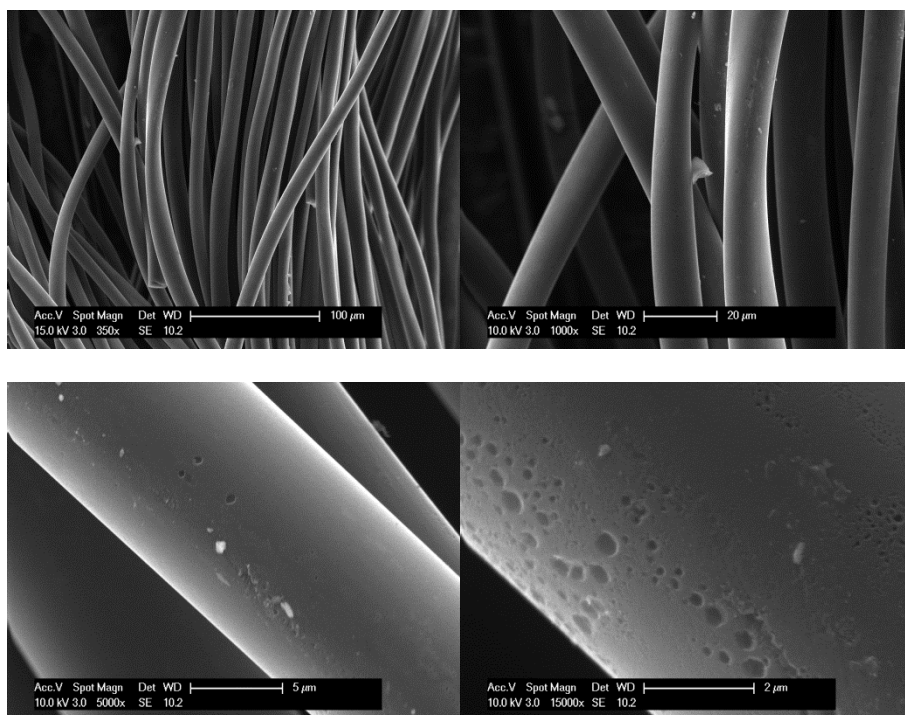
Figure 4.1 SEM pictures of ACF-2 with different magnification

Figure 4.2 presents typical N_2 adsorption isotherms obtained over the samples used in this study and shows the larger nitrogen adsorption capacity of the ACF-2 as compared to ACF-1. Both isotherms exhibit a type I profile typical for microporous adsorbents according to the IUPAC classification [12].

In order to evaluate more precisely the morphology of the ACF-1 and ACF-2, a pore size determination was carried out via comparative α-method (**Section 2.3.1**) [71, 72, 75, 77]. In this work, carbon black was chosen as a non-porous reference material. Its SSA obtained by the BET method within the N_2 partial pressure range of 0.05-0.33 was ~9±1 m^2 g^{-1}. The α-plots obtained for all ACFs samples (**Figure 4.3**) are almost linear and constant at $\alpha_s > 1$. This implies that the external surface area is relatively small as compared to the total surface area meaning that most of the surface is due to the pores [58]. It confirms that both adsorbents are microporous with a relatively narrow pore size distribution. The slope change of ACF-1

appears at $\alpha_s \sim 0.6$ whereas an extremely steep slope is seen at slightly higher α_s values for ACF-2. The α_s value difference at which the slope change occurs is interpreted as a microporosity difference between ACF-1 and ACF-2. A slope change at higher α_s values (ACF-2) signifies relatively large micropores [204]. It is then suggested that ACF-2 contains mainly supermicropores (d_p 1-2 nm) whereas ACF-1 is an ultramicroporous ($d_p < 1$ nm) adsorbent.
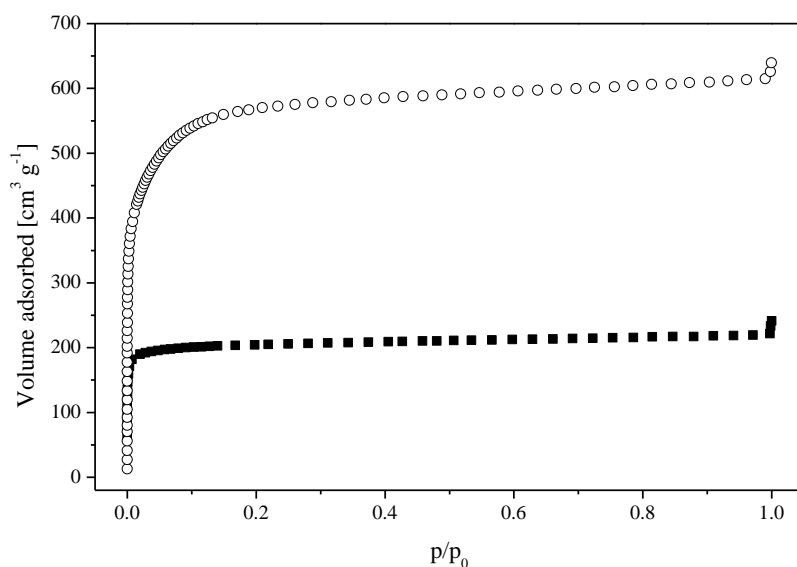
Figure 4.2 N_2 adsorption isotherms (77 K) of ACF-1 (∎) and ACF-2 (○)
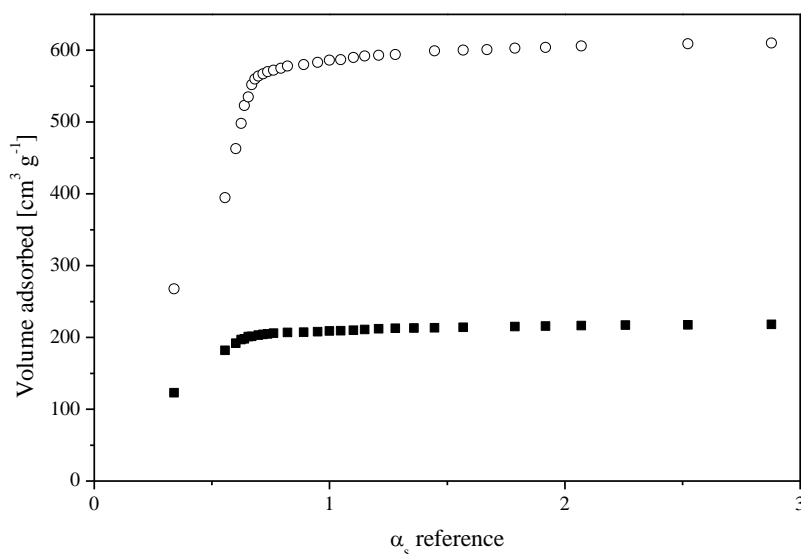
Figure 4.3 α-plot of ACF-1 (■) and ACF-2 (○)

The specific surface area of all samples was calculated through the BET equation using N_2 adsorption data [55]. The equation was linearized in the partial pressure range of 0.001-0.07 for ACF-1 and 0.01-0.1 for ACF-2. ACF-1 shows a lower SSA (800 m^2 g^{-1}) compared to ACF-2 (2150 m^2 g^{-1}). As shown in **Table 4.1**, the C values obtained are > 100 for all the samples confirming their microporous morphology. The C value of the BET equation which can qualitatively describe the pore size, is larger for ACF-1 as compared to ACF-2 indicating narrower microporosity and confirming the results obtained with the α-plot.

Surface Functionalities

The surface chemistry analysis was addressed via TPD with the outlet composition monitored by the mass spectrometer. Two major molecules desorbing from the ACFs surface are CO and CO_2 revealing the presence of O-containing groups in low quantities on the surface of both ACFs. **Figure 4.4** shows TPD profiles of both original samples. As can be

seen, no desorption of CO occurs at low temperature for both fibers whereas a CO_2 desorption

peaks appears between 400-650 K attributed to carboxylic groups [117].
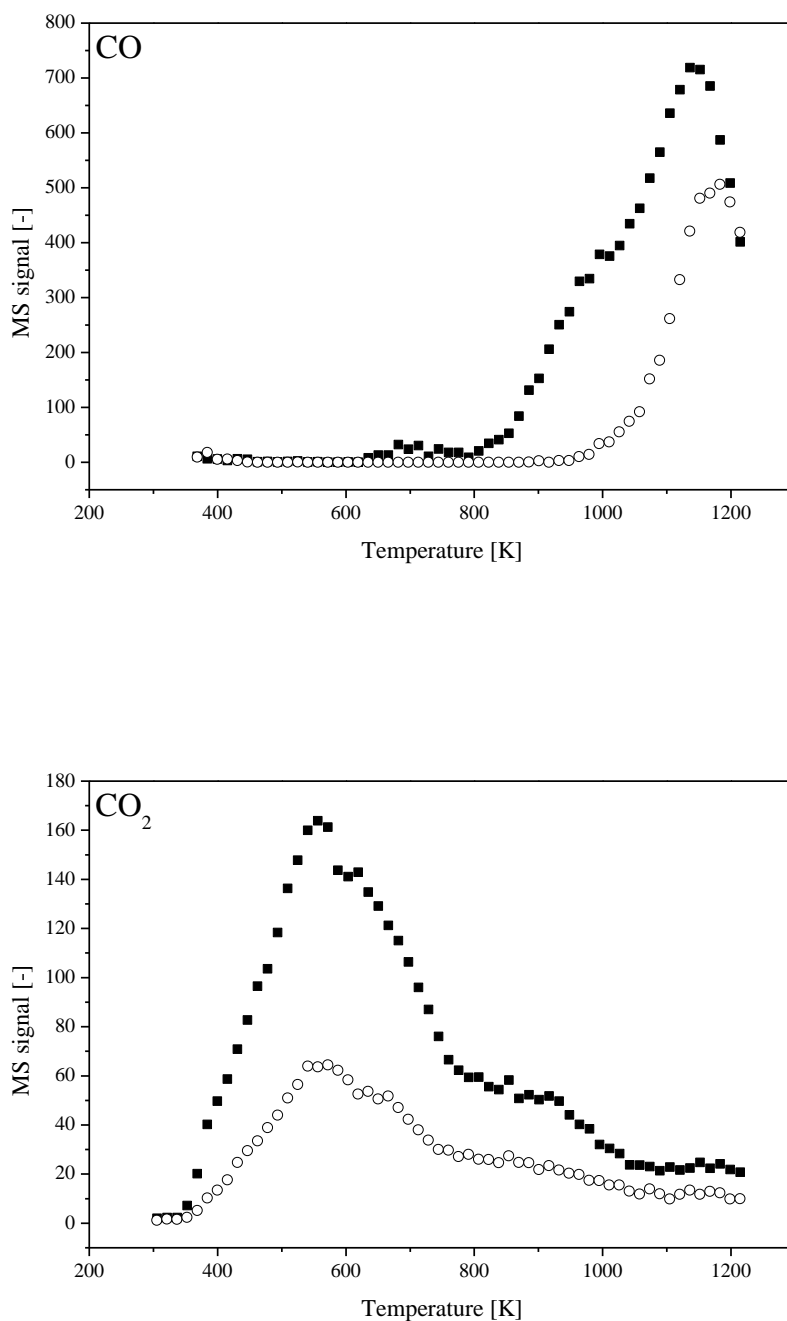
Figure 4.4 TPD profiles of original ACF-1 (■) and ACF-2 (○) (10 K min^{-1}, 50 cm^3 min^{-1})

The integration of the CO and CO_2 concentration curves gives the surface oxygen contents of the samples which are reported in **Table 4.1**. The total oxygen concentration in the ACFs was found to be quite low and comparable to previously published results [100, 101]. As shown in **Figure 4.4**, ACF-1 contains more O-containing groups decomposing in CO_2 as compared to ACF-2. The amount of CO evolved is also slightly higher in the case of ACF-1. Therefore, the concentration of polar groups on the ACF-1 surface is larger.

It was reported that O-containing groups reduce the carbon adsorption capacity of toluene at constant porosity [100]. Therefore, to compare only the effect of the microporosity on toluene adsorption capacity, the surface chemistry of both ACFs should be comparable. To obtain similar surface chemistry of both ACFs samples a heat treatment under inert (He) at 673 K to remove part of the O-containing groups was performed. The TPD pattern of ACF-1 and ACF-2 pretreated at 673 K is presented **Figure 4.5**.
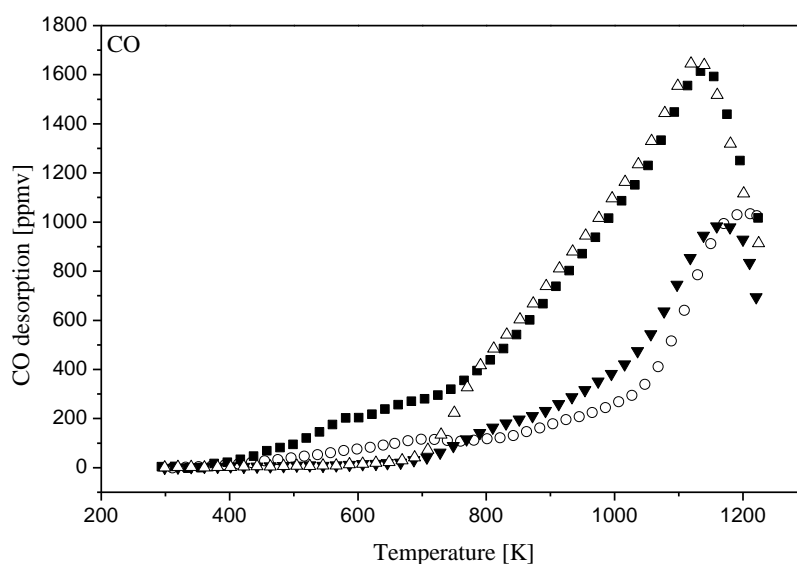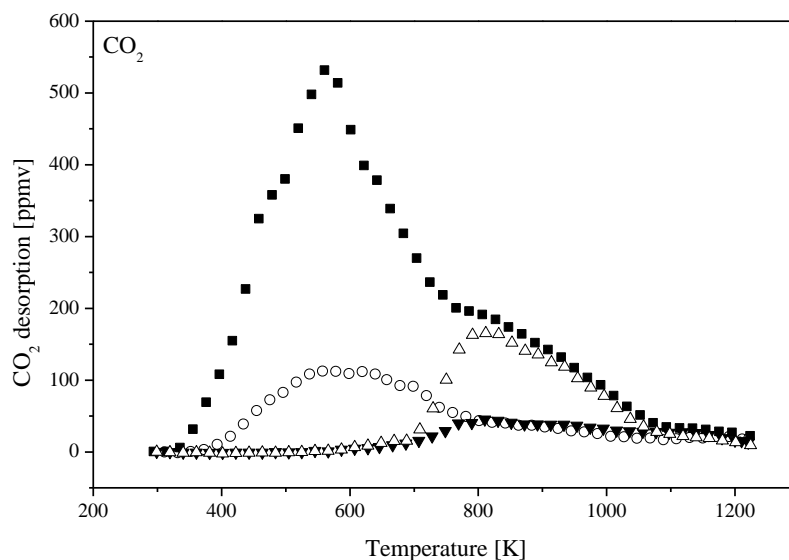
Figure 4.5 TPD profiles of original ACF-1 (■), ACF-2 (○) ACF-1-673K (△) and ACF-2-673K (▼) (10 K min^{-1}, 50 cm^3 min^{-1})

The TPD pattern shows clearly a lower desorption of O-containing groups upon heat treatment. For both samples pretreated at 673 K the desorption of CO and CO_2 is almost zero until 673 K. At this temperature the carboxylic groups characterized by the peak at 600 K are removed [117] however part of the lactones, lactol and anhydride group, characterized by the shoulder at 800 K remains. The O-containing groups desorbing in CO at higher temperature such as carbonyl and phenol are also remaining on the surface. In conclusion, the surface polarity of treated fibers is reduced, particularly for ACF-1.

The characteristics of ACF-1 and ACF-2 pretreated at 673 K are presented in **Table 4.1**. The heat treatment increases slightly the specific surface area and the pore volume of both fibers due to oxygen group removal [205]. The oxygen content obtained by integration of CO and CO_2 curves for ACF-1-673K and ACF-2-673K is low. The total oxygen content is obtained by the addition of the integral of the CO and 2 times the integral CO_2 desorption curve. Further increase of the pretreatment temperature would have removed more O-

56

containing groups and created a more hydrophobic surface, however it was noticed that the porosity started to collapse around 773 K particularly for ACF-1 (decrease of the micropore volume). Hence, 673 K was chosen as the optimum temperature avoiding a porosity modification and removing the maximum of O-containing groups. Since after pretreatment, the surface O-content was very low, it was assumed that the polarity was negligible and should not influence the toluene adsorption capacity. Thus, the microporosity is suggested to be the only difference between ACF-1-673K and ACF-2-673K and the influence of pore diameter on toluene adsorption can be studied.

Table 4.1 Characteristics of ACFs

Sample	SSA_{BET} [$m^2\,g^{-1}$]	Pore volume [$cm^3\,g^{-1}$]	C BET equation	Oxygen content [$\mu mol\,g^{-1}$]
ACF-1	800±50	0.38±0.02	6400	800±50
ACF-1-673K	1030±50	0.40±0.02	6700	500±50
ACF-2	2150±50	0.94±0.02	280	420±50
ACF-2-673K	2220±50	0.95±0.02	310	370±50

4.3.2   Toluene Adsorption Isotherms

Typical toluene adsorption results are shown in **Figure 4.6** as breakthrough curves. The adsorption capacity of the ACFs materials was determined by a numerical integration of the area between the toluene concentration curve and the argon curve as described in **Section 3.4.3**. In all the adsorption experiments the outlet toluene concentration was zero indicating a total toluene removal before the breakthrough.
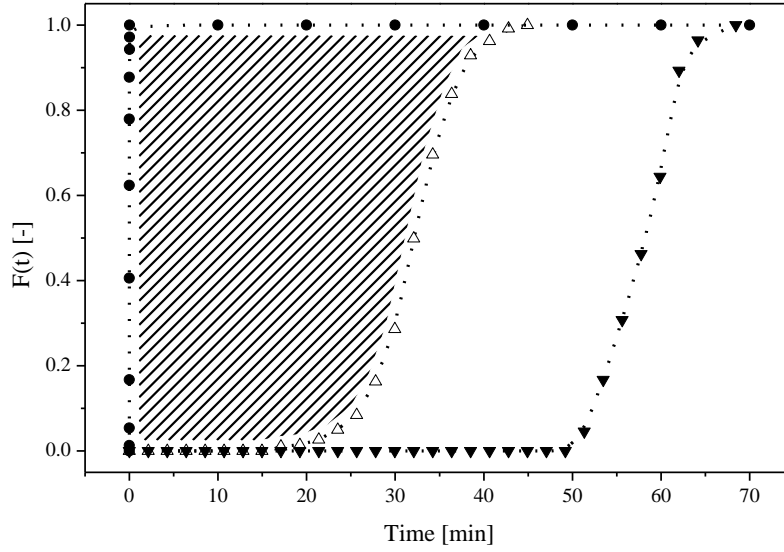
Figure 4.6 Toluene (80 ppmv) breakthrough curves for ACF-1-673K ($\triangle$) and ACF-2-673K

($\blacktriangledown$) and 2% (v/v) Argon tracer ($\bullet$).Total flow rate (STP) 300 cm^3 min^{-1} (298 K)

As can be seen in **Figure 4.6**, the adsorption capacity of ACF-2-673K is larger than ACF-1-673K. This result can be explained by a larger specific surface area and pore volume of ACF-2-673K (**Table 4.1**). By varying the toluene concentration (10-80 ppmv or 1-8 Pa) at different temperature (298- 353 K) a set of adsorption isotherms was obtained for both ACFs (**Figure 4.7**). Langmuir (equation 4.1) and van't Hoff equations (equation 4.2) were first used to fit the experimental data.

$$q = q_{\max,L} \frac{Kp_{tol}}{1 + Kp_{tol}} \tag{4.1}$$

where

$$K = K_0 \exp\left(\frac{-\Delta H^0_{ads}}{RT}\right) \qquad (4.2)$$

The model variables were the total monolayer surface coverage as defined by the Langmuir model ($q_{\max,L}$), the pre-exponential factor of the adsorption equilibrium constant (K_0) and enthalpy of adsorption (ΔH^0_{ads}).

Langmuir model assumes that the maximum adsorbed amount ($q_{\max,L}$) is not a function of the adsorption temperature and the lateral interactions are negligible implying that the enthalpy of adsorption does not depend on the surface coverage. The fitted model parameters obtained for the studied adsorbents are presented in **Table 4.2**.
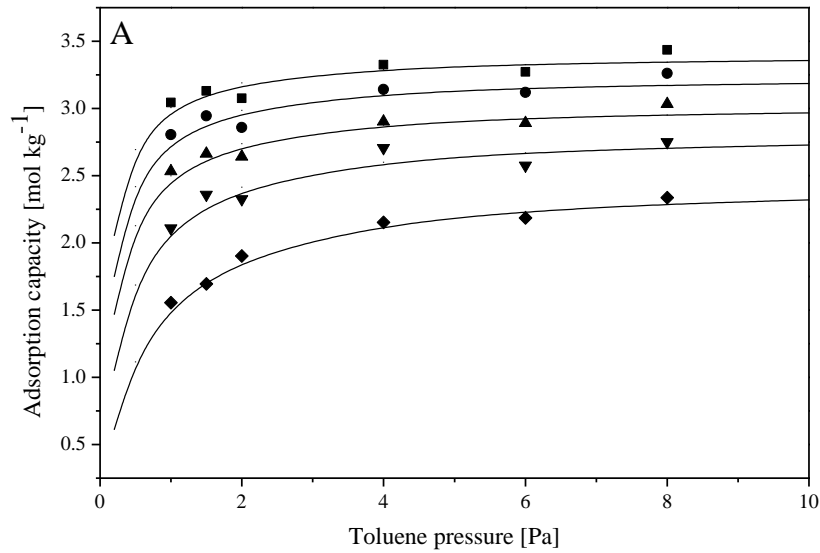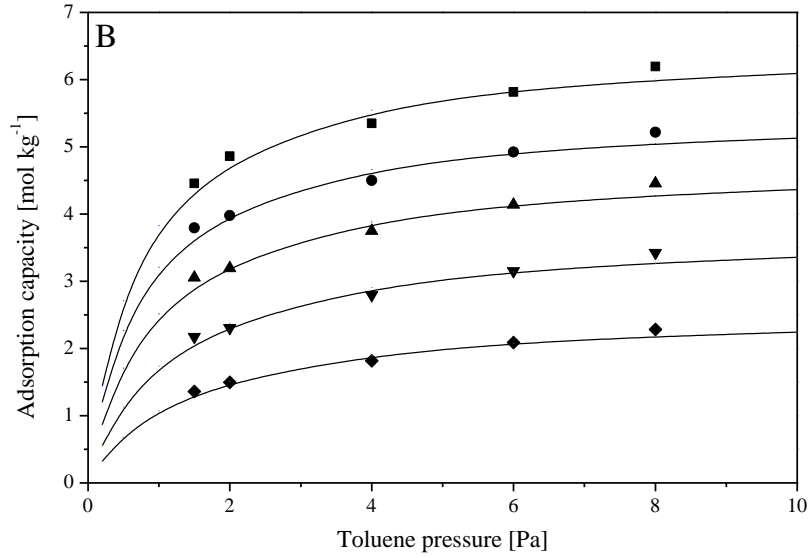
Figure 4.7 Toluene adsorption isotherms on ACF-1-673K (**A**) and ACF-2-673K (**B**) fitted

with the Langmuir model at different temperature: 298 K (■), 308 K (●), 318 K (▲), 333K

(▼), 353 K (♦)

Table 4.2 Langmuir model parameters for toluene adsorption

Adsorbent	$q_{max,L}$ [mol kg^{-1}]	K_0 [Pa^{-1}]	ΔH_{ads} [kJ mol^{-1}]
ACF-1-673K	2.9±0.5	4.3±0.3·10^{-4}	-24.4±4.2
ACF-2-673K	4.6±2	1.3±0.1·10^{-2}	-11.8±4.2

As can be seen in **Table 4.2** the supermicroporous ACF-2-673K has higher maximum

toluene adsorption capacity ($q_{max,L}$) at 298 K as compared to ACF-1 due to the larger specific

surface area and pore volume of the ACF-2-673K (**Table 4.1**). The error on the measurement

of the maximum adsorption capacity is relatively large since these values were found to vary

with the adsorption temperature which is in contradiction with the Langmuir model. Indeed a

total occupation of the adsorption sites are assumed by the Langmuir model regardless of the

temperature at high partial pressure (4.1). Such variation indicates that the Langmuir model may not be correct for toluene adsorption on ACFs.

Figure 4.7 shows the results of the adsorption isotherm fitted to the Langmuir model. The curve determination coefficients (R^2) were found to be larger than 0.75 and 0.96 for ACF-1 and ACF-2 respectively. Despite the apparent good fit, the enthalpies of adsorption obtained for both ACFs are smaller than the enthalpy of condensation (-38 kJ mol^{-1}) [206] which is impossible. Since this result is meaningless, we concluded that Langmuir model is not suitable to describe the toluene adsorption on ACFs. The monolayer adsorption and the absence of lateral interactions are apparently not correct assumptions for microporous materials even at very low toluene partial pressure. Therefore, we assumed that multilayer adsorption and/or a pore filling occurs requiring another adsorption model.

The Dubinin-Radushkevich (D-R) model (4.3) was originally developed for benzene adsorption on activated carbon [207]. This semi-empirical equation was developed for sub-critical vapors in microporous solids where the adsorption process follows a pore filling mechanism. A liquid-like adsorbed phase is assumed in the micropores. Vapors adsorption on many microporous solids, such as activated carbon or zeolites, can be described by the D-R equation. A particular characteristic of the D-R model is the temperature independence of the characteristic adsorption energy (E_0). It implies that adsorption data obtained at one temperature allow determining the characteristic adsorption energy.

$$W = W_0 \exp\left(-\left(\frac{A}{\beta E_0} \right)^2 \right) \tag{4.3}$$

Where W_0 is the maximum adsorbed volume and E_0 the characteristic adsorption energy. The parameter β is a constant specific for the adsorbate. In the case of toluene β is 1.28 [208].

The parameter A represents the Polyani adsorption potential. The value of A is equal to the difference between the chemical potential of the adsorbate in the liquid state and in the adsorbed state at the same temperature.

$$A = RT \ln\left(\frac{p_0}{p}\right) \tag{4.4}$$

p_0 is the saturation pressure of the adsorbate, p is the adsorbate partial pressure and T is the temperature at which the adsorption experiment took place. In this model, the adsorbed phase is assumed to be liquid. Therefore, the saturation adsorption capacity corresponds to the maximum adsorbed liquid volume in the microporous network.

$$q_{max} = W_0 / v_M \tag{4.5}$$

Where W_0 is the maximum adsorbed volume and v_M is the liquid molar volume (toluene = 106.3 cm^3 mol^{-1}). This is in opposition to the Langmuir model where the maximum adsorption capacity is equal to monolayer coverage of the adsorbent surface.

The saturation capacity is temperature dependent since the liquid molar volume is a function of temperature. The integral form of the temperature dependence of the saturation adsorption capacity is:

$$q_{max} = q_{max,0} \exp\left(-\delta(T - T_0)\right) \tag{4.6}$$

Where $q_{max,0}$ is the saturation adsorption capacity at a reference temperature T_0 (298 K) and δ is the thermal expansion coefficient of the saturation concentration. For toluene δ is 0.001 K^{-1} [209].

The enthalpy of adsorption of the D-R model can be calculated from the van't Hoff equation

$$\frac{\Delta H_{ads}^0}{RT^2} = -\left(\frac{\partial \ln p}{\partial T}\right)_q \qquad (4.7)$$

The change in vapor pressure with respect to temperature is given by the Clausius-Clapeyron equation

$$\frac{1}{p_0}\frac{dp_0}{dT} = \frac{\Delta H_{vap}}{RT^2} \qquad (4.8)$$

By taking the total derivative of the D-R equation (4.3), the Clausius-Clapeyron equation (4.8) and substituting them in equation 4.7, the expression of the isosteric heat is obtained for a constant loading:

$$-\Delta H_{ads}^0 = RT \ln\left(\frac{p_0}{p}\right) + \Delta H_{vap} + \frac{(\beta E_0)^2 \delta T}{2RT \ln\left(\frac{p_0}{p}\right)} \qquad (4.9)$$

where ΔH_{vap} is the heat of condensation being -38 kJ mol^{-1} for toluene [210].

The isosteric enthalpy of adsorption is the summation of three terms: the first represents the adsorption potential, the second is the heat of vaporization and the third expresses the variation of the maximum capacity with temperature. For the sake of clarity the isosteric adsorption enthalpy is expressed in terms of fractional loading:

$$-\Delta H_{ads}^{0} = \Delta H_{vap} + \beta E_0 \left(\ln\left(\frac{1}{\theta}\right) \right)^{1/2} + \frac{\beta E_0 \delta T}{2} \left(\ln\left(\frac{1}{\theta}\right) \right)^{-1/2}$$

(4.10)

with

(4.11)

$$\theta = \frac{q}{q_{max}}$$

Following equation 4.10, the enthalpy of adsorption is by definition larger than the heat of condensation and depends on the characteristic adsorption energy (E_0) and on the adsorbent fractional loading (θ). The maximum adsorption capacity and the characteristic adsorption energy were obtained by fitting the experimental data to equation 4.3 for all the isotherms and both adsorbents (**Figure 4.8**).
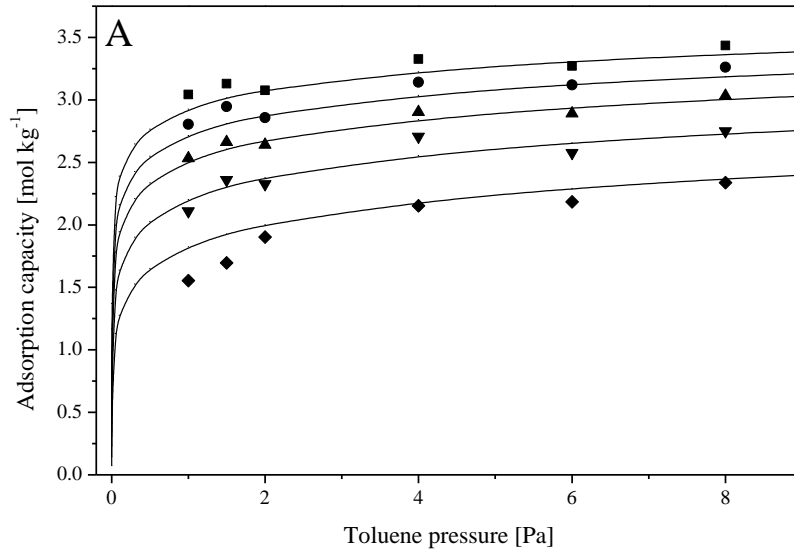
Figure 4.8 Toluene adsorption isotherms on ACF-1-673K (**A**) and ACF-2-673K (**B**) fitted with the D-R model at different temperature: 298 K (■), 308 K (●), 318 K (▲), 333K (▼), 353 K (♦)

The D-R model fits well the experimental data for ACF-2-673K with a determination coefficient (R^2) of 0.98. For ACF-1-673K the R^2 is slightly lower (0.85) but remains acceptable. The parameters (E_0 and $q_{max,0}$) obtained are presented in **Table 4.2**. D-R model predicts a higher maximum toluene adsorption capacity (q_{max}) at 298 K of ACF-2-673K (9.6 mol kg^{-1}) as compared to ACF-1-673K (4 mol kg^{-1}) according to its larger pore volume (**Table 4.1**). The thermodynamic adsorption parameter (E_0) also indicates a difference in toluene adsorption mechanism on both ACF samples. The characteristic adsorption energy (E_0) is 28±6 and 17±2 kJ mol^{-1} for the ACF-1-673K and ACF-2-673K, respectively. High characteristic adsorption energy suggests stronger adsorbate-adsorbent interactions. It is then concluded that adsorbent with ultramicropores have stronger interactions with the adsorbate. Pore filling mechanism suggested by the D-R model seems to be a suitable model for toluene adsorption on ACFs. All the parameter values calculated seem reliable with a relatively small

error. The fitting obtained by the D-R model in **Figure 4.8** could be further improved using the Dubinin-Astakhov model (D-A) [207]. This model is also based on the Polyani adsorption potential and the characteristic adsorption energy and only differs from the D-R equation by the exponent (N):

$$W = W_0 \exp\left(-\left(\frac{A}{\beta E_0}\right)^N\right)$$ (4.12)

In the D-R model the exponent is $N=2$ whereas it can take a random value in the D-A model. This exponent represents the adsorbent surface heterogeneity and is linked to the sharpness of the pore size distribution being specific for each particular adsorbent [211]. For non-homogeneous pore size distribution the typical values are found between 1 and 2, whereas it increases for narrower pore size distribution [207]. Molecular sieving carbon, for example, has a heterogeneity parameter of 3 and for crystalline zeolite this parameter can increase up to 6 [212].

The D-A model was used herein to fit the experimental data of toluene adsorption on both ACFs. The characteristic adsorption energy (E_0), the saturation capacity ($q_{max,0}$) and the surface heterogeneity (N) were adjusted. The results are presented in **Figure 4.9**.
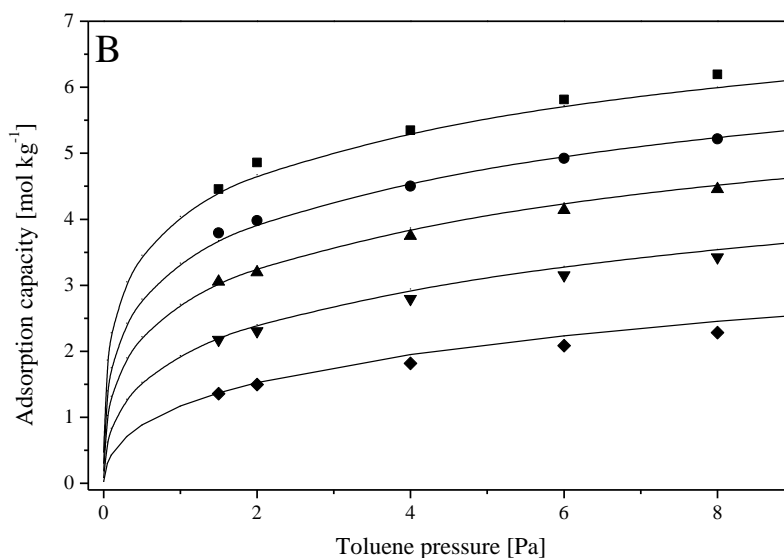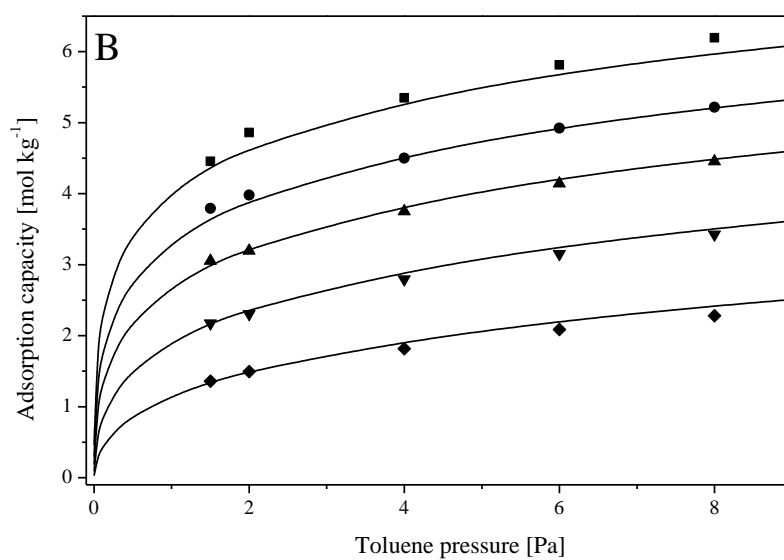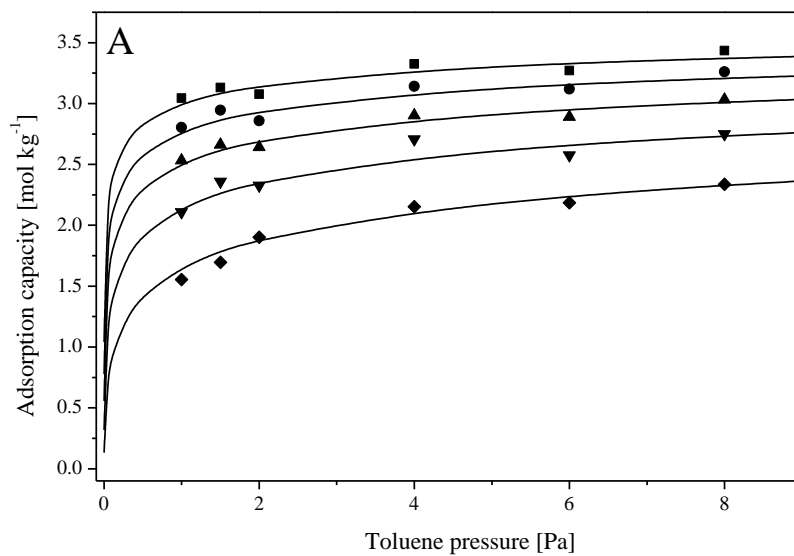
Figure 4.9 Toluene adsorption isotherms on ACF-1-673K (A) and ACF-2-673K (B) fitted

with the D-A model at different temperature: 298 K (■), 308 K (●), 318 K (▲), 333K (▼),

353 K (♦)

Similarly to the D-R model, the D-A model shows also a good fitting of the experimental data. For ACF-2-673K the optimized parameters of the D-A model were extremely close to the D-R ones. The heterogeneity parameter was close to 2, the characteristic adsorption energy was 17 ± 2.0 kJ mol^{-1} and the saturation capacity was 9.5 ± 1.5 mol kg^{-1}, being in accordance to ones obtained with the D-R model. For ACF-1-673K the D-A model gave a better fitting at $N = 3$. The curve determination coefficient was slightly increased with the D-A model, particularly for the isotherm at 353 K R^2=0.91 instead of 0.85 for the D-R model. However due to the degree of freedom during the linearization the error on the parameters is relatively important for the D-A model. It is then not possible to insure that the D-A model is more suitable for the ACF-1-673K despite the better fitting. Hence the parameter values found with the D-R model will be used. The parameter of the D-R and the D-A equation for toluene adsorption are summarized in **Table 4.3**.

Table 4.3 Toluene adsorption parameters

Adsorbent	Dubinin-Radushkevich model			Dubinin-Astakhov model		
	$q_{max,0}$ [mol kg^{-1}]	N	E_0 [kJ mol^{-1}]	$q_{max,0}$ [mol kg^{-1}]	N	E_0 [kJ mol^{-1}]
ACF-1-673K	4 ± 0.4	2	28 ± 6	3.6 ± 0.3	3	27 ± 7
ACF-2-673K	9.6 ± 1.5	2	17 ± 2	9.5 ± 1.5	1.9	17 ± 2

To further prove the validity of the D-R model, the isosteric adsorption enthalpy was evaluated with equation 4.9 for 298 K and is presented as a function of fractional loading in **Figure 4.10**. The dependency of the isosteric adsorption enthalpy on temperature was found to be negligible (0-3 kJ mol^{-1}) in the studied temperature range (298-353 K).
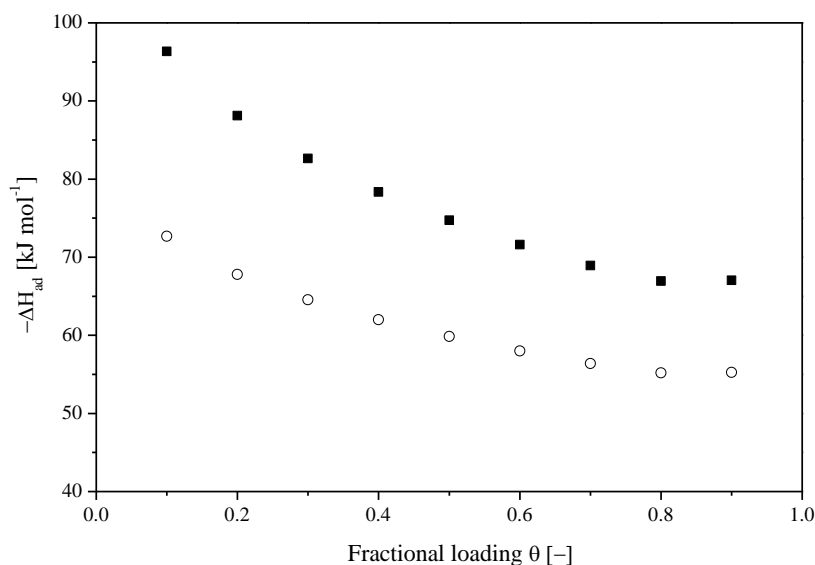
Figure 4.10 Toluene adsorption enthalpy in function of the adsorbent fractional loading for

ACF-1-673K (■) and ACF-2-673K (○)

Figure 4.10 shows a decrease of the isosteric adsorption enthalpy with the micropore filling. The D-R model predicts a very high adsorption enthalpy for low loading, going to infinite at zero loading. The isosteric adsorption enthalpy decreases with the fractional loading until a minimum whereas at fractional loading > 0.95, it increases again (due to the thermal expansion coefficient of the saturation concentration in the third them of equation 4.10). So, the model has limitations and cannot be applied at a fractional loading of 0 and 1. Therefore, the toluene adsorption was studied in the fractional loading range of 0.1-0.9.

The higher isosteric adsorption enthalpy calculated for ACF-1-673K (70-90 kJ mol^{-1}) as compared to ACF-2-673K (55-75 kJ mol^{-1}) is directly linked to their difference in characteristic adsorption energy (E_0). Toluene is therefore more strongly adsorbed in the pores of ACF-1-673K.

The adsorption capacity at 298 K and 80 ppmv of toluene (8 Pa) were 31.6 and 57.0 wt.% for ACF-1-673K and ACF-2-673K, respectively, whereas their specific surface area are 1030 m^2 g^{-1} and 2220 m^2 g^{-1} (**Table 4.1**). The surface normalized adsorption capacity is then higher for ACF-1-673K ($3.3 \cdot 10^{-6}$ mol m^{-2}) as compared to ACF-2-673K ($2.8 \cdot 10^{-6}$ mol m^{-2}). Since the characterization revealed similar surface chemistry (O-containing groups), the larger normalized adsorption capacity for ACF-1-673K is explained by the porosity. Indeed, narrower pores were measured for ACF-1-673K. The higher adsorption efficiency of ACF-1-673K is due to its ultramicroporosity (pore diameter < 1 nm) as compared to supermicropores (pore diameter 1-2 nm) of ACF-2-673K.

The influence of the micropore size on the VOC adsorption capacity of ACFs has already been studied [103, 104]. For some adsorbates (ethane, propane, butane and pentane), a microporous adsorbent with a lower SSA can have a higher adsorption capacity due to narrower pores [104]. This phenomenon is referred to as the cross-over regime, meaning a higher adsorption capacity for a lower specific surface area. The pore filling in ultramicroporous adsorbents is enhanced and the available pore volume is used more efficiently as compared to supermicroporous adsorbents due to the higher interactions of the adsorbate with both pore walls. For supermicroporous adsorbent only single wall interactions is suggested. In the present study, this phenomenon is observed for toluene adsorption. In the range of concentrations (10-80 ppmv), the degree of filling of ACF-1-673K ultramicropores is larger than ACF-2-673K supermicropores. Their fractional loading at 298 K and 8 Pa is 0.86 and 0.63, respectively. The lower specific surface area and smaller pore volume of ACF-1-673K is compensated by a more favorable pore shape leading to a larger toluene adsorption capacity under certain conditions. Thus, the adsorbent pore size along with specific surface area plays a crucial role in toluene removal by adsorption from highly diluted streams.

The narrower pore size of ACF-1-673K explains its larger adsorption enthalpy because of the stronger interactions of the pore walls. Such phenomenon can lead to a larger adsorption capacity of ACF-1-673K, particularly at high temperature. For example at 353 K despite its lower specific surface area (**Figure 4.8 A** and **B**) the adsorption capacity of ACF-1-673K is larger as compared to ACF-2-673K. A larger adsorption enthalpy is particularly interesting at high adsorption temperature. An adsorbent with a lower specific surface area but narrower micropores could be more efficient than an adsorbent with large pore volume and wider micropores. This phenomenon was already reported for low boiling point VOC [104].

4.3.3   Temperature-Programmed Desorption of Toluene

Toluene desorption from the ACFs was carried using different temperature ramps. The TPD profiles recorded for the ACF-2-673K are plotted on **Figure 4.11**.
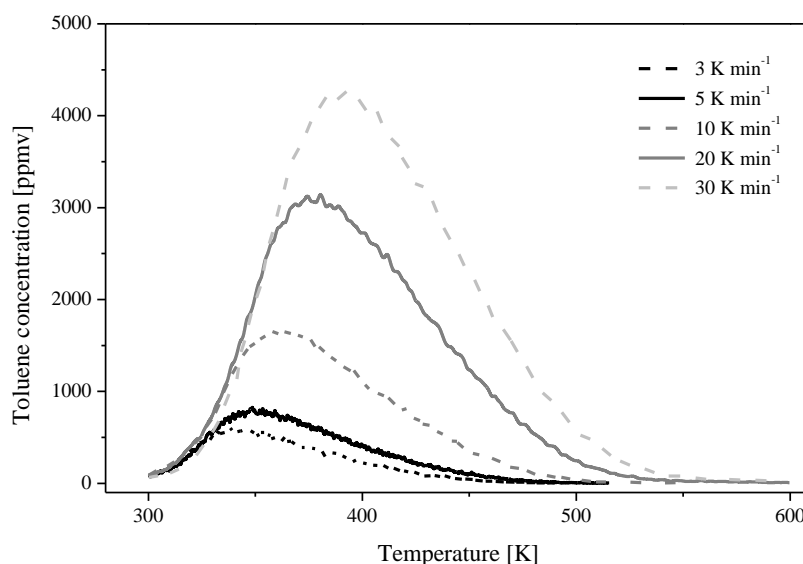
Figure 4.11 TPD profiles of toluene of ACF-2-673K at different temperature ramps (100 cm^3 min^{-1})

As shown in **Figure 4.11**, the peak maximum shifts to higher temperatures with the temperature ramp. In order to determine the kinetic parameters of desorption (E_d, k), TPD curves were numerically simulated for five temperature ramps. By solving the mass balance and linear temperature variation simultaneously, TPD profiles can be simulated. The fitting of the experimental points is then adjusted by varying E_d and k. The mass balance is expressed as following:

$$\dot{n}_{tol,0} - \dot{n}_{tol} = R_d \cdot m_{adsorbent} \tag{4.13}$$

where $\dot{n}_{tol}$ is the molar flow and R_d the desorption rate. Toluene desorption is then expressed as a function of the desorption rate constant (k_d):

$$-\dot{n}_{tol} = -k_d \cdot Z_{tol}^m \cdot m_{adsorbent} \tag{4.14}$$

where Z_{tol} is the concentration of adsorbed species and m the kinetic order of desorption. The rate constant of desorption can be expressed with the activation energy of desorption and supposing a 1st order desorption kinetic:

$$\dot{n}_{tol} = k_{d,0} \exp\left(\frac{-E_d}{R \cdot T}\right) \cdot Z_{tol} \cdot m_{adsorbent} \tag{4.15}$$

The following differential equation was then obtained:

$$\frac{dZ_{tol}}{dt} = k_{d,0} \exp\left(\frac{-E_d}{R \cdot T}\right) \cdot Z_{tol} \tag{4.16}$$

The equation of the linear temperature increase is

$$T = T_0 + \gamma t; \frac{dT}{dt} = \gamma \tag{4.17}$$

where T is temperature, T_0 the initial temperature, γ the temperature ramp and t the time. By combining equation 4.16 and 4.17:

$$\frac{dZ_{tol}}{dT} = \frac{k_{d,0}}{\gamma} \exp\left(\frac{-E_d}{R \cdot T}\right) \cdot Z_{tol} \tag{4.18}$$

The surface concentration of adsorbed toluene as a function of temperature is obtained. By mass balance the gas phase concentration is calculated and can be fitted to the TPD experimental data. The toluene desorption rate depends on desorption rate and the activation energy of desorption. Supposing negligible activation energy of adsorption, the activation energy of desorption is approximated to the adsorption enthalpy [213]. Therefore, a comparison of this parameter obtained by the isotherm modelling and by TPD simulation could be performed. A simulation of a TPD pattern is presented in **Figure 4.12**.
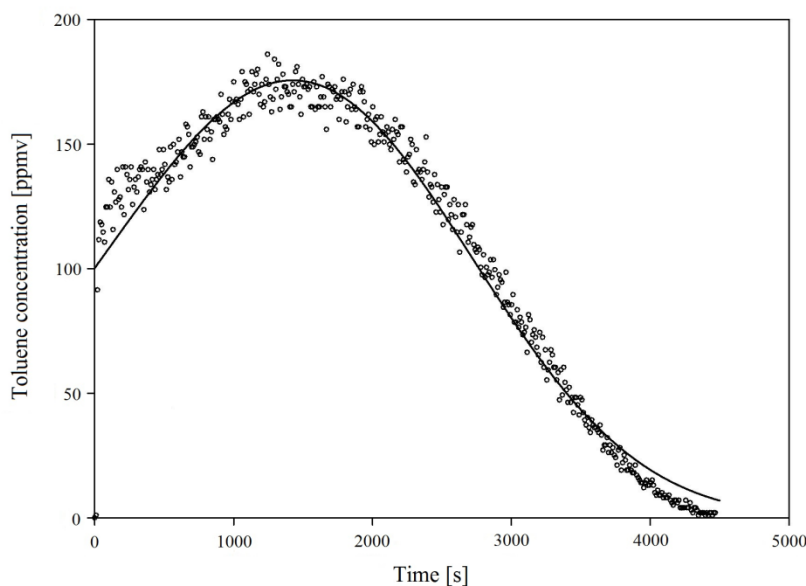
Figure 4.12 TPD of toluene (experimental points and simulation line) over ACF-1-673K (3 K min^{-1}, 100 cm^3 min^{-1})

As can be seen the simulation fits very well the experimental data suggesting that the toluene desorption from ACF-1-673K follows a 1st order kinetic regime. An apparent activation energy of desorption is found at 25 kJ mol^{-1}. This value is significantly lower than the adsorption enthalpy found with the D-R isotherm modelling. Moreover, the simulated value is lower than the heat of condensation (-38 kJ mol^{-1}) which does not have any physical meaning. Since ACF-1-673K presents a narrow microporosity (**Table 4.1**), it is supposed that internal mass transfer may influence the desorption process explaining the low activation energy. It corresponds to a global kinetic constant that combines the adsorption enthalpy and a mass transfer coefficient.

To overcome the effect of mass transfer and determine the adsorption enthalpy, only the lower temperature part of the TPD profile was used for simulations. It was supposed that the mass transfer influence on the desorption rate is negligible due to the low kinetic of

desorption at low temperature. However, for ACF-1-673K, the simulation did not give meaningful results suggesting that mass transfer limitations are not negligible even at low temperature.

Unlike ACF-1-673K a nice fitting was obtained by simulating only the first part of the desorption curve for ACF-2-673K. As an example, a TPD profile with the ramp of 3 K min^{-1} is presented in **Figure 4.13**. The influence of mass transfer on the rate of desorption encountered for ACF-1-673K does not appear with ACF-2-673K because of its wider micropores (**Table 4.1**). In the low temperature range, the desorption rate depends only on the kinetics and the adsorption enthalpy can then be obtained.
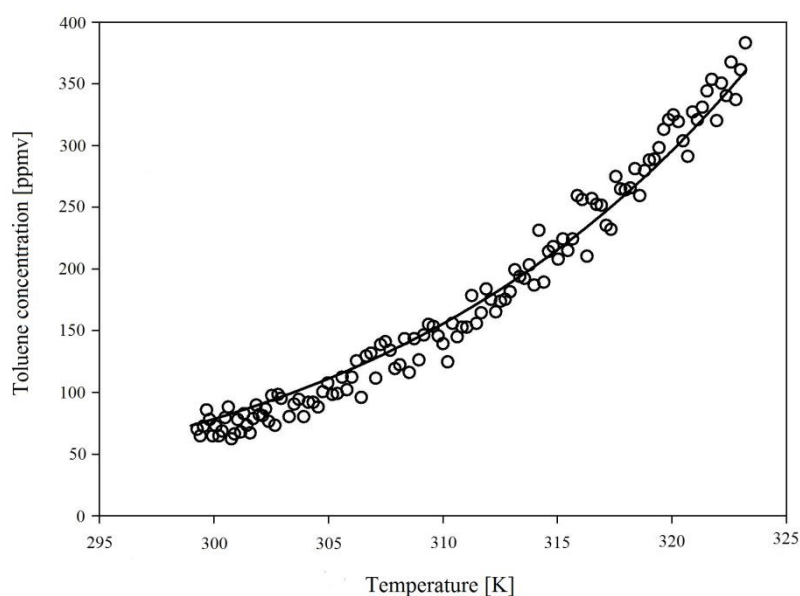
Figure 4.13 Simulation of TPD profile of initial toluene desorption over ACF-2-673K (3 K min^{-1}, 100 cm^3 min^{-1})

The simulation of the TPD profiles was performed for different temperature ramps (3-30 K min^{-1}) for the toluene desorption up to 320 K. This corresponds to 10% desorbed and the micropore filling was supposed constant. With these assumptions, an enthalpy of adsorption of -53 kJ mol^{-1} was calculated. This value was identical for all the temperature ramps justifying the assumptions used. Moreover, as presented in **Table 4.4**, the adsorption enthalpy obtained for ACF-2-673K is very close the adsorption enthalpy calculated from the adsorption isotherms, also confirming a suitable isotherm modelling. The pore filling mechanism assumed in D-R and D-A model is therefore likely to occur.

Table 4.4. Adsorption enthalpy determined by TPD and isotherm modelling

Sample	ΔH^{0}_{ads} [kJ mol^{-1}]	
	Isotherms	TPD
ACF-1-673K	-67±6	-
ACF-2-673K	-57±2	-53±3

4.4 Conclusions

Adsorption of toluene was studied over two different ACFs: ultramicroporous ($d_p < 1$ nm) and supermicroporous ($d_p \sim$ 1-2 nm) adsorbents with similar surface chemistry (O-containing groups). The effect of the surface morphology on the toluene adsorption capacity was addressed by measuring the adsorption isotherms and temperature-programmed desorption (TPD) profiles. Dubinin-Radushkevich (D-R) and Dubinin-Astakhov (D-A) model based on a pore filling mechanism were consistent with the experimental adsorption isotherms. Based on this modelling the characteristic energy and the adsorption enthalpy were

calculated for both ACFs revealing that the toluene is more strongly adsorbed in ultramicroporous ACFs as compared to supermicroporous one. Therefore, for practical applications especially at high adsorption temperature the ultramicroporous ACF is the adsorbent of choice.

Toluene TPD experiments were carried out over both samples and the TPD profiles were successfully simulated in the low temperature (300-320 K) range where effect of mass-transfer on desorption kinetics is negligible. The calculated adsorption enthalpy was close to the values determined from the D-R and D-A isotherm model for ACF-2.

5 Effect of ACFs Surface Chemistry on Toluene and Acetaldehyde Adsorption

The effect of oxygen surface functionalities of ACFs on the adsorption of toluene and acetaldehyde at low concentrations (~80 ppmv) is presented in this chapter. The oxygen surface containing groups were obtained by nitric acid oxidation and was characterized by monitoring the CO/CO_2 evolved during temperature-programmed desorption. The effect of oxidation on the porosity was assessed by N_2 physisorption. The adsorption capacities of original and oxidized ACFs were evaluated for toluene and acetaldehyde. These results were explained based on the oxygen content of the ACFs surface.

5.1 Introduction

Oxygenated VOC contains an oxygen atom in their molecular structure. They are used as solvents or can be found as combustion by-products [214]. The presence of an oxygen atom creates a dipolar moment which drastically decreases the removal capacity of AC as compared to non-polar VOC due to the non-polar properties of the graphene layers [215].

As shown in **Chapter 4**, ACFs are efficient adsorbents for high boiling point non-polar VOC such as toluene and the influence of their surface morphology on the adsorption capacity was established. The modification of the ACFs surface chemistry is suitable for the increase of the VOC removal capacity [106]. The addition of oxygen containing groups is a common method used to reduce the hydrophobicity of ACFs [117]. Depending on the oxidative treatments presented in **Section 2.3.3**, O-containing surface functionalities can be obtained in different proportions [216].

The effect of the surface oxygen content of ACFs on the adsorption capacity towards oxygenated VOC was reported by Mangun *et al.* [124]. Due to their hydrophilic character AC with larger oxygen content showed increased adsorption capacity towards methanol [125, 128], acetone [217] or butanol [218]. Specific interactions between the oxygenated VOC and the O-containing groups via hydrogen bonding were identified [106]. On the opposite, the presence of hydrophilic groups on the ACFs surface was reported to decrease the removal of non-polar VOC [100, 111]. Similar to non-polar VOC, the effect of the AC morphology was also reported to influence the adsorption capacity towards oxygenated VOC such as diethyl ether [219] and phenol [220].

This chapter reports the effect of nitric acid oxidative treatment on the removal of acetaldehyde and toluene used as a model for polar and non-polar VOC, respectively. The

adsorption capacity from diluted streams (80 ppmv) is measured over ACFs oxidized to different extent. A systematic evaluation of the surface oxygen of the oxidized ACF was carried out by TPD. The effect of oxidation treatment on the pore volume, the specific surface area and the pore size was assessed by N_2 adsorption.

5.2 Experimental

Materials

Original ACFs are described in **Section 3.1.1** and oxidized ACFs were prepared following the procedure presented in **Section 3.1.2**.

ACFs Characterization

The ACFs morphology was characterized by N_2 adsorption at 77 K. The ACFs surface chemistry was assessed by TPD of the oxygen-containing groups of the oxidized ACFs. During TPD, apart from CO and CO_2, water and NO were detected in negligible amounts below 673 and 473 K, respectively. The low amount of water was attributed to physisorbed molecules whereas traces of NO were probably coming from HNO_3 remaining after rinsing. Detailed description of the apparatus used and the conditions applied can be found in **Section 3.2**.

Dynamic Adsorption Measurements

Toluene and acetaldehyde adsorption capacity were obtained at 298 K and partial pressure of 8 Pa. 10±0.1 mg and 20±0.1 mg of original and oxidized ACF-2 were used for toluene and acetaldehyde respectively. The experimental setup used for adsorption experiments was presented in **Section 3.4.1** and the calculation details in **Section 3.4.2**.

5.3   Results and Discussion

5.3.1   Characterization of ACFs

Morphology

The morphology of the original ACFs materials consisting of elementary filaments of ~10 μm diameter was presented in **Figure 4.1**. Their morphology was kept upon nitric acid treatment. **Figure 5.1** presents typical N_2 adsorption isotherms over the samples used in this study. All isotherms exhibit a type I profile typical for microporous adsorbents according to the IUPAC classification [12] indicating that the material remains microporous after oxidative treatment. A gradual decrease of the porosity is observed by increasing the nitric acid treatment time.
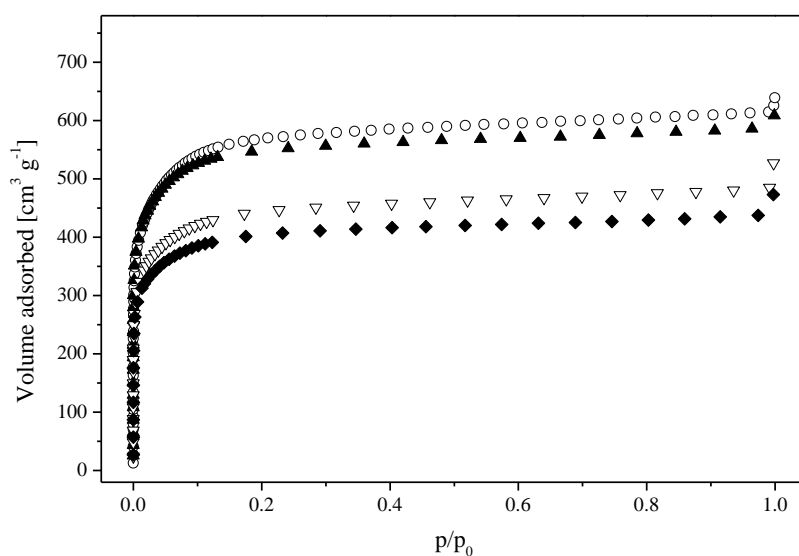
Figure 5.1 N_2 adsorption isotherms (77 K) for ACF-2 (○), ACF-2/HNO$_3$-1m (▲), ACF-2/HNO$_3$-15m (▽) and ACF-2/HNO$_3$-30m (♦)

In order to evaluate the morphology of ACF-2 without treatment and treated by HNO_3 a pore size determination was carried out via comparative α-plot [71]. The non-porous reference material was described in **Chapter 4**.
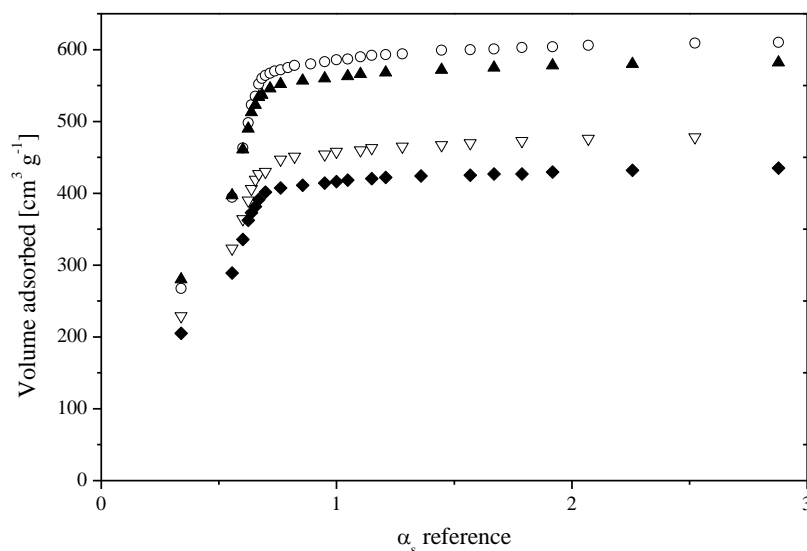
Figure 5.2 α-plot of ACF-2 (○), ACF-2/HNO_3-1m (▲), ACF-2/HNO_3-15m (▽) and ACF-2/HNO_3-30m (♦)

The α-plots obtained for ACF-2 samples (**Figure 5.2**) are almost linear and constant at α > 1 hence no increase of the adsorption capacity occurs at high α > 1. This implies that the external surface area is relatively small as compared to the total surface area meaning that most of the surface is due to the pores [58]. It confirms that all adsorbents are microporous with a relatively narrow pore size distribution.

The curve slope is changing in the range of 0.5 < α < 1 for original and nitric acid treated ACFs. As presented in **Chapter 4.3.1**, ACF-2 was found to be supermicroporous (d_p ~1-2 nm). Since the slope change of the α-plots for nitric acid treated ACF-2 occurred at the

same α_s reference (0.7), it is concluded that the oxidative treatment does not affect the micropore diameter of the ACFs.

The specific surface area of all samples was calculated through the BET equation using N_2 adsorption data [55]. The equation was linearized in the partial pressure range of 0.01-0.1. As shown in **Table 5.1**, in all cases the *C* values obtained are > 100. The *C* value of the BET equation which can qualitatively describe the pore size remained approximately constant for original and nitric acid treated ACF-2 signifying a constant micropore size and confirming the interpretation of the α-plot. Similar results were already obtained for oxidized activated carbon [106, 120, 121]. Therefore, HNO_3 treatment reduces both the specific surface area and pore volume of ACF-2 but its pore structure remains in the micro-range (< 2 nm) (**Figure 5.1**).

Table 5.1 Characteristics of ACFs adsorbents

Sample	SSA_{BET} [$m^2\,g^{-1}$]	*C* BET equation	Pore volume [$cm^3\,g^{-1}$]
ACF-2	2170±50	280	0.94±0.02
ACF-2/HNO$_3$-1m	2100±50	400	0.90±0.02
ACF-2/HNO$_3$-15m	1670±50	370	0.74±0.02
ACF-2/HNO$_3$-30m	1530±50	420	0.67±0.02

Surface Functionalities

O-containing groups on the ACF-2 surface were characterized by TPD with the outlet composition monitored by the mass spectrometer. Two major molecules desorbing from the ACFs surface are CO and CO_2 although traces of H_2O and NO were also detected. CO_2 is

assumed to originate from decomposition of carboxylic (373-673 K), lactone (463-923 K) and anhydride groups (623-900 K), whereas CO is a product of decomposition of anhydride (623-900 K) phenolic (873-973 K), carbonyl (973-1173 K) and quinone groups (973-1173 K) [117].
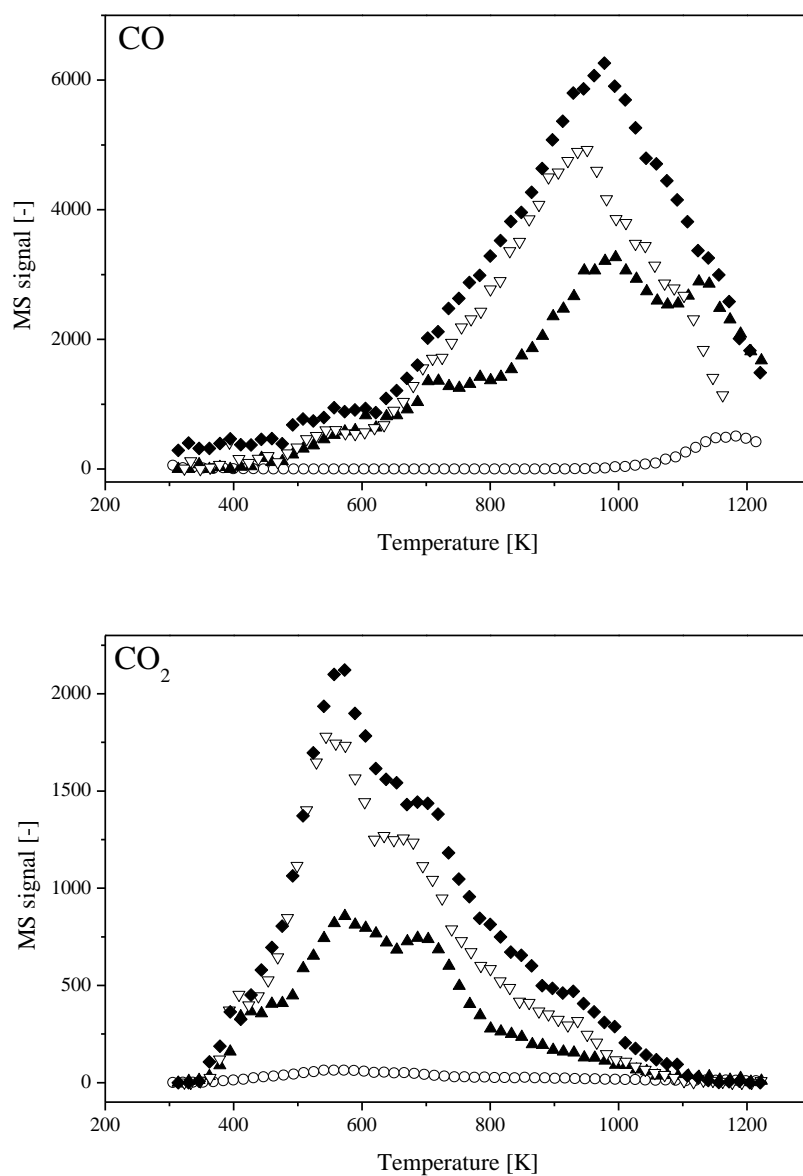
Figure 5.3 TPD profiles of ACF-2 (○), ACF-2/HNO$_3$-1m (▲), ACF-2/HNO$_3$-15m (▽) and ACF-2/HNO$_3$-30m (♦) (10 K min^{-1}, 50 cm^3 min^{-1})

Figure 5.3 shows TPD profiles of original and oxidized samples. As can be seen, treatment of ACF-2 by nitric acid drastically increases the surface oxygen content. Even a short treatment time (1 min) in boiling nitric acid leads to a large increase in surface oxygen content. All type of surface O-containing groups is created by such treatment. Anhydride groups are identified by the broad shoulder at 800 K on both CO and CO_2 desorption pattern. As compared to the other desorption peaks, the quantity of anhydride groups is relatively low. Particularly visible on the ACF-2/HNO_3-1m pattern, the CO desorption peaks at 1000 K and 1150 K indicate the creation by the oxidative treatment of phenolic and carbonyl or quinone groups, respectively. For longer treatment time, due to the higher amount of groups created, the two decomposition peaks are not distinguishable. The CO_2 decomposition pattern of all oxidized samples revealed that carboxylic groups are created in a large amount although a small amount was already present on both original samples (550 K). Decomposing at higher temperature (700 K), lactone groups are created by the oxidative process in a smaller extent.

The integration of the CO and CO_2 concentration curves gives the surface oxygen contents of the samples which are reported in **Table 5.2**. For original and nitric acid treated samples the amount of evolved CO is comparable to the amount of CO_2 confirming that all type of O-containing groups are present on the ACFs surface. Nitric acid treatment increased considerably the oxygen content in ACF-2. Indeed, ACF-2/HNO_3-30m has 20 times more surface O-containing groups as compared to the original ACF-2.

Table 5.2 Quantitative characterization of ACFs surface oxygen groups

Sample	CO_2 [μmol g^{-1}]	CO [μmol g^{-1}]	Total oxygen content [μmol g^{-1}]
ACF-2	240	180	420±50
ACF-2/HNO$_3$-1m	2200	2800	5000±100
ACF-2/HNO$_3$-15m	4000	3500	7500±100
ACF-2/HNO$_3$-30m	4000	4200	8200±100

5.3.2   Toluene Adsorption

Toluene breakthrough curves are shown in **Figure 5.4**. The adsorption capacity of the ACFs materials was determined by numerical integration as described in **Section 3.4.3**.
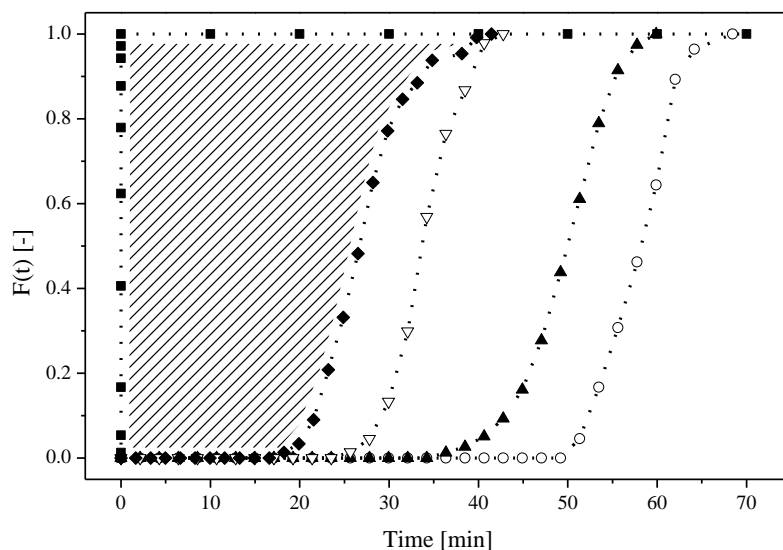
Figure 5.4 Toluene (80 ppmv) breakthrough curves for ACF-2 (○), ACF-2/HNO$_3$-1m (▲), ACF-2/HNO$_3$-15m (▽), ACF-2/HNO$_3$-30m (♦) and 2% (v/v) Argon (■). Total flow rate (STP) 300 cm^3 min^{-1} (298 K)

As shown in **Figure 5.4**, ACF-2 is efficient for toluene adsorption even at short contact time (~20 ms). The outlet toluene concentration is zero indicating its total adsorption before the breakthrough at about 50 minutes. The toluene adsorption capacity obtained is 51 wt. %. This value is in agreement with already published results [101].

The modification of ACF-2 by nitric acid gradually decreases the toluene adsorption capacity with the HNO_3 treatment time (**Figure 5.5**). From 51 wt. % for original ACFs the adsorption capacity drops to 44, 30 and 26 wt. % for ACF-2/HNO_3-1m, ACF-2/HNO_3-15m and ACF-2/HNO_3-30m, respectively. The breakthrough curve shape of the oxidized samples is identical to the original sample suggesting similar adsorption kinetics. This observation can be explained by the constant micropore size upon nitric acid treatment (**Figure 5.2**). The lower adsorption capacity of the treated ACFs is explained by their lower specific surface areas (**Table 5.1**) and higher oxygen contents (**Table 5.2**). It is known that a lower specific surface area leads to a lower adsorption capacity for similar pore sizes [101], whereas O-containing groups weaken the interaction between benzene ring of toluene molecules and graphite layers of ACFs [100]. To quantify both effects, the adsorption capacity is normalized by the specific surface area of the adsorbent. The normalized efficiencies reflect the effect of the O-containing groups. It decreases with nitric acid treatment (**Figure 5.5**). It is then concluded that the presence of O-containing groups decreases the adsorption capacity towards toluene.
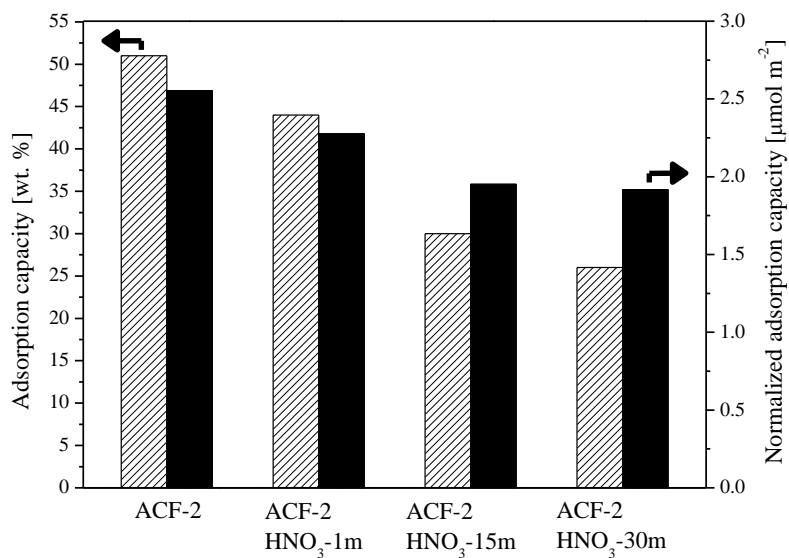
Figure 5.5 Toluene (80 ppmv) adsorption capacities as a function of nitric acid treatment

(298 K)

To quantify the effect of the O-containing groups, the adsorption normalized by the specific surface area of the different samples is plotted on the oxygen surface concentration. The results presented in **Figure 5.6** show a linear trend, confirming that polar groups weaken the interactions between toluene and ACFs surface.
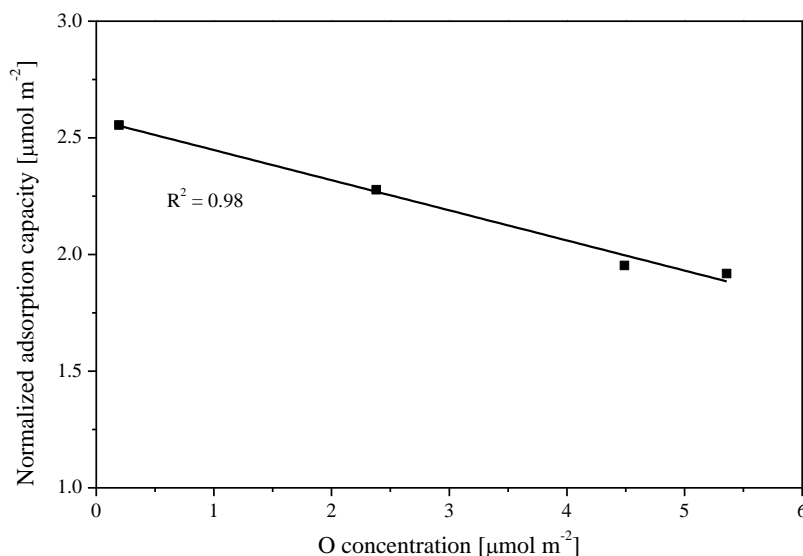
Figure 5.6 Normalized toluene (80 ppmv) adsorption capacities as function of the O-concentration of ACF-2 (298 K)

5.3.3   Acetaldehyde Adsorption

The effect of ACFs surface functionalities on the acetaldehyde adsorption was studied using original and HNO$_3$ treated ACF-2. At similar concentration (80 ppmv), much lower acetaldehyde adsorption capacities as compared to toluene were measured for original ACF-2: 0.3 wt.%, and 51 wt.%, respectively. Despite their lower adsorption capacity, the breakthrough curves in **Figure 5.7** confirm a complete acetaldehyde removal (outlet concentration is zero until breakthrough). Moreover, the steepness of the breakthrough curve indicates fast adsorption kinetics. Similarly to toluene, the modification of the fibers by oxidative treatment does not influence the adsorption kinetics but only the total adsorption capacity. Low adsorption capacity towards acetaldehyde was already reported qualitatively for AC [129] and ACFs [106]. Similarly to previously published results, oxidized samples demonstrated larger acetaldehyde adsorption capacities. The O-containing groups of the

activated carbon surface were suggested to enhance the acetaldehyde adsorption as compared to original samples.
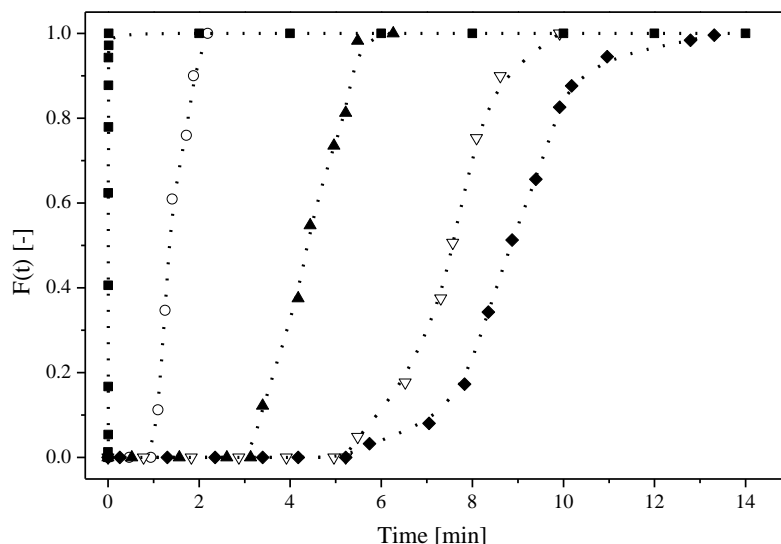
Figure 5.7 Acetaldehyde (80 ppmv) breakthrough curves for ACF-2 (○), ACF-2/HNO$_3$-1m (▲), ACF-2/HNO$_3$-15m (▽), ACF-2/HNO$_3$-30m (♦) and 2% (v/v) Argon (■). Total flow rate (STP) 300 cm^3 min^{-1} (298 K)

The adsorption capacity as a function of the oxygen surface concentration is presented in **Figure 5.8** showing its proportionality to the oxygen surface concentration. Higher adsorption capacity is obtained for larger O-concentration hence, samples treated longer time by nitric acid shows larger adsorption capacity. A maximum adsorption capacity of 2.2 wt.% is reported for ACF-2/HNO$_3$-30m at 80 ppmv. Since all types of oxygen functionalities are created during the nitric acid treatment, it is not possible to indicate which surface oxygen containing groups contribute the most to the acetaldehyde adsorption. **Figure 5.8** also shows that at higher acetaldehyde partial pressure the adsorption capacity increases for similar O-

concentration. The acetaldehyde adsorption mechanism on surface functional groups of activated carbon has been already reported [129]. It is suggested that the aldehyde group interacts with O-containing groups of activated carbon via hydrogen bonding. The results presented in **Figure 5.8** are consistent with this mechanism.
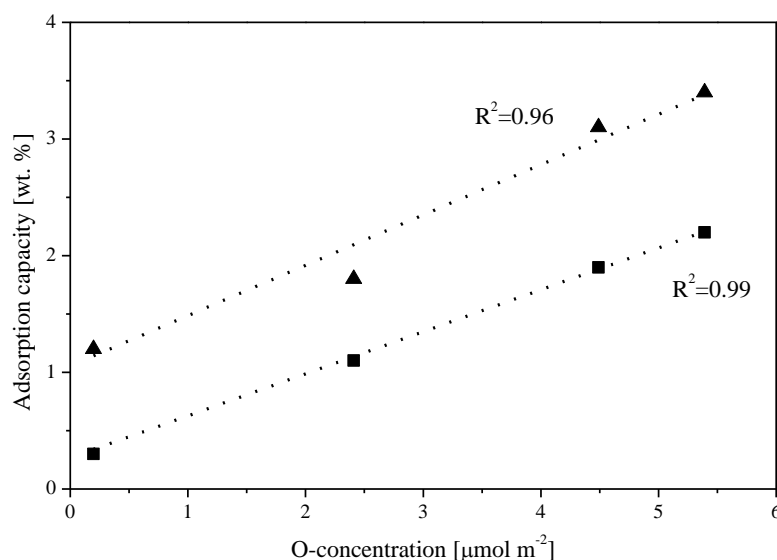
Figure 5.8 Acetaldehyde adsorption capacity as a function of oxygen surface concentration for original and HNO$_3$ treated ACF-2. (■) 80 ppmv acetaldehyde, (▲) 150 ppmv acetaldehyde

The amounts of acetaldehyde adsorbed are around 10 times lower than the O-content. with 0.07-0.5 mmol g^{-1} and 0.4-8 mmol g^{-1}, respectively. The coverage of the active sites by acetaldehyde remains relatively low at working partial pressure of 80 ppmv. The surface coverage increases with the acetaldehyde partial pressure confirming that the maximum adsorption capacity is not reached at the working pressure. Hence some adsorption sites remained unused due to the adsorption equilibrium.

5.4 Conclusions

The effect of ACFs surface chemistry on the adsorption of toluene and acetaldehyde was studied at low partial pressure (80 ppmv). By varying the duration of HNO_3 treatment time, a series of microporous ACFs with various surface oxygen contents and constant micropore size was obtained. The surface oxygen content was assessed by temperature-programmed desorption of CO/CO_2. Toluene and acetaldehyde adsorption capacity were shown to strongly depend on the surface functionalities. Larger surface O-concentration increases acetaldehyde removal but decreases the toluene adsorption capacity. This effect was rationalized by suggesting different type of interactions with the activated carbon surface. Acetaldehyde is adsorbed via hydrogen bonding with the O-containing groups while toluene adsorption occurs preferentially on hydrophobic carbon surface.

6 Amine Modified ACFs for Formaldehyde Adsorption

In this chapter the results of ACFs surface modification to create specific interactions with formaldehyde are reported. Diethylene triamine (DETA) is deposited on the ACFs surface as a thin liquid film. Formaldehyde adsorption was carried out over several DETA modified ACFs showing a considerable increase of the adsorption capacity as compared to original ACFs. A mechanism of adsorption was suggested and a study of the adsorbent stability was performed.

6.1 Introduction

As discussed in **Chapter 2** adsorption capacity towards polar VOC can be enhanced by the functionalization of the adsorbent surface. Besides O-containing groups, surface specific interactions with the adsorbate can be created by the introduction of nitrogen groups. Such functionalization can represent a valuable alternative for the removal of formaldehyde because of its low boiling point (254 K) and polarity [221]. Hence, this chapter reports formaldehyde removal over functionalized ACFs.

Formaldehyde adsorption by various AC has been studied by several research groups. High content of functional oxygen hydrophilic groups [222, 223] and large pore volume [224] were shown to increase the formaldehyde removal efficiency. The surface functionalization of AC and ACFs by nitrogen-containing groups was also studied by several groups and significant increase of the adsorption capacity was reported [131, 134]. Similarly, graphite oxide containing amino groups was reported as an effective adsorbent for formaldehyde abatement [146, 147]. Amorphous silica [144], MCM-41 and zeolite HY [225] were also functionalized with various amine containing molecules to efficiently adsorb formaldehyde. Finally AC was modified by hexamethylene diamine for gas phase formaldehyde removal. A significant improvement of the adsorption capacity was reported upon hexamethylene diamine deposition [141].

Undoubtedly the presence of the amine group on the adsorbent surface enhances the formaldehyde removal. In this chapter, the synthesis of a novel adsorbent combining ACFs and diethylene triamine (DETA) is reported. A liquid layer of DETA is deposited on the surface of the ACFs and the adsorbent was found efficient for formaldehyde removal. DETA is an organic high boiling point molecule (477 K) presenting a high density of amine groups per unit of weight. Due to its low volatility DETA evaporation from the ACFs does not occur

at room temperature. The effect of DETA deposition on the ACFs morphology and its performance towards formaldehyde adsorption are evaluated.

6.2 Experimental

Materials

Original and DETA modified ACF-2 are used in this chapter. Original ACFs are described in **Section 3.1.1**. DETA modified ACF-2 was synthesized following the procedure detailed in **Section 3.1.2**.

Adsorbent Characterization

The SSA and the porosity of the adsorbent were determined by physical adsorption of N_2 at 77 K. Detailed description of the apparatus used and the conditions applied can be found in **Section 3.2**.

Adsorption Measurements

Formaldehyde adsorption capacity was evaluated at 50 ppmv and 298 K. 20 ± 0.1 mg of original and DETA modified ACF-2 were used for formaldehyde adsorption. Prior to adsorption the samples were outgassed at 373 K for 30 minutes. The experimental setup used for adsorption experiments was presented in **Section 3.4.1** and the calculation details in **Section 3.4.2**.

6.3 Results and Discussion

6.3.1 Characterization of ACFs

The morphology of the original ACFs materials consisting of elementary filaments of ~10 μm diameter was presented in **Figure 4.1**. Their morphology was kept upon DETA

deposition. The porosity of original and DETA (5 to 35 wt.%) modified ACF-2 was assessed by N_2 physisorption at 77 K. As can be seen in **Figure 6.1** the adsorption isotherms of all adsorbents exhibit a type I profile signifying microporous material. Although a decrease of the pore volume is noticed upon DETA deposition suggesting a gradual filling of the micropores, the microporosity is still present even for ACF-2/35%DETA.
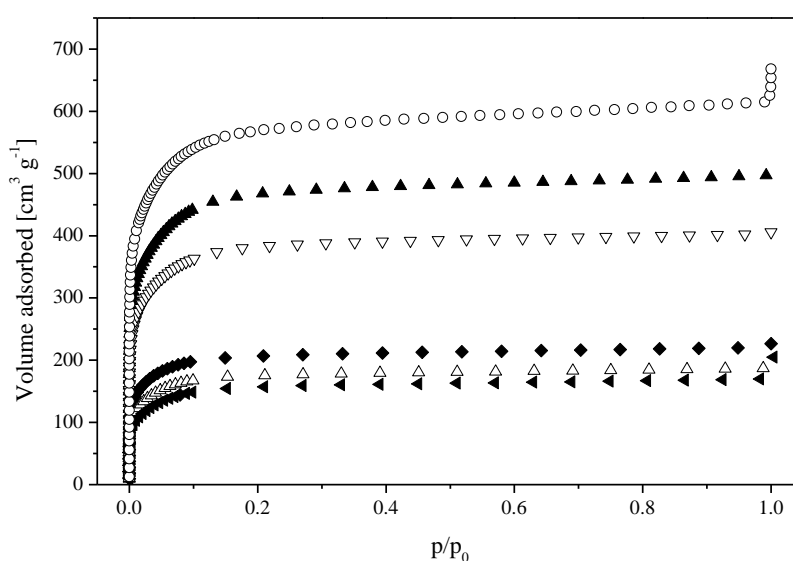
Figure 6.1 N_2 adsorption isotherms (77 K) for ACF-2 (○), ACF-2/5%DETA (▲), ACF-2/15%DETA (▽), ACF-2/20%DETA (♦), ACF-2/25%DETA (△) and ACF-2/35%DETA (◄)
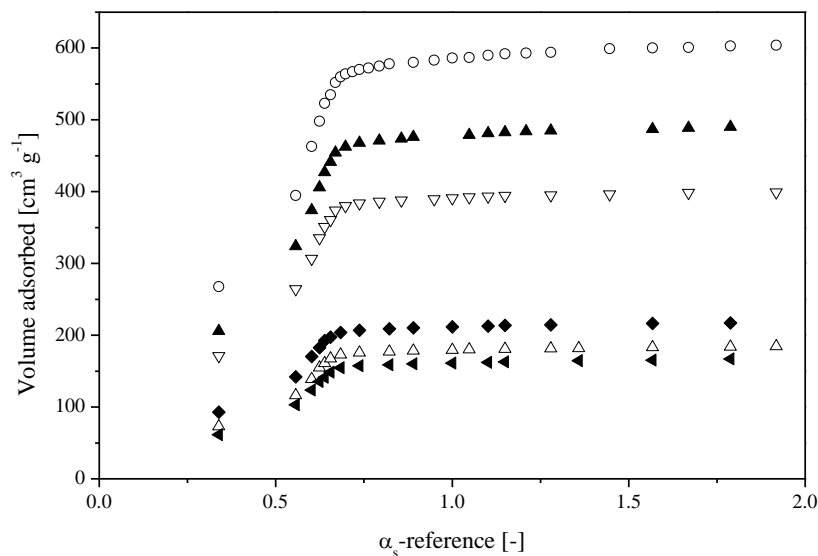
Figure 6.2 α-plot of ACF-2 (○), ACF-2/10%DETA (▲), ACF-2/15%DETA (▽), ACF-2/20%DETA (♦), ACF-2/25%DETA (△) and ACF-2/35%DETA (◄)

The assessment of the porosity was also performed via the α-plot presented in **Figure 6.2**. As can be seen α-plot of all adsorbents present a slope change at the same α_s-references: 0.7 suggesting similar pore size. Hence the deposition of DETA on ACF-2 does not influence the mean pore diameter.

The specific surface area of all samples was calculated through the BET equation using N_2 adsorption data [55]. The equation was linearized in the partial pressure range of 0.01-0.1 for ACF-2 and ACF-2/DETA (all loadings). As presented in **Figure 6.3**, the specific surface area was found to decrease with the DETA loading along with the pore volume.
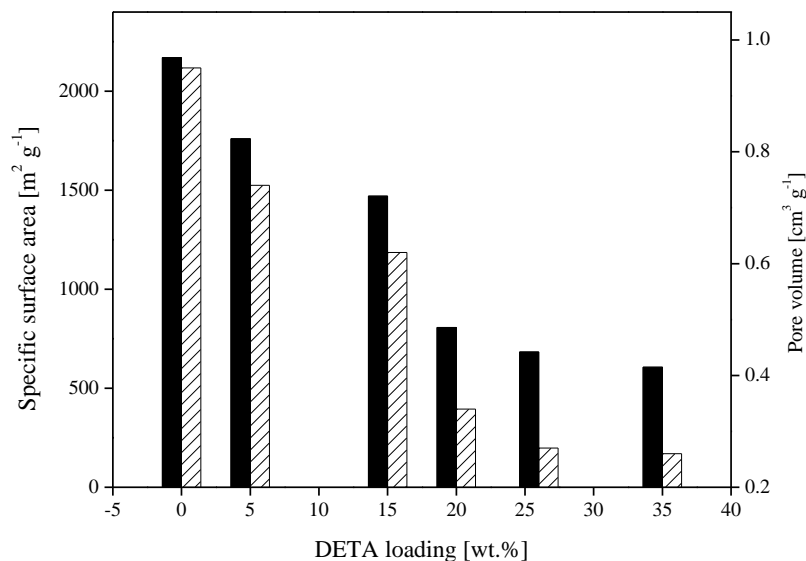
Figure 6.3 Influence of the DETA loading on the specific surface area and the pore volume of

the adsorbent

As can be observed the specific surface area and the pore volume decreases with the DETA loading up to 20 wt.% DETA whereas at higher loading (26 and 35 wt.%) the decrease is less pronounced. This phenomenon along with the constant micropore size upon DETA loading (**Figure 6.2**) suggests a micropore filling and not a layer by layer addition of DETA which would result in a decrease of the pore volume and the pore width simultaneously. Assuming slit-shaped micropores as often reported for ACFs [226] we suggest that the micropores are gradually filled with DETA leading to an important decrease of the SSA at low loading. Moreover since DETA molecule is relatively large as compared to the size of the bottom of the micropore, the volume is not efficiently occupied. This assumption can be verified by comparing the theoretical decrease of the pore volume and the measured one (**Table 6.1**). Taking the liquid density of DETA (0.995 g cm^{-3}), 20 wt.% loading should reduce the initial pore volume from 0.94 to 0.74 cm^3 g^{-1} whereas the pore volume measured is 0.34 cm^3 g^{-1}. It is concluded that the pore volume is not efficiently occupied by DETA.

At higher DETA loading (25-35%) the micropores are filled at 70 % and the addition of supplementary DETA only slightly reduces the SSA and the pore volume because of a more efficient arrangement of DETA favored by a larger pore diameter at the entrance. The optimum DETA loading is achieved at 20 wt.% since an almost constant specific surface area is reported for higher loadings (**Figure 6.3**). A schematic representation of the pore filling by DETA is shown in **Figure 6.4**.

| 5% DETA | 20% DETA | 35% DETA |

Available pore volume
Available SSA
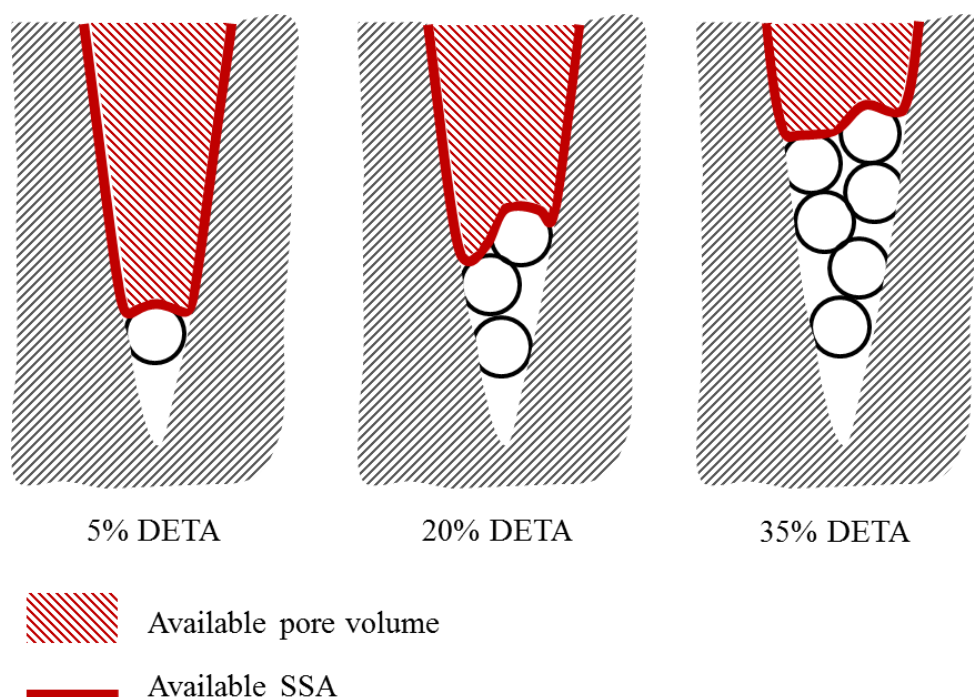
Figure 6.4 Schematic representation of DETA micropore filling

The characteristics of original and modified samples are summarized in **Table 6.1**. As can be seen the DETA loading does not influence the *C* value of the BET equation confirming a constant pore width and supporting the DETA pore filling mechanism

Table 6.1 Characteristics of ACFs adsorbents

Sample	SSA$_{BET}$ [m^2 g^{-1}]	C	Micropore volume [cm^3 g^{-1}]
ACF-2	2170±50	280	0.94±0.02
ACF-2/5%DETA	1760±50	360	0.74±0.02
ACF-2/15%DETA	1460±50	280	0.64±0.02
ACF-2/20%DETA	810±30	260	0.35±0.02
ACF-2/26%DETA	680±30	240	0.27±0.02
ACF-2/35%DETA	610±30	215	0.26±0.02

6.3.2   Formaldehyde Adsorption

Formaldehyde adsorption (50 ppmv) over original and DETA modified ACF-2 is shown in **Figure 6.5**. As can be seen the breakthrough curve of original ACF-2 occurs extremely quickly implying a very small adsorption capacity (0.1 wt.%) of non-functionalized ACFs. This result is in line with the performance reported in the literature [131, 134, 223].

The deposition of 5% DETA on the fibers leads to a large increase of the formaldehyde abatement (2.5 wt.%). The formaldehyde signal remains at zero during 15 minutes signifying a total removal. Moreover, the relative steepness of the breakthrough curve suggests fast adsorption kinetics.
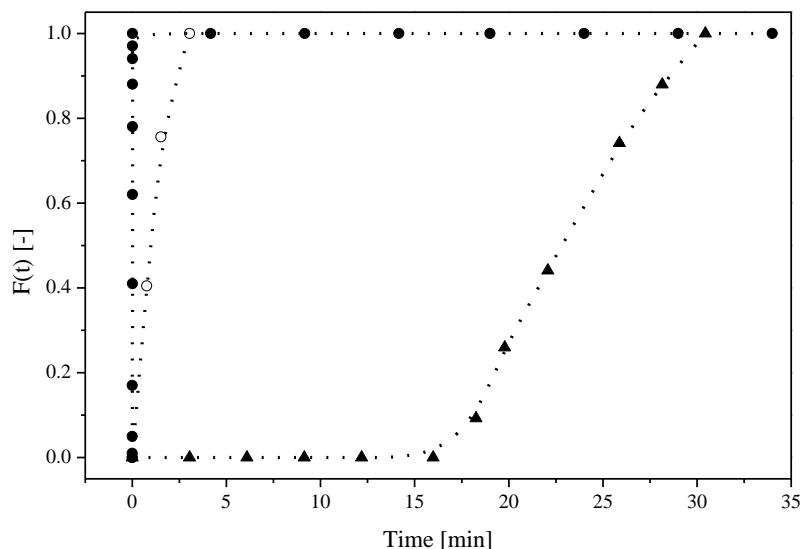
Figure 6.5 Formaldehyde (50 ppmv) breakthrough curves for ACF-2 (○), ACF-2/5% DETA (▲) and 2% (v/v) Argon (■). Total flow rate (STP) 300 cm^3 min^{-1} (298 K)

The large increase of the adsorption capacity noticed for ACF-2/5%DETA indicates the importance of the surface chemistry for formaldehyde adsorption [221]. Similarly to acetaldehyde removal on HNO$_3$ treated ACFs (**Chapter 5**) the surface chemistry appears to be the main parameter for the removal of oxygenated VOC. The micropore structure is apparently less important.

The importance of amine groups for the removal of formaldehyde was reported for several adsorbents and an increase of the formaldehyde adsorption capacity was noticed [141, 147]. Matsuo *et al.* suggested a Schiff base interaction mechanism between the aldehyde and the electron rich nitrogen atom of the amine group. In general the presence of basic functional groups enhances the interactions with formaldehyde [134, 227]. As compared to the other amine based adsorbents for aldehyde removal, the deposition of DETA on ACFs presents several advantages such as the high SSA of the ACFs and the high density of amine groups

per DETA molecule. Such properties allow a larger adsorption capacity as compared to the other adsorbents.

In order to increase the formaldehyde abatement capacity of the fibers, the loading of DETA was varied as shown in **Figure 6.6**.
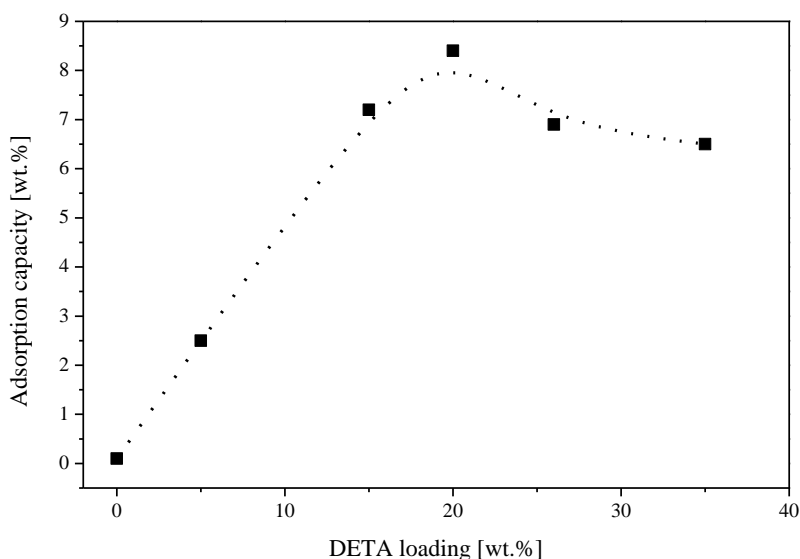
Figure 6.6 Influence of the DETA loading on the formaldehyde (50 ppmv) removal capacity

(298 K)

The increase of the DETA loading enhances linearly the formaldehyde adsorption capacity (loading < 20 wt.%) up to a maximum value of 8.6 wt.%. As can depicted in **Figure 6.6** further increase of the DETA loading leads to a slight decrease of the adsorption capacity. This phenomenon was already reported for hexamethylene diamine deposition on AC [141]. It was explained by the pore volume decrease at high loading. Hence the optimum DETA loading for ACF-2 is 20%. Such observation along with the DETA pore filling mechanism

suggested in **Figure 6.4** indicates that formaldehyde is adsorbed on the DETA surface and does not penetrate into the liquid phase in the microporosity.

Interestingly 20 wt.% DETA is also the maximum loading which strongly influences the SSA (**Figure 6.3**). It is then suggested that the maximum DETA surface is reached at 20 wt.% for ACF-2. Higher DETA loading does not create more accessible adsorption sites.

6.3.3 Adsorbent Stability

The ACF-2/20% DETA being a promising adsorbent for formaldehyde removal has been evaluated for its stability in time. Since amine based adsorbents are used for CO_2 capture [228-230], deactivation of ACF-2/20%DETA in ambient atmosphere towards formaldehyde adsorption may occur during storage.
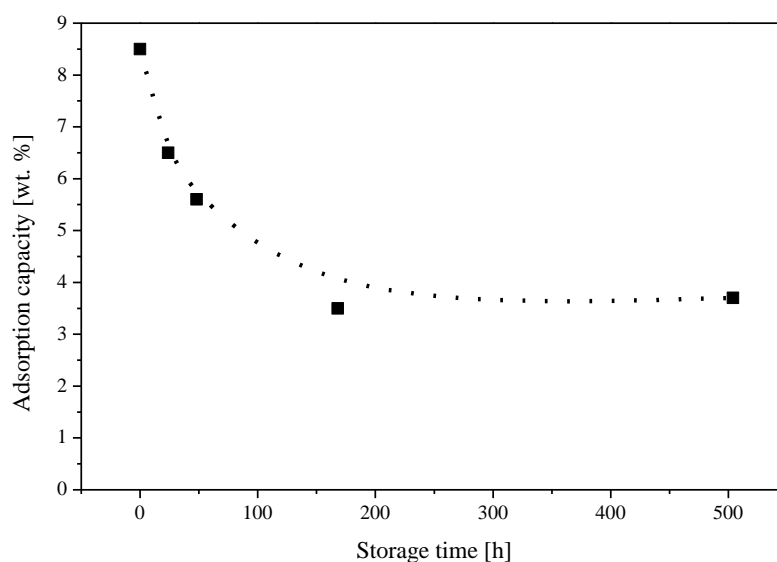
Figure 6.7 Formaldehyde (50 ppmv) adsorption capacity of ACF-2/20%DETA after storage

(298 K)

As can be seen in **Figure 6.7** a deactivation of ACF-2/20%DETA towards formaldehyde adsorption takes place during storage. The adsorption capacity towards formaldehyde drops from 8.6 wt.% to approximately 3.8 wt.% during the first 200 hours but reaches a plateau suggesting long term stability. As compared to toluene adsorption on ACF (**Chapter 4**) the capacity of the ACF-2/20%DETA after stabilization is about 10-fold smaller in mass and 5 times less in mole at the same partial pressure (50 ppmv). However formaldehyde has a much lower boiling point (254 K) as compared to toluene (384 K). Compared to acetaldehyde removal over HNO_3 treated ACF-2 (**Chapter 5**), the performance of ACF-2/20%DETA is much higher despite the lower partial pressure. An acetaldehyde removal capacity of 2.2 wt.% was reported at 80 ppmv whereas the adsorption capacity of ACF-2/20%DETA is 3.8 wt.% at 50 ppmv. Moreover since formaldehyde is a lighter molecule the adsorption capacity measured in mole per gram is more than 2 times higher. Therefore DETA on ACFs is a promising adsorbent for formaldehyde removal despite its deactivation during the first hours of storage.

The deactivation is explained by two main reasons: either CO_2 is interacting with DETA or DETA reacts slowly with the oxygen groups present on the ACFs surface (**Chapter 4**). In both cases the amine sites becomes unavailable for formaldehyde.

To get an insight on the deactivation mechanism, a TPD experiment of ACF-2/20%DETA was carried out. The TPD profile is shown in **Figure 6.8**.
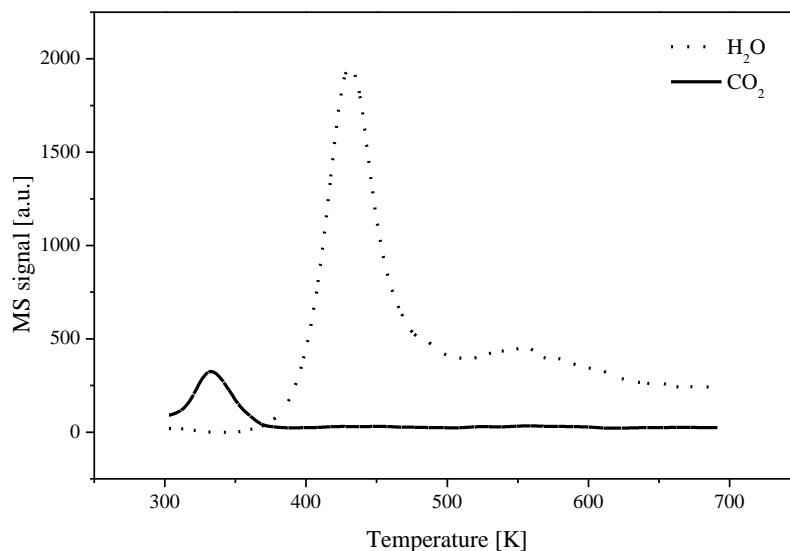
Figure 6.8 TPD profile of ACF-2/20%DETA (10 K min^{-1}, 50 cm^3 min^{-1})

As observed the desorption of both CO_2 and H_2O occurs during TPD of ACF-2/20%DETA. At low temperature (300-380 K), CO_2 is desorbed whereas at 440 K, a large desorption of water is noticed. This desorption peak is assigned to the reaction between amine and oxygen groups present the ACFs surface. A Schiff base reaction between the amines and the O-containing groups is suggested deactivating irreversibly the adsorbent. Since ACF-2/20%DETA was pretreated at 373 K before each adsorption experiment, CO_2 should not be the origin of the deactivation. The mechanism of the deactivation observed in **Figure 6.7** is suggested to occur via reaction between the ACFs support and the amine. The stabilization reached after 200 hours is then assigned to the reaction of all the O-containing groups with the amine.

6.4 Conclusions

A novel efficient adsorbent was developed for the removal of low concentration formaldehyde by deposition of a liquid layer of diethylene triamine (DETA) on the surface of

microporous ACFs. A set of adsorbents with different DETA loading was synthesized. A mechanism of DETA deposition on the ACFs surface was suggested based on microporosity analysis. An optimum DETA loading of 20 wt.% was determined and considerable adsorption capacity increase was noticed in comparison to original ACFs, 8.6 and 0.1 wt.%, respectively. A Schiff base mechanism between the amine groups of DETA and formaldehyde was suggested as the adsorption driving force. The stability upon storage of the developed adsorbent was addressed. After a 50 % deactivation during the first hours of storage, the adsorption capacity remains stable with 3.8 wt.% of formaldehyde removal. Irreversible interactions between the amines and the O-containing groups present on the ACFs surface were suggested.

7 ACFs Modified by Metal Oxide for Acetaldehyde Adsorption

This chapter presents novel efficient adsorbents for acetaldehyde removal from diluted gas streams (~1300 ppmv). Adsorbents combining the properties of ACFs and nanoparticles (NPs) of metal oxides (La_2O_3, CaO, MgO, ZnO, and Al_2O_3) have been developed. The adsorbents have been prepared by wetness impregnation of ACF using different precursors. The NPs are well dispersed and have average particle size below 2 nm. Depending on their basic properties metal oxide NPs show different adsorption capacity towards acetaldehyde. The NPs deposition provides up-to a 6-fold increase of the amount of acetaldehyde adsorbed as compared to the non-modified ACF. The effect of CO_2 in the gas stream on the adsorption capacity of NPs on ACFs was measured as well as the effect of the initial porosity of the ACFs. Finally, based on TPD experiments, an adsorption mechanism was suggested.

7.1 Introduction

As seen in **Chapter 5**, the original activated carbon showed a limited adsorption capacity towards diluted mixture of acetaldehyde. Although AC surface functionalization by addition of O-containing groups is a valuable strategy to increase its adsorption capacity, the hydrophilic groups are not selective to acetaldehyde and the adsorption capacity remains relatively low.

Other alternatives have been developed to adsorb acetaldehyde and other oxygenated VOC from gas streams such as AC functionalization via nitrogen containing groups (**Chapter 6**) or via adsorption by metal oxide particles [156]. Recently, metal oxide particles were reported to show particular reactivity towards a large range of VOC such as hydrogen sulfide [152] sulfur dioxide [155], ammonia [160] or acetaldehyde [231]. Among them nanocrystalline aerogels of alkaline earth oxides were proposed as effective adsorbents for aldehyde and alcohols. The large specific surface area of aerogel nano-particles (500 m^2 g^{-1}) was reported to enhance their adsorption capacity. The adsorption capacity of these materials was found to be larger compared to AC due to a multilayer dissociative adsorption of VOC [156]. In the particular case of acetaldehyde adsorption, MgO was reported as the most efficient.

Despite their high intrinsic adsorption potential, small nano-particles present tremendous pressure drop at high flow rates decreasing their potential for industrial application. However their deposition on a support presenting open macro-structure can represent a valuable alternative since it allows much higher gas velocity before observing a pressure drop [160]. Activated carbon is a material widely used in heterogeneous catalyst systems to support the catalysts active phase [232, 233]. Its well-developed microporosity

allows the formation of numerous NPs. Although rarely seen for adsorption purpose the combination of nano-particles supported by ACFs can represent a novel type of adsorbent.

The goal of this chapter was to develop novel ACFs-based structured adsorbents for efficient removal of acetaldehyde from low-concentrated streams. The approach is based on a conjugation of ACFs properties (large surface area and open macro-structure) with the reactivity of metal oxide NPs. Different metal oxide NPs were deposited on ACFs and their adsorption capacity towards acetaldehyde was evaluated and compared with original ACFs and nitric acid oxidized ACFs as presented in **Chapter 5**. The effect of CO_2 exposure on the adsorption capacity was also evaluated. Finally an adsorption mechanism is suggested.

7.2 Experimental

Materials

Original, oxidized and metal oxide modified ACFs are used in this chapter. Original ACFs are described in **Section 3.1.1**. Oxidized ACFs and metal oxide deposited on ACFs were prepared following the procedure presented in **Section 3.1.2**.

Adsorbent Characterization

The SSA and the porosity of the adsorbent were determined by physical adsorption of N_2 at 77 K. Metal oxide particle size was assessed by HRSTEM imaging. Detailed description of the apparatus used and the conditions applied can be found in **Section 3.2**.

Adsorption-Desorption Measurements

Acetaldehyde adsorption capacity was evaluated at 1300 ppmv and 298 K. 20±0.1 mg of original, oxidized and metal oxide deposited ACF-2 were used for acetaldehyde adsorption. In the experiment using a mixture of CO_2 and acetaldehyde, pure CO_2 (99.999 % Carbagas)

was added to the acetaldehyde/He mixture via a second gas line. The concentration of CO_2 in the gas mixture was adjusted by modifying its flow rate. The experimental setup used for adsorption experiments was presented in **Section 3.4.1** and the calculation details in **Section 3.4.2**.

The temperature-programmed desorption (TPD) experiments were carried out as described in **Section 3.4.4**. A He flow of 50 cm^3 min^{-1} was applied at different temperature ramps (3-30 K min^{-1}). Mass 29 and 44 were monitored by the mass spectrometer for acetaldehyde. The concentration of CO_2 (mass 44 only) was also monitored.

7.3   Results and Discussion

7.3.1   Characterization of ACFs

Morphology

The morphology of the original ACFs materials consisting of elementary filaments of ~10 μm diameter was presented in **Figure 4.1**. Their morphology was conserved upon nitric acid treatment and metal oxide deposition.

The recorded N_2 adsorption isotherms of the original and MgO modified ACFs are shown in **Figure 7.1**. The isotherms of MgO modified ACFs correspond to the type I (according to the IUPAC classification) typical for microporous materials (d_p < 2 nm) suggesting that the ACFs morphology is kept upon MgO deposition. However the total pore volume is diminished by the NPs deposition.
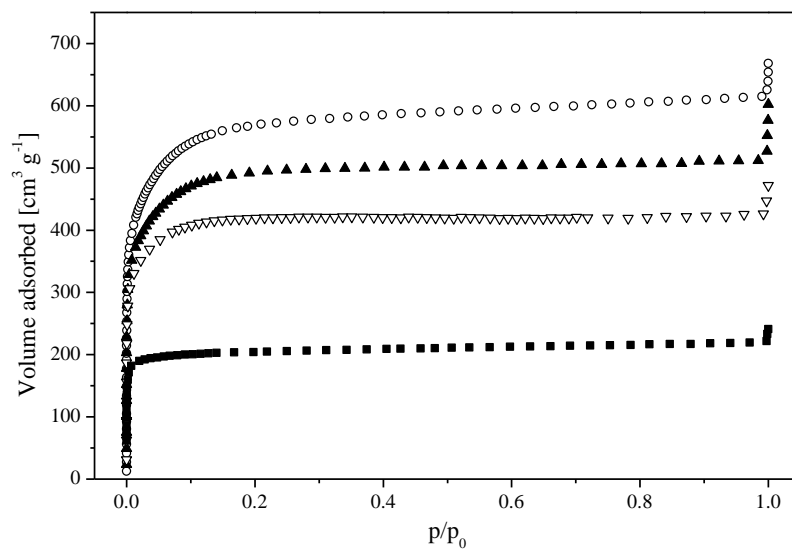
Figure 7.1 N_2 adsorption isotherms (77 K) for ACF-1 (■), ACF-2 (○), ACF-2/5%MgO (▲) and ACF-2/10%MgO (▽)

In order to evaluate the morphology of ACF-2 and MgO modified ACFs a pore size determination was carried out via comparative α-method [71]. Similar methodology was presented in **Chapter 4**, **5** and **6**.
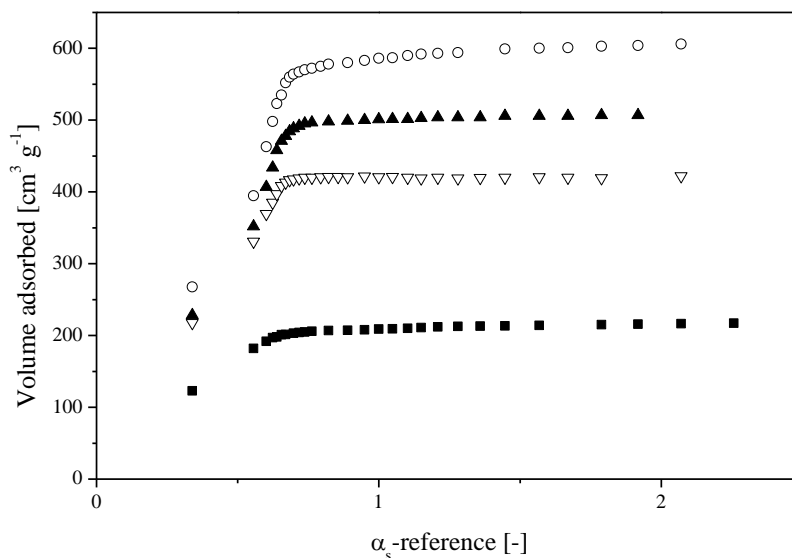
Figure 7.2 α-plot of ACF-1 (■), ACF-2 (○), ACF-2/5%MgO (▲) and ACF-2/10%MgO (▽)

The α-plots obtained for ACF-1 and ACF-2 and MgO modified ACF-2 are presented in **Figure 7.2**. Similarly to the data presented in **Chapter 4** for ACF-1 and ACF-2, the α-plots are linear and constant at α > 1 signifying a small external surface as compared to the surface in the pores [58]. The α-plots of MgO deposited ACF-2 is compared to original ACF-1 and ACF-2. As can be seen in **Figure 7.2** the curve slope change of ACF-2/5%MgO and ACF-2/10%MgO occurs between original ACF-1 and ACF-2. The mean pore size of metal oxide deposited ACF-2 is then suggested to slightly decrease upon MgO deposition. Since ACF-2 is supermicroporous (d_p 1-2 nm) and ACF-1 is ultramicroporous (d_p < 1 nm) (**Chapter 4**), it is suggested that the MgO NPs of deposited on ACF-2 are smaller than 2 nm and are located in the micropores.

The specific surface area of all samples was calculated through the BET equation using N_2 adsorption data [55]. The equation was linearized in the partial pressure range of 0.01-0.1 for ACF-2, ACF-2/5%MgO and ACF-2/10%MgO. As shown in **Table 7.1**, in all cases the *C* values obtained are > 100. The *C* value of the BET equation which can qualitatively describe

the pore size is increasing for MgO ACF-2/5%MgO and ACF-2/10%MgO suggesting a decrease of the micropore size confirming the interpretation of the α-plot. Therefore MgO deposition on ACF-2 was found to reduce the specific surface area, pore volume and the micropore size.

Table 7.1 Characteristics of ACFs adsorbents

Sample	SSA$_{BET}$ [m^2 g^{-1}]	C	Micropore volume [cm^3 g^{-1}]
ACF-1	800±50	6400	0.34±0.02
ACF-2	2170±50	280	0.94±0.02
ACF-2/5%MgO	1850±50	480	0.78±0.02
ACF-2/10%MgO	1590±50	1115	0.66±0.02

A high resolution scanning transmission electron microscopy (HRSTEM) analysis (EDX mode) of ACF-2/5%MgO revealed a homogenous distribution of MgO through the carbon fibers. However, a detailed study of individual MgO NPs was not possible even at the highest resolution due to a low contrast between carbon and magnesium. To overcome this problem, a HRSTEM study of ACF-2/5%La$_2$O$_3$ was carried out. Lanthanum (mass 237) provides a higher HRSTEM contrast. The obtained image is shown in **Figure 7.3** where homogenously distributed La$_2$O$_3$ nanoparticles with a size of 0.9-2 nm are clearly visible. The result confirms that metal oxide nanoparticles are formed within ACFs micropores and their size is controlled by the pore diameter. This conclusion holds for ACF-2/5%MgO since the nanoparticle formation was the same for all synthesized adsorbents. Nano-sized metal oxides are characterized by a very high surface-to-volume ratio and provide a large amount of active adsorption sites.
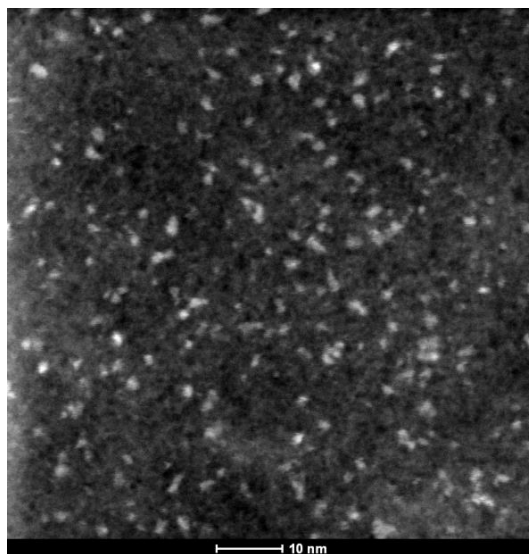
Figure 7.3 HRSTEM picture of ACF-2/5%La$_2$O$_3$

Precursor decomposition temperature

As mentioned in the experimental part (**Section 3.1.2**) to obtain metal oxide NPs, ACF-2 is impregnated by nitrate precursors (except TiO$_2$) and further decomposed by thermal treatment. The precursor decomposition temperature was studied by mass spectrometry. An example of alkaline-earth oxide decomposition on ACF-2 is shown in **Figure 7.4**.
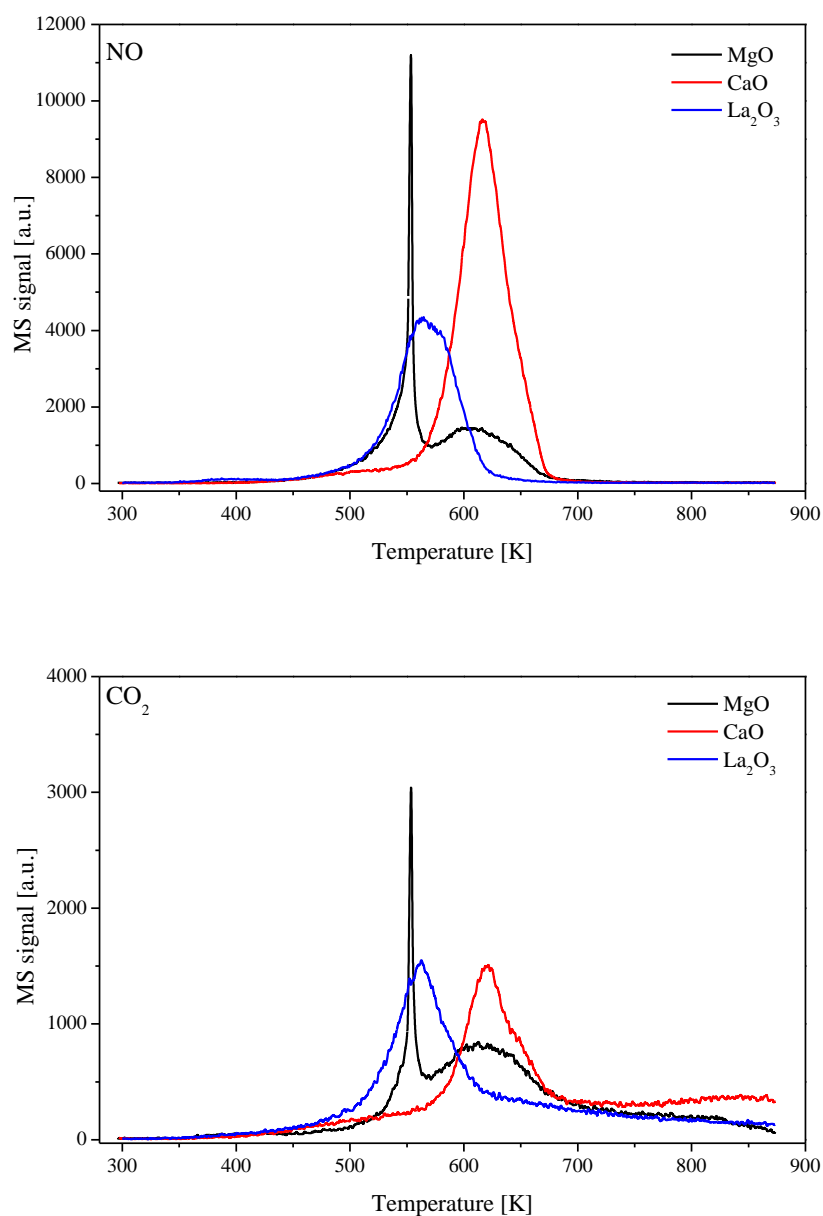
Figure 7.4 TPD profile of $Mg(NO_3)_2$, $Ca(NO_3)_2$ and $La(NO_3)_3$ on ACF-2 (10 K min^{-1} 50 cm^3 min^{-1})

As can be seen the decomposition of the all the alkaline-earth oxide precursors take place between 473 and 673 K. Nitrous oxide and carbon dioxide were the main species detected from the nitrates decomposition. Nitrous oxide comes from the nitrate group directly whereas the presence of carbon dioxide implies a partial oxidation of the ACFs during the

preparation. Whereas the NO signal reached its initial baseline before 673 K for all the samples, the CO_2 signal remains slightly higher probably due to desorption of O-containing group from the surface or formation of the alkaline-earth oxide NPs. The adsorbent were then prepared at 773 K. A further optimization of the ACF-2/5%MgO allowed decreasing the calcination temperature at 673K.

7.3.2 Acetaldehyde Adsorption

Acetaldehyde adsorption (1300 ppmv) on original, HNO_3 and MgO NPs treated ACF-2 is shown in **Figure 7.5**. The adsorption capacity was assessed by numerical integration of the area defined by the acetaldehyde breakthrough curve following the procedure detailed in **Section 3.4.3**.
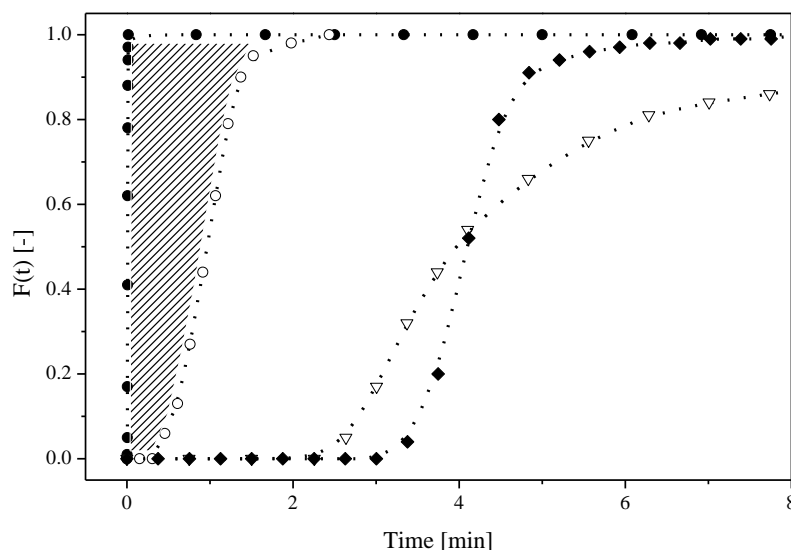
Figure 7.5 Acetaldehyde (1300 ppmv) breakthrough curves for ACF-2 (○), ACF-2/HNO_3-75m (♦), ACF-2/5%MgO (▽) and 2% (v/v) Argon (●). Total flow rate (STP) 200 cm^3 min^{-1} (298 K)

Similarly to more dilute mixture (**Chapter 5**), the acetaldehyde signal is equal to zero during a certain time and the breakthrough curve is relatively steep for original an HNO_3 modified ACF-2 implying fast kinetics of acetaldehyde adsorption on ACFs. The adsorption capacity calculated for the original and HNO_3 modified ACF-2 were 3.2 and 9.9 wt.%, respectively. Due to the higher partial pressure of acetaldehyde (1300 vs 80 ppmv) these adsorption capacities are considerably larger as compared to the values reported in **Chapter 5**.

As showed in **Figure 7.5**, the deposition of MgO NPs on original ACF-2 increases the acetaldehyde adsorption capacity. Although a total acetaldehyde removal is also observed the breakthrough curve is less steep suggesting pronounced mass transfer limitations. As compared to HNO_3 treated ACF-2 the acetaldehyde concentration raised earlier but since its slope is less steep the total adsorption is larger (16 wt. %). Hence the deposition of MgO on ACF-2 is a more performant strategy for acetaldehyde removal as compared to HNO_3 treatment. Moreover ACF-2/5%MgO is supposed to be a more selective adsorbent as compared to the O-functional groups obtained by HNO_3 treatment.

The deposition of other alkaline-earth oxide such as CaO and La_2O_3 on ACF-2 was carried out. The acetaldehyde breakthrough curves are presented in **Figure 7.6**.
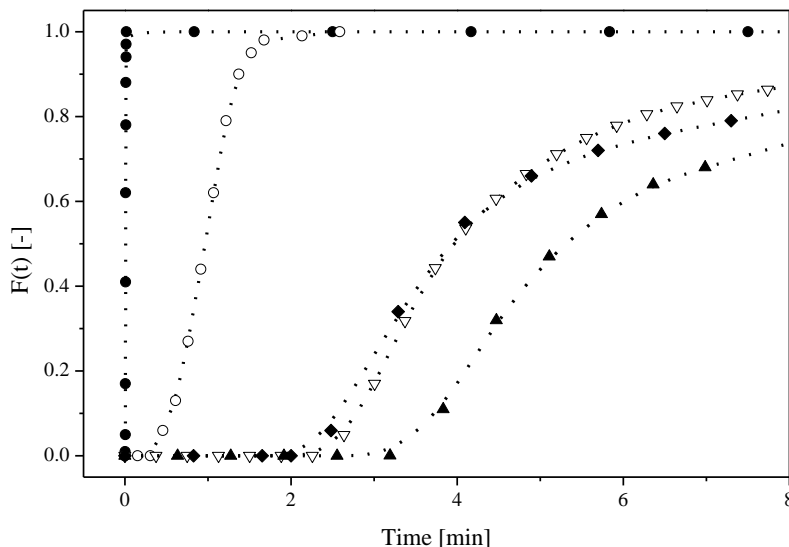
Figure 7.6 Acetaldehyde (1300 ppmv) breakthrough curves for ACF-2 (○), ACF-2/5%MgO (▽), ACF-2/5%CaO (♦), ACF-2/5%La$_2$O$_3$ (▲) and 2% (v/v) Argon (●). Total flow rate (STP) 200 cm^3 min^{-1} (298 K)

The breakthrough curve of CaO and La$_2$O$_3$ on ACF-2 shows similar shape than ACF-2/5%MgO. They are also efficient adsorbent and present similar mass transfer limitations. Since the mean diameter of the pores is not drastically affected by the deposition of metal oxides, migration of adsorbed acetaldehyde on the metal oxide NPs are suggested to govern the adsorption rate.

The adsorption capacities of the different metal oxide deposited on ACF-2 are shown in **Figure 7.7**. As observed, the ACFs modified by alkaline-earth metal oxide are showing the largest acetaldehyde adsorption capacity. Alkaline-earth metal oxides are known for their basicity [234]. Both CO$_2$ chemisorption microcalorimetry and TPD experiments showed a stronger basic character of CaO as compared to MgO [235]. CO$_2$ adsorption experiments revealed a larger adsorption capacity of La$_2$O$_3$ as compared to CaO and MgO implying the stronger basic character of La$_2$O$_3$ [236]. The amphoteric properties of TiO$_2$, Al$_2$O$_3$ and ZnO

were confirmed by both CO_2 and NH_3 chemisorption microcalorimetry methods [236]. Thus, we can conclude that the acetaldehyde adsorption capacity of ACF modified by metal oxide NPs is related to the basicity of the latter. NPs with a higher basicity provide a larger acetaldehyde removal capacity.
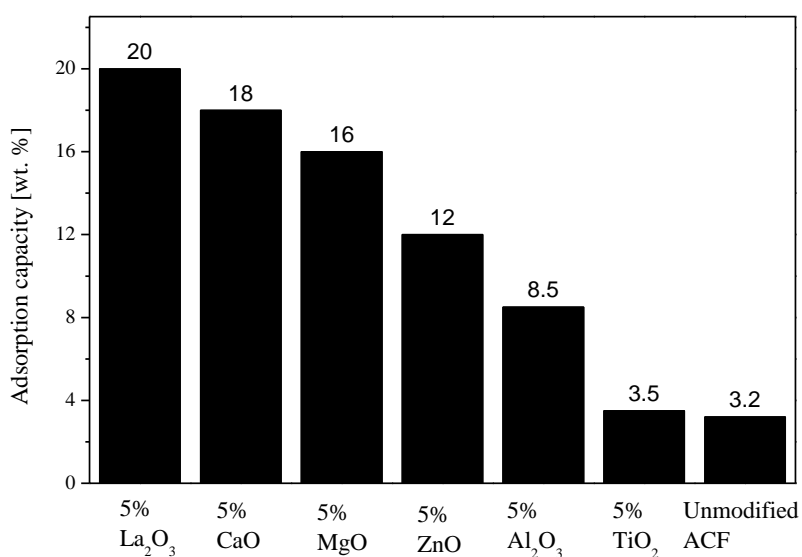
Figure 7.7 Acetaldehyde (1300 ppmv) adsorption capacity of metal oxide modified ACF-2

(298 K)

A higher acetaldehyde adsorption capacity by MgO and CaO aerogels as compared to activated carbon (measured by a static gravimetric method) has already been reported [156]. However, metal oxide NPs supported on ACF-2 in our samples are much smaller (0.9-2 nm) as compared to aerogel nano-powders (4-7 nm) [231] and provide a much higher amount of active sites for acetaldehyde adsorption for a similar metal oxide quantity. Moreover, the structured ACF material provides a low pressure drop being suitable for a dynamic adsorption from flue gas streams.

7.3.3   Competitive Adsorption: CO_2 Effect

In industrial flue gas streams, acetaldehyde is often mixed with other gases including CO_2. Therefore, competitive adsorption of CO_2 and acetaldehyde on basic metal oxide NPs supported on ACFs was studied taking ACF-2/5%MgO as a representative sample. The concentration of acetaldehyde in gaseous streams was fixed at 1300 ppmv whereas the concentration of CO_2 was varied.
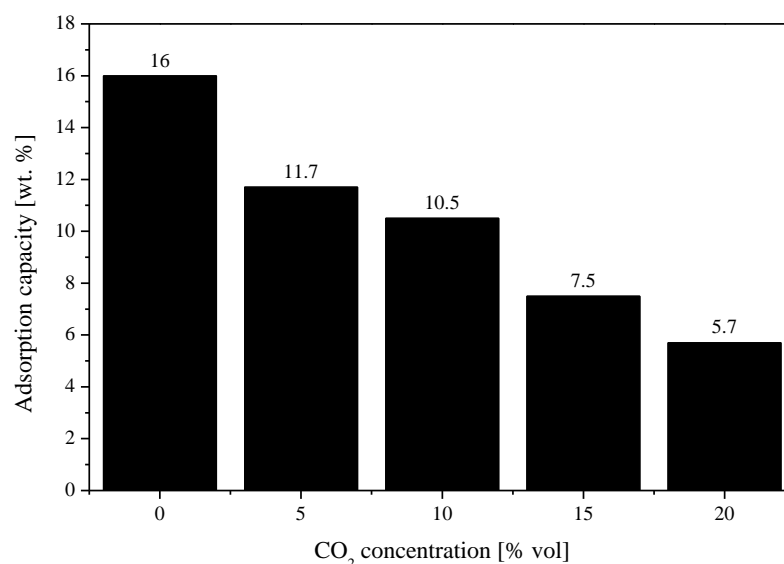
Figure 7.8 Acetaldehyde (1300 ppmv) adsorption capacity of ACF-2/5%MgO as a function of CO_2 concentration (298 K)

As shown in **Figure 7.8**, the presence of CO_2 in the stream decreases the adsorption capacity of ACF-2/5%MgO towards acetaldehyde. A competitive adsorption of acetaldehyde and CO_2 on MgO sites can be supposed since CO_2 is known for its interactions with basic surface [237]. Despite the decrease of the adsorption capacity in presence of CO_2, the selectivity of ACF-2/5%MgO is still very high. A 100 fold larger CO_2 concentration (10 %

(v/v)) divides by 2 the adsorption capacity towards acetaldehyde. However, in presence of CO_2 the acetaldehyde outlet concentration never dropped to zero meaning that the complete acetaldehyde removal was not achieved. The minimum acetaldehyde concentration reached at the outlet was ~80 ppmv and corresponds to a 90-95 % of acetaldehyde removal.

Using ACF-1/5%MgO instead of ACF-2/5%MgO, decreased drastically the effect of CO_2 (**Figure 7.9**). In the presence of CO_2 the adsorption capacity of ACF-2/5%MgO decreased from 16 to 9.5 wt. %, while a little or no change was observed for ACF-1/5%MgO. As shown in **Chapter 4**, ACF-1 has smaller micropores as compared to ACF-2 decreasing the MgO NPs size. However, the adsorption capacity of ACF-1/5%MgO was ~1.6 times smaller as compared to ACF-2/5%MgO. This result can be explained by a partial blockage of MgO NPs within the narrower pores of ACF-1. At the same time such geometry results in an improved selectivity of adsorption towards acetaldehyde in the presence of CO_2.
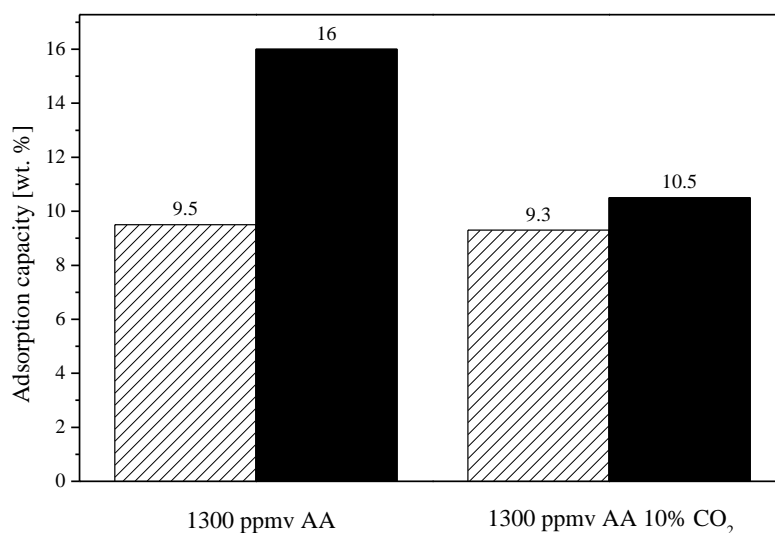
Figure 7.9 Acetaldehyde (1300 ppmv) adsorption capacity of ACF-1/5%MgO (hatched bars) and ACF-2/5%MgO (solid bars) in the presence of 10% CO_2 (298 K)

7.3.4   Temperature-Programmed Desorption of Acetaldehyde

The interactions between acetaldehyde and the adsorbent surface were characterized by TPD of adsorbed acetaldehyde. The acetaldehyde TPD profiles recorded for ACF-2/5% MgO are shown in **Figure 7.10**. The profile recorded for ACF-2/HNO$_3$-75m is also shown for comparison.
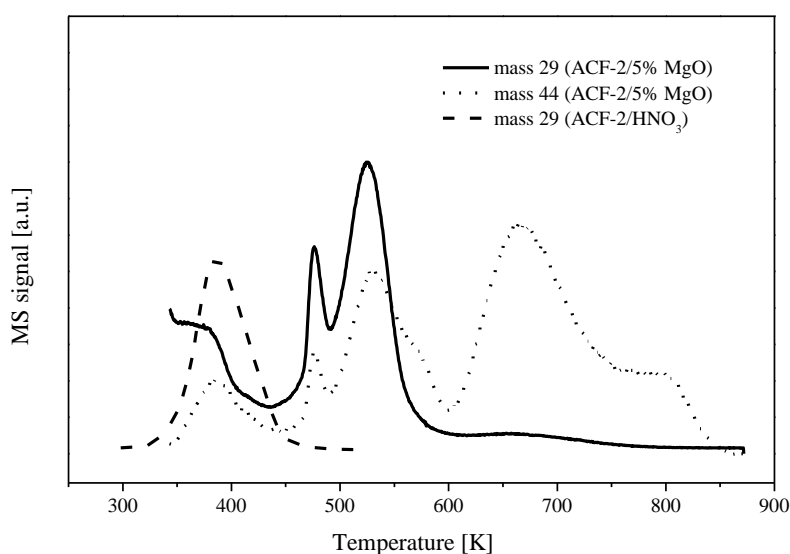
Figure 7.10 TPD profile of acetaldehyde desorption over ACF-2/5%MgO and ACF-2/HNO$_3$-75m (10 K min^{-1}, 100 cm^3 min^{-1})

The experiments were carried out by monitoring mass 29 and 44 at the reactor outlet. Mass 44 corresponds to the molecular ion of acetaldehyde whereas mass 29 is the main fragment. This is important to underline because mass 44 is also the characteristic mass of CO$_2$. Several TPD peaks observed in **Figure 7.10** imply that ACF-2/5%MgO has energetically different adsorption sites. The first desorption peak corresponds to the weakest adsorption sites. The curve of both masses 44 and 29 are detected here simultaneously

signifying that acetaldehyde molecules are desorbed in this case. The same peak appears in acetaldehyde TPD from ACF-2/HNO_3-75m. Since ACF-2/HNO_3-75m has only O-containing surface groups to adsorb acetaldehyde, it is suggested that the first peak corresponds to acetaldehyde molecules adsorbed on O-containing carbon surface groups of ACF-2/5%MgO [106, 129]. The larger area under the peak of ACF-2/HNO_3 as compared to ACF-2/5%MgO is explained by the extremely low content of surface oxygen groups on ACF-2/5%MgO. Indeed, ACF-2 has a low initial content of O-containing groups and in the case of ACF-2/5%MgO the fibers went through a calcination process, which partially removed the O-containing groups.

The two next peaks appearing at higher temperatures (~470 and 520 K) are attributed to acetaldehyde adsorbed on MgO NPs. The hypothesis of multiple MgO adsorption sites has been discussed in several papers dealing with acetaldehyde adsorption on nanocrystalline aerogel prepared MgO [156, 238]. The density functional study of acetaldehyde adsorption on nano-sized MgO revealed different adsorption sites on the surface. Two modes of acetaldehyde adsorption were identified. In one of them, the acetaldehyde carbonyl group is aligned perpendicularly to the MgO surface and attached to a Mg^{2+} ion through the oxygen atom without involving the carbon atom. One hydrogen of the methyl group can interact with a surface O^{2-} ion (**Figure 7.11 A**). In other adsorption mode, the carbonyl group is oriented horizontally to the MgO surface above a Mg-O bond. In this case, the carbonyl group interacts with a MgO NP through both oxygen and carbon atoms (**Figure 7.11 B**).
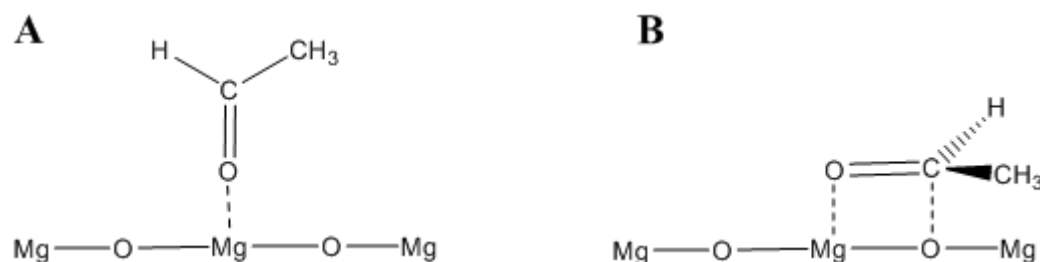
Figure 7.11 Mode of acetaldehyde adsorption on MgO NPs

The 4th TPD peak (~670 K) in **Figure 7.10** is represented only by mass 44. It was therefore attributed to CO_2 desorption. CO_2 is either adsorbed by MgO NPs from ambient air during the storage or created by destructive desorption of acetaldehyde and/or products of its chemical transformation on MgO NPs. Alkaline earth metal oxides are well known acid-base catalysts for various reactions [239, 240], such as aldol addition and condensation [241, 242] or Tishchenko reaction [243, 244]. Although, none of the products of these reactions were detected in the adsorbent downstream, they could be strongly adsorbed on the ACF-2/5%MgO surface and decomposed at elevated temperature to form CO_2.

Acetaldehyde desorption from ACF-2/5%MgO was also studied using different temperature ramps. In this case, the peaks maxima are shifted depending on the temperature ramp. The measurements allow to calculate the activation energy of desorption (E_d) by measuring the desorption rate at different temperatures [213]. In TPD experiments, temperature is increased linearly and desorption rate changes. The activation energy of desorption is determined by varying the temperature ramp and measuring the temperature at the maximum desorption rate. Since the difference between activation energy and heat of desorption is negligible [213], the activation energy of desorption can be approximated as the adsorption enthalpy *(ΔH_{ads})*. The adsorption enthalpy of acetaldehyde on different active sites of ACF-2/5%MgO is presented in **Table 7.2**.

Table 7.2 Heat of acetaldehyde adsorption on different active sites of ACF-2/5%MgO (10 K min^{-1}, 100 cm^3 min^{-1})

Type of active sites	Peak position (at 10 K min^{-1}) [K]	ΔH^0_{ads} [kJ mol^{-1}]
1	390	-22±10
2	470	-45±13
3	520	-77±11

The adsorption enthalpy calculated for the 1st peak is a relatively low (-22 kJ·mol^{-1}). It corresponds to physisorption of acetaldehyde molecules on O-containing carbon surface groups via hydrogen bonding as already reported by several research groups [106, 129]. The obtained *ΔH$_{ads}$* value is in line with the published ones. The isosteric heat of acetaldehyde adsorption determined at zero surface coverage for graphitized carbon black and HNO$_3$ treated activated carbon was reported to be -25.8 and -32.4 kJ mol^{-1}, respectively [129].

Acetaldehyde adsorption on other active sites (2nd and 3rd TPD peaks) is characterized by larger adsorption enthalpy values: -45 and -76 kJ mol^{-1}, respectively, and corresponds to its chemisorption on MgO NPs. The obtained *ΔH$_{ads}$* values are comparable to the published results calculated by DFT for acetaldehyde adsorption on a nano-sized MgO powder: -44 and -73 kJ mol^{-1} [238]. The DFT calculations allowed describing the acetaldehyde adsorption conformations on the MgO surface. Acetaldehyde molecules desorbing from the 2nd type of active sites (desorption temperature ~470 K, **Table 7.2**) were adsorbed through the carbonyl group oriented horizontally above Mg^{2+}-O^{2-} ion pair (**Figure 7.11 B**). Both carbon and oxygen atoms of the carbonyl group are involved in this interaction. Acetaldehyde adsorption on the 3rd type site (desorption temperature ~520 K, **Table 7.2**) takes place solely through the oxygen atom of the acetaldehyde group attached to Mg^{2+} ion (**Figure 7.11 A**).

7.4 Conclusions

In summary, structured adsorbents efficient for acetaldehyde removal from diluted gas streams have been developed. ACFs have been used as structured supports for nanoparticles (NPs) of basic metal oxides. Deposited NPs were stabilized within the ACFs micropores and have mean diameter below 2 nm. The highest adsorption capacity up to 20 wt.% of acetaldehyde was obtained with the NPs of the most basic metal oxides, La_2O_3 and MgO.

The developed adsorbents based on modified ACF are sensitive to the presence of CO_2 in the gas stream due to its competitive adsorption with acetaldehyde on metal oxide NPs. The adsorption selectivity towards acetaldehyde could be increased by using ACF with narrower microporosity (ACF-1). Smaller MgO NPs more selective towards acetaldehyde are suggested to be created by the narrower microporosity.

Acetaldehyde TPD from ACF-2/5%MgO revealed three types of surface adsorption sites: one was assigned to physisorption on the surface O-containing carbon groups and two other sites are on MgO surface and provide acetaldehyde chemisorption in two different modes.

7.5 Practical Applications of Metal Oxide Functionalized ACFs for Cigarette Smoke Constituents Removal

Although not mentioned earlier in this thesis, the adsorbents presented in this thesis were developed for the particular application of cigarette smoke constituents removal. The targeted VOC chosen along this thesis were also selected based on the smoke composition. For the acetaldehyde removal, metal oxide NPs deposited on ACFs showed the largest adsorption capacity. The acetaldehyde amount adsorbed was larger than to the quantities of acetaldehyde present in cigarette smoke. Moreover ACF-2/5%MgO was shown to be stable in

time and efficient in the presence of 10 % (v/v) CO_2 in the gas mixture (**Figure 7.8**). Hence this adsorbent was tested in cigarette conditions.

Figure 7.12 presents the design of the cigarette filter prototypes. The filter is divided in 3 different compartments. The first one starting from the mouth end is 18 mm long and is composed of cellulose acetate, the standard component of cigarette filters. The second compartment is constituted of five disks of ACF-2/5%MgO for a total length of 3 mm. The weight of adsorbent is 30 mg. The third part of the filter with a length of 6 mm is composed of cellulose acetate.
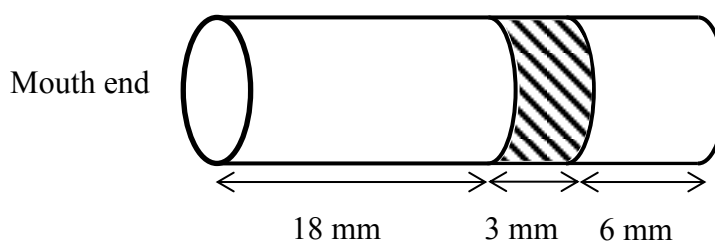
Figure 7.12 Cigarette filter design

The experiments were carried out in a smoke machine with 20 cigarettes constituted with ACF-2/5%MgO filters. The performance of the adsorbent was evaluated by measuring the composition of the smoke after the mouth end. The performance of the developed adsorbents was evaluated for 5 different compounds: acetaldehyde, acrolein, formaldehyde, benzene and butadiene. The performances of the filters towards acetaldehyde are reported in **Figure 7.13**.
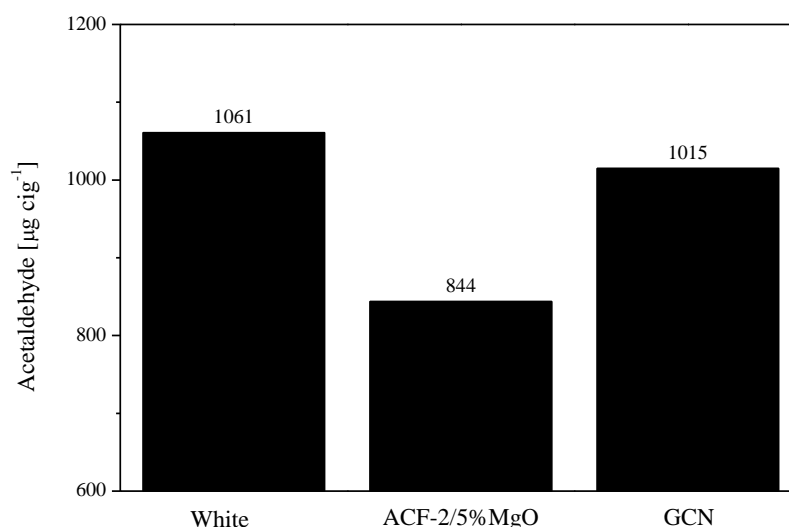
Figure 7.13 Non-retained acetaldehyde quantities in cigarettes conditions

As can be seen ACF-2/5%MgO is an efficient adsorbent for acetaldehyde in real smoke conditions. The non-retained acetaldehyde content in a cellulose acetate filter is about 1.06 mg whereas it decreases to 0.84 mg with ACF-2/5%MgO. A third type of filter is tested for comparison (GCN) which consists of 60 mg of granulated activated carbon disposed in the filter. The granulated activated carbon particles have a diameter of 500 μm. They are microporous adsorbents similarly to ACFs. However they are not functionalized with MgO NPs. As can be seen their performance, is lower as compared to ACF-2/5%MgO since 1.02 mg of acetaldehyde are not retained by the filter. Hence the combination of ACFs and MgO NPs provides a considerable increase of the removal of smoke compounds.

The performance of ACF-2/5%MgO was also evaluated for the other aldehyde such as formaldehyde and acrolein. The results are presented in **Figure 7.14**.
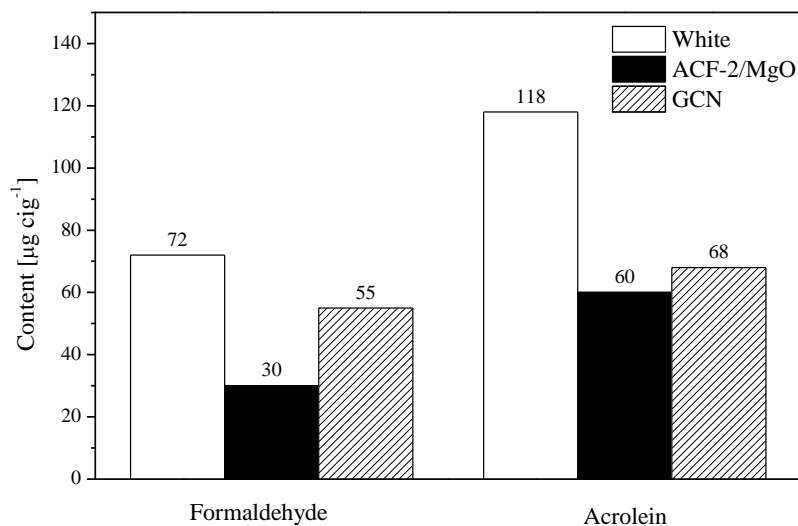
Figure 7.14 Non-retained formaldehyde and acrolein quantities in cigarette conditions

The results clearly indicate that the filters composed with ACF-2/5%MgO are more efficient than standard cellulose acetate or granulated activated carbon for aldehydes. A removal larger than 50% is achieved by the ACF-2/5%MgO. Such performance is attributed to the combination of basic metal oxide NPs due to their high adsorption potential towards aldehydes and the favorable open macrostructure of the ACFs.

Finally the performance of ACF-2/5%MgO was evaluated for non-polar compounds such as benzene and butadiene. For such compounds the functionalization of ACF-2 by MgO NPs is not supposed to enhance the adsorption capacity. However a large adsorption capacity towards toluene attributed to the well-developed microporosity of the ACF-2 was reported in **Chapter 4**. Due to the molecular similarities between toluene and benzene, high adsorption capacity of ACF-2 is expected for benzene. Although the microporosity of ACF-2 is slightly decreased by the MgO NPs deposition it is supposed to be sufficient for efficient benzene removal from cigarette smoke. The performance of the different filters towards benzene and butadiene are presented in **Figure 7.15**.
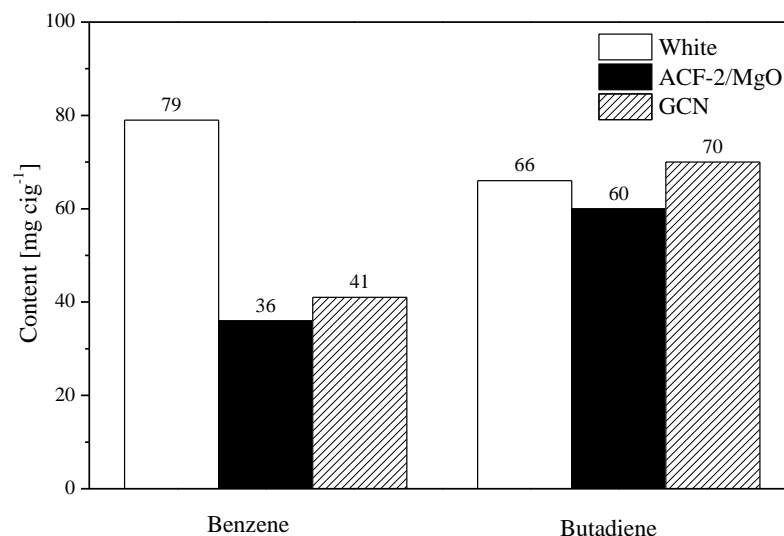
Figure 7.15 Non-retained benzene and butadiene quantities in cigarette conditions

The efficiency of the cigarette filter composed of ACF-2/5%MgO towards benzene is clearly shown. More than 50% of the benzene is retained by the filter containing ACF-2/5%MgO. As suggested earlier the large efficiency towards benzene is attributed to the microporosity of ACF-2 and not to the MgO NPs. For benzene, the efficiency of granulated activated carbon is in the same range compared to ACFs due to their similar microporosity.

Despite its non-polar properties similar to toluene, butadiene is efficiently retained neither by ACF-2/5%MgO nor by granulated activated carbon. This phenomenon is attributed to the high volatility of this VOC (boiling point 269 K) and the lack of specific interaction sites.

In conclusions, an efficient adsorption of aldehydes (acetaldehyde, formaldehyde and acrolein) by cigarette filters composed of ACF-2/5%MgO is observed in real conditions despite the complexity of the smoke constitution. A 20% removal is measured towards

acetaldehyde whereas a 50% removal has been measured for acrolein and formaldehyde. The performances of ACF-2/5%MgO are significantly better than granulated activated carbon. The efficiency of this adsorbent in cigarette conditions towards benzene was also shown. Only butadiene is not efficiently retained because of its high volatility and the absence of interactions with MgO NPs. Hence another strategy is necessary for the development of an efficient adsorbent.

8 Butadiene Adsorption by Zeolites

This chapter reports the adsorption of diluted butadiene (100 ppmv) over original and modified Na-X. The modification of this zeolite was performed via water treatment followed by calcination. The bulk composition and surface chemistry of the original and modified zeolites were characterized. Adsorption of butadiene over modified zeolites was studied by *in situ* FTIR to get an insight of the adsorption mechanism. The thermodynamic parameters were obtained through the modelling of butadiene adsorption isotherms. Temperature-programmed desorption was carried out and simulated. Finally the thermodynamic parameters obtained by TPD and isotherm methods were compared.

8.1 Introduction

As described in **Chapter 4**, ACFs are very efficient for the removal of non-polar high boiling point VOC such as toluene thanks to pore condensation mechanisms, whereas, for non-polar low boiling point VOC, their adsorption capacity is considerably smaller, particularly for diluted mixtures [221]. Identically to polar VOC removal (**Chapter 6** and **7**), the creation of specific adsorption sites can represent a valuable alternative for efficient adsorption of non-polar low boiling point VOC.

As presented in **Chapter 2**, besides activated carbon, zeolite is another widely used adsorbent. Consisting of crystalline microporous aluminosilicates with an infinite three dimensional framework of AlO_4 and SiO_4, zeolites are characterized by an important micropore volume and a large specific surface area [245]. Because of their particular structure, they can present surface acid sites often used in catalytic reactions [246, 247]. In the context of adsorption, these acid sites can serve for specific adsorption. Two types of acidity are usually reported for zeolites: Brønsted and Lewis sites [248]. Brønsted acid sites are formed by aluminum atoms connected to silicon by a "bridging hydroxyl" (Si-OH-Al) where the framework negative charge is compensated by a proton. Lewis acid sites are composed of aluminum or silicon with low coordination [249] or of alkaline cations such as sodium [250]. Recently Brønsted sites were reported to interact with the π bond of olefins in H-ZSM-5 [251].

Butadiene is a non-polar low boiling point (269 K) VOC. Because of its physical properties efficient butadiene adsorption is particularly challenging. Indeed the adsorption capacities of microporous ACFs reported for similar compounds (butane) are relatively low [104]. Hence, efficient adsorption requires specific chemical interactions. Some publications report the use of transition metal-exchanged zeolites [181, 182] or polycations metal

exchanged zeolites [184] for butadiene adsorption involving a π-complexation mechanism. Interactions between the *d* orbital of the transition metal and the electron rich π system of butadiene are suggested [158]. Although exchanged zeolites are efficient adsorbents, the adsorption mechanism is still unclear. Moreover, since a large number of transition metals are interacting with butadiene, there are still doubts regarding the activity of the exchanged metal cations [182].

This chapter reports a novel efficient adsorbent for butadiene removal at low partial pressure. An approach for studying the type of zeolite acidity and the butadiene adsorption capacity is chosen. Butadiene adsorption isotherms have been measured and temperature programmed desorption measurements were performed to get insights of the adsorption enthalpy. Adsorption mechanism and characterization of surface sites is assessed by FT-IR spectroscopy, pyridine TPD and ^{27}Al MAS NMR.

8.2 Experimental

Materials

The zeolite samples are described in **Section 3.1.3**. Prior to adsorption measurement the zeolites were heated at 373 K (He 40 cm^3 min^{-1}) during 30 minutes.

The butadiene/He 0.1 % (v/v) was purchased by Carbagas and was diluted 10 times to obtained an outlet concentration of 100 ppmv in the setup described in **Section 3.4.1**.

Adsorbents Characterization

The zeolite morphology was characterized by N$_2$ adsorption at 77 K and scanning electron microscopy. The bulk composition of the zeolites was assessed by elemental analysis via AAS method and MAS NMR whereas the crystallography of the zeolites was measured

by XRD. The analysis of the zeolite surface was obtained by IR spectroscopy. The acidity of the adsorbent was evaluated by *in situ* FTIR with pyridine as a probe molecule for qualitative evaluation and by pyridine TPD using a Micromeritics Autochem II for acid site quantification. Detailed description of the apparatus used and the conditions applied can be found in **Section 3.2**.

Adsorption-Desorption Measurements

Butadiene adsorption isotherms on the Na-X and Na-X-H_2O (40 mg $\pm$ 0.5) were obtained by measuring the adsorption capacity at different temperatures (298-333 K) and butadiene partial pressures (25-300 ppmv). The experimental setup used for adsorption experiments was presented in **Section 3.4.1** and the calculation details in **Section 3.4.2**.

The temperature-programmed desorption experiments were carried out as described in **Section 3.4.4**.

8.3   Results and Discussion

8.3.1   Characterization of Zeolites

Morphology

A representative SEM image of the original Na-X is shown in **Figure 8.1**. As can be seen on the right picture the pellet size is around 500 µm. Such pellet size was chosen to avoid pressure drop encountered with small particles and mass transfer limitations appearing with large particles. The pellets are constituted of elementary microcrystals of around 4-5 µm linked together (right picture) without possessing a proper 3-dimensional shape. The general appearance of the zeolite was maintained after water treatment.
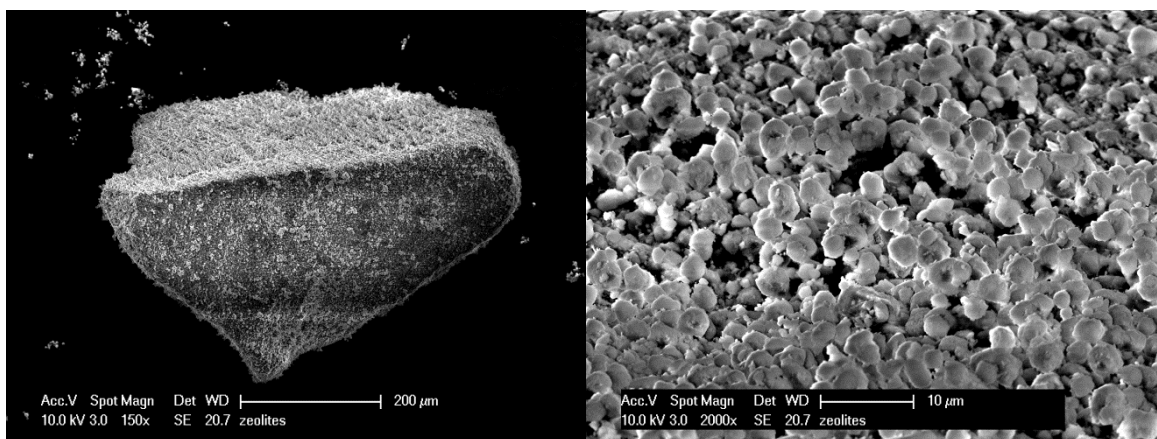
Figure 8.1 SEM picture of zeolite

The N_2 adsorption isotherm of the original Na-X and water treated Na-X are presented in **Figure 8.2**. The two isotherms are similar implying that the water treatment does not affect the porosity of the zeolite. They correspond to a type I isotherm according to the IUPAC classification indicating a microporous material (pore diameter < 2 nm) [12]. The specific surface area of the adsorbents was calculated from N_2 adsorption data using the BET equation [55]. The BET equation was linearized in the 0.001-0.05 pressure range. The specific surface area was found to be 750 m^2 g^{-1} and the pore volume was measured around 0.28 cm^3 g^{-1} which is in the same range as already published values [252]. The "*C*" value of the BET equation is a qualitative representation of the first layer adsorption energy. Such high value (~50000) indicates microporous structure with narrow pore size corresponding to the theoretical faujasite channel size of 7.4 Å [245].
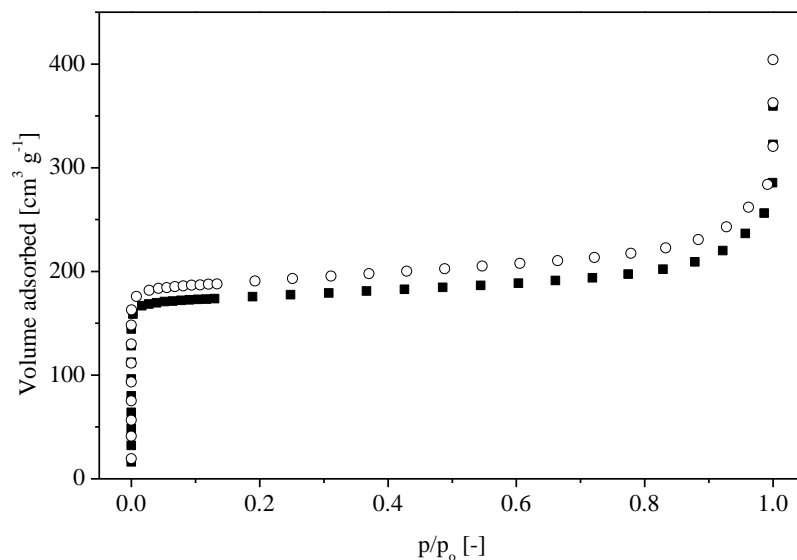
Figure 8.2 N_2 adsorption isotherm (77 K) of Na-X (○) and Na-X-H_2O (■)

The increase in N_2 adsorption capacity at $p/p_0 > 0.8$ suggests adsorption on external surface of the zeolite. Due to the small size of the zeolite crystals presented in **Figure 8.1** their external surface is large enough to influence the N_2 isotherm. Since in this study butadiene removal is studied at low partial pressure (300 ppmv), it should not be influenced by the zeolite external surface.

Bulk Composition

The structure of the adsorbent was studied by X-ray diffraction and solid state NMR whereas its chemical composition was determined by atomic absorption spectroscopy (AAS). Since zeolites are crystalline aluminosilicates, strong XRD signal was expected for the original compound used as a blank. As shown in **Figure 8.3** the XRD pattern of Na-X corresponds to the faujasite reference. The XRD analysis of Na-X-H_2O also reveals a crystalline structure identified by sharp diffraction peaks. Moreover the position of the

diffraction peaks is identical to the faujasite pattern implying that the treatment with water does not affect the initial crystalline structure of the zeolite.
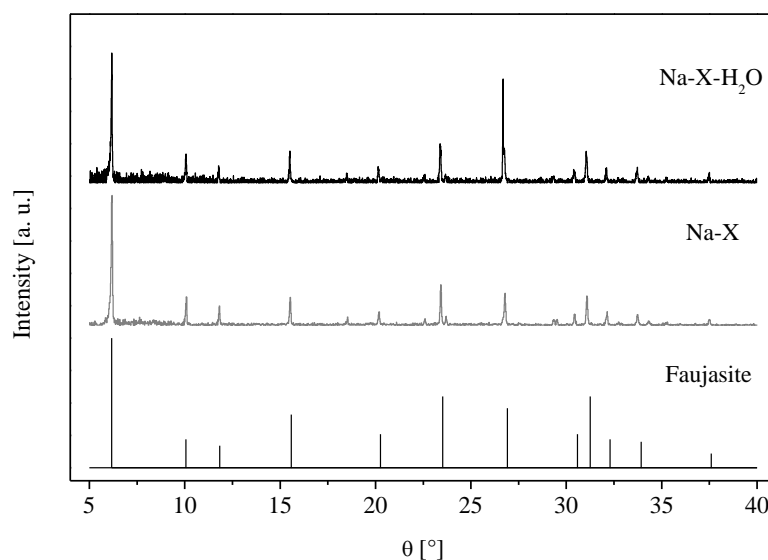
Figure 8.3 XRD pattern of original and modified zeolite

The result of the elemental analysis performed by AAS is shown in **Table 8.1**. The analysis of original Na-X shows a Si/Al ratio of 0.96, slightly lower than the composition announced by the provider (**Section 3.1.3**). The Na/Al ratio is 0.93 insuring that the majority of the framework counterions are sodium. The elemental composition of Na-X-H_2O showed a slightly increased Si/Al ratio signifying that partial zeolite dealumination occurred during the water treatment whereas the Na/Al (0.95) ratio was kept constant within experimental error.

Table 8.1 Elemental analysis of Na-X and Na-X-H_2O

Sample	Si/Al	Na/Al
Na-X	0.96±0.05	0.93±0.05
Na-X-H_2O	1.3±0.05	0.95±0.05

The bulk composition of Na-X and Na-X-H_2O was studied by solid state NMR. As can be seen in **Figure 8.4** both samples show a sharp band at 64 ppm in their ^{27}Al MAS NMR spectra, consistent with the presence of tetrahedral coordinated aluminum in the zeolite framework. No additional peak is observed for Na-X-H_2O. The slight shift between the two curves is attributed to experimental error and is not representative of a different type of Al atom environment.
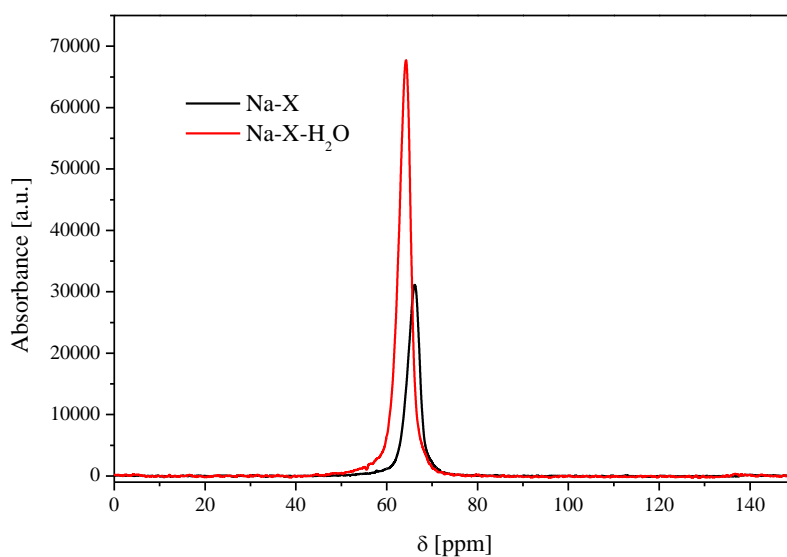
Figure 8.4 ^{27}Al MAS NMR spectra of Na-X and Na-X-H_2O

Surface Chemistry

The surface chemistry of the original and water treated zeolites were characterized by FTIR techniques. Since zeolite samples surface are generally covered by chemi and physi-sorbed water, they were treated at 573 K under N_2 flow in order to observe the hydroxyl surface groups. As shown in **Figure 8.5** Na-X displays three distinct bands in the OH region at 3637 (Si-OH-Al located in large cavity) [253], 3700-3680 (OH on extraframework/defect sites) [254, 255] and 3734 cm^{-1} (silanols) [256]. A wide contribution is observed between 3300 and 3500 cm^{-1}, attributed to bonded OH, partially located in small cavities. Na-X-H_2O presents mainly bands at 3637 and 3734 cm^{-1} whereas the band at 3680 cm^{-1} observed for Na-X has a much lower intensity.

Since the band at 3680 cm^{-1}, attributed to extraframework Al or defect sites, does not appear after the treatment, it is suggested that such treatment of Na-X leads to the removal of these Al sites. The increase of the Si/Al content reported in **Table 8.1** is in line with this assumption.
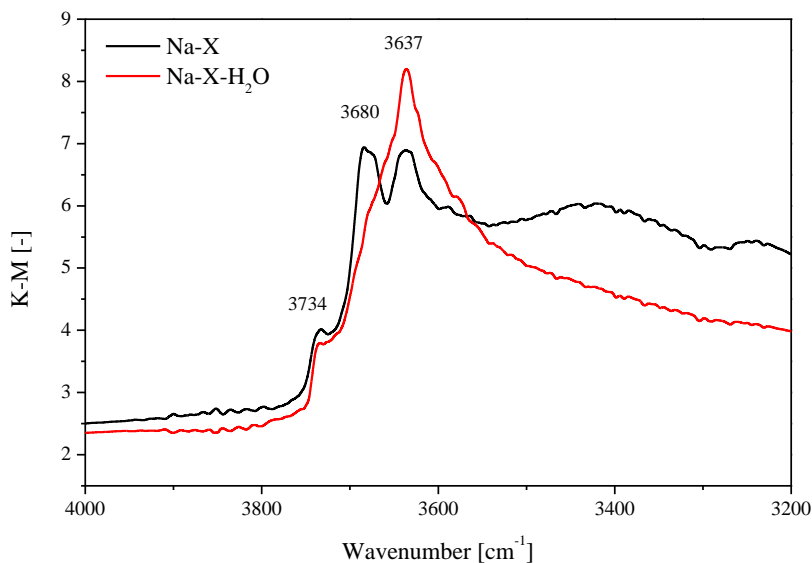
Figure 8.5 OH region of FTIR spectra for Na-X and Na-X-H$_2$O (573 K)

Qualitative analysis of the acid nature was performed by FTIR spectroscopy using pyridine as a probe adsorbed on the zeolite surface. Such technique is widely known for zeolite acid site characterization [234, 257]. The FTIR spectra of pyridine adsorption on both zeolites are shown in **Figure 8.6**. The bands at 1590, 1490 and 1443 cm^{-1} are attributed to Lewis acid sites whereas the peak at 1541 cm^{-1} is characteristic for Brønsted acid [258]. As can be seen, the pyridine adsorption peaks of Lewis acid sites are clearly visible for both zeolites. Na-X does not display an adsorption peak for Brønsted acid whereas a broad peak is present at 1541 cm^{-1} for Na-X-H$_2$O. The presence of Brønsted sites on Na-X-H$_2$O is explained by a partial exchange of the Na$^+$ cation with H$^+$ cations present in aqueous solution during the water treatment. However, their content remains relatively low compared to Lewis acid sites.
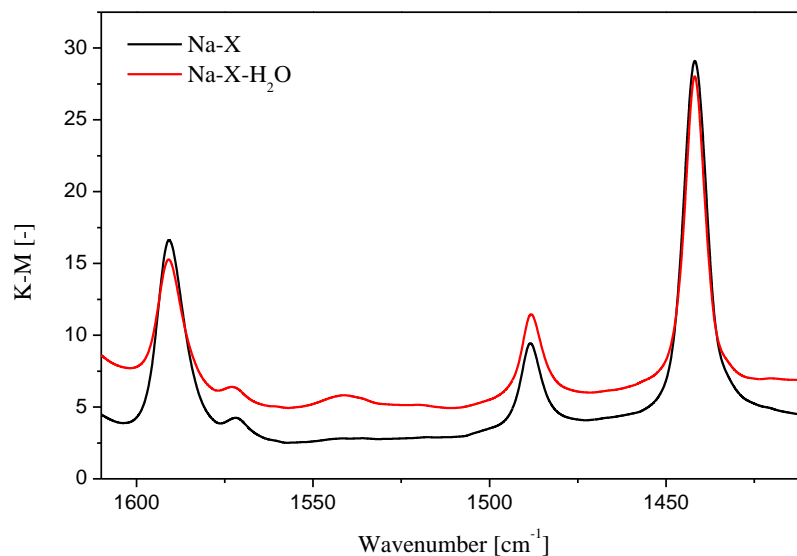
Figure 8.6 FTIR spectra of pyridine adsorption on Na-X and Na-X-H_2O

For quantitative analysis of the zeolite surface acidity, their surface was characterized by desorption of pyridine. Acid strengths were defined according to the pyridine desorption temperatures. For quantitative analysis the desorption peaks were integrated based on a TCD calibration. As shown in **Figure 8.7** Na-X shows two types of acid sites: weak ones, identified by a desorption peak at around 600 K and a strong one with a desorption peak at 740 K. As can be seen, the quantity of weak acid sites is lower as compared to strong ones.

The absence of desorption peak at 600 K in the pyridine desorption pattern of Na-X-H_2O clearly indicates a disappearance of weak acid sites upon water treatment. These type of weak acid sites were attributed to unsaturated atom in a defective zeolite framework [259], or extraframework $Al(OH)_3$ and $Al(OH)^{2+}$ [260, 261]. However, since the TCD signal of Na-X-H_2O starts to rise at around 650 K, one can suppose that a small amount of these sites still exist on the zeolite surface. These results confirm the hypothesis formulated on the basis of FTIR (**Figure 8.5**) and elemental analysis (**Table 8.1**).

The amount of strong acid sites is similar between Na-X and Na-X-H$_2$O with 0.16 and 0.15 mmol g^{-1}, respectively. Such value, far below the theoretical maximum value of acid sites reported for H-USY (3 mmol g^{-1}) [262], is explained by the Na$^+$ form of the zeolite.
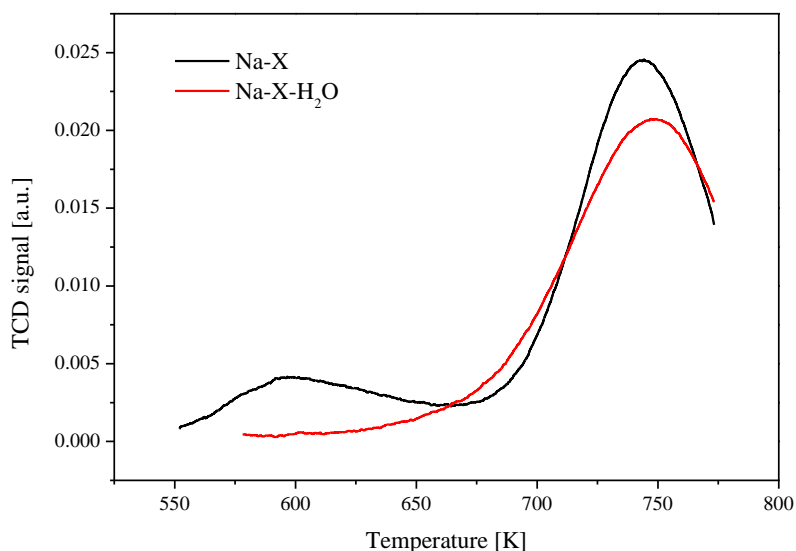
Figure 8.7 TPD spectra of pyridine of Na-X and Na-X-H$_2$O

In conclusion the water treatment applied to Na-X was found to reduce the Al content as shown by the elemental analysis, without affecting the crystallinity of the framework. The analysis of the zeolite surface by FTIR and pyridine TPD suggests that the extraframework alumina species are removed.

8.3.2   Butadiene Adsorption

Adsorption of butadiene at 100 ppmv was performed over Na-X and Na-X-H$_2$O. The butadiene breakthrough curves are shown in **Figure 8.8**. The adsorption capacity is calculated by integration of the area defined by the butadiene and the argon breakthrough curves.
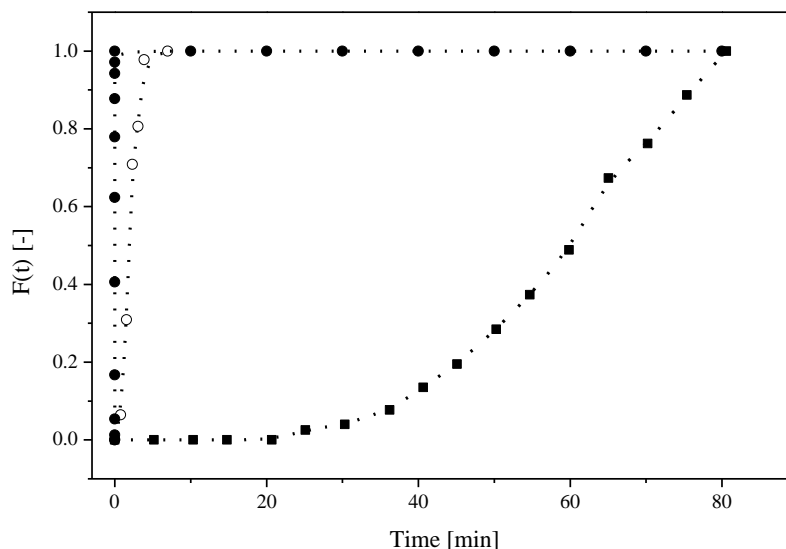
Figure 8.8 Butadiene (100 ppmv) breakthrough curves of Na-X (○), Na-X-H$_2$O (■) and 2% (v/v) Argon tracer (●). Total flow rate (STP) 300 cm^3 min^{-1} (298 K)

As depicted in **Figure 8.8**, the adsorption capacity towards butadiene drastically increases upon water treatment. The adsorption capacity of original Na-X is close to zero whereas it reaches 7.2 wt. % for water modified zeolites. The butadiene outlet concentration remains zero for around 20 minutes with Na-X-H$_2$O indicating total butadiene removal. It is, therefore, an efficient adsorbent for butadiene.

8.3.3   Butadiene Adsorption Mechanism

The *in situ* FTIR spectrum of butadiene adsorption on Na-X-H$_2$O is shown in **Figure 8.9**. As can be observed with the increase of the 3000-3500 cm^{-1} broad bands, cooling the sample from 573 to 298 K under N$_2$ flow leads to partial rehydroxylation due to the moisture present in the gas flow. The sharp band appearing at 3693 cm^{-1} when cooling the sample is attributed to the rehydroxylation of remaining extraframework Al sites.

Once Na-X-H$_2$O is exposed to butadiene at 298 K, the band at 3693 cm^{-1} suddenly decreases. Simultaneously C-H bands are observed around 3000 cm^{-1} indicating butadiene adsorption. Those results indicate an interaction of butadiene with the zeolite surface. For comparison similar experiments were carried out over Na-X. As observed in **Figure 8.10** with the band at 3693 cm^{-1} rehydroxylation of OH sites in Na-X also occurs when cooling down the sample to 298 K. However, the exposition of Na-X to butadiene leads neither to adsorption (**Figure 8.8**) nor to a decrease of the 3693 cm^{-1} band. Instead, constant rehydroxylation takes place indicating that the OH band at 3693 cm^{-1} is not representative of an adsorption site. Some publications suggest interactions between olefin bonds and Brønsted acid sites (Si-OH-Al) [251, 263]. However, it appears to be unlikely for Na-X since only a very small number of Brønsted were measured in Na-X-H$_2$O (**Figure 8.7**). Similarly to molecular simulation of alkene adsorption in zeolites [264], one may suggests that the double bond of butadiene is linked to an oxygen of the zeolite lattice.

Hence it is suggested that a high presence of extraframework Al prevents the interactions between butadiene and the double bond of butadiene. Consequently the removal of these Al species allows butadiene-zeolite interactions, increasing considerably the zeolite adsorption capacity.
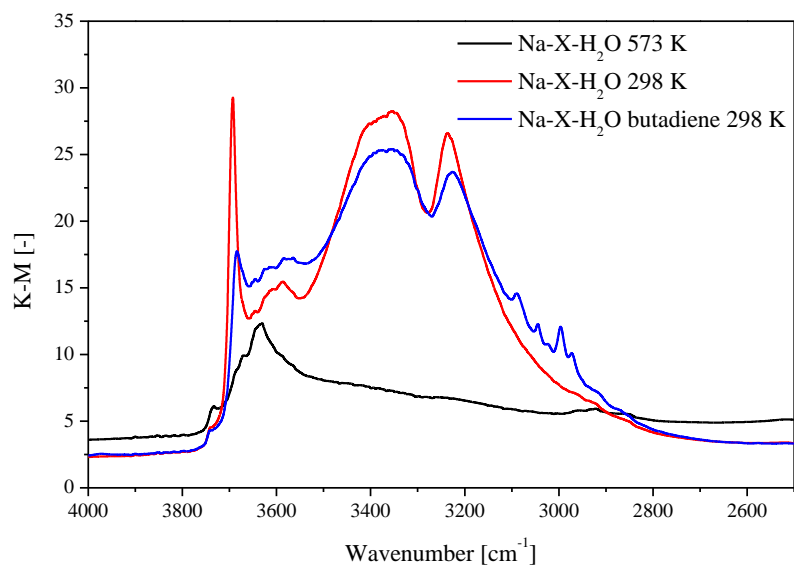
Figure 8.9 *in situ* FTIR spectra of butadiene adsorption on Na-X-H₂O
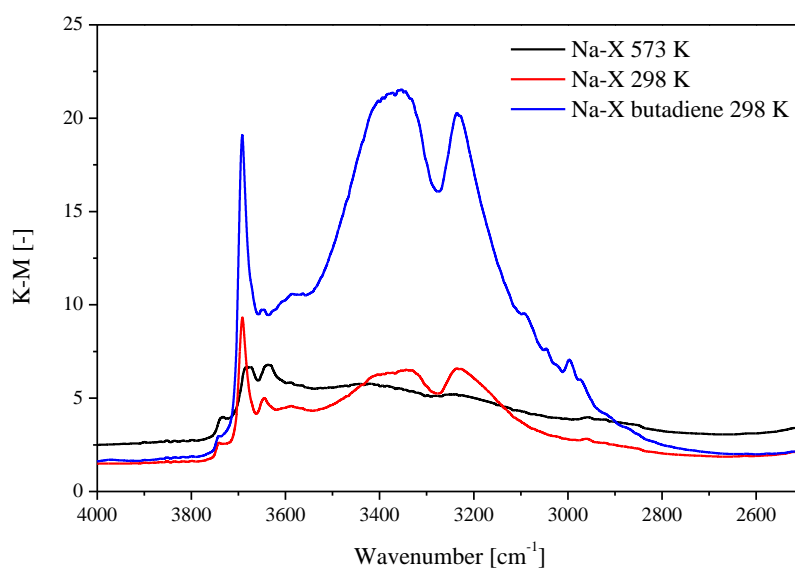
Figure 8.10 *in situ* FTIR spectra of butadiene adsorption on Na-X

8.3.4   Butadiene Adsorption Isotherms

Butadiene adsorption isotherm over Na-X-H_2O was measured to get a deeper insight into the adsorption thermodynamic parameters. By varying the butadiene concentration (25-300 ppmv) and temperature of adsorption (298-333K) a set of adsorption isotherms was obtained for Na-X-H_2O. The Dubinin-Astakhov (D-A) model was used to fit the experimental data [201]. This model is a generalization of the Dubinin-Radushkevich model originally developed for benzene adsorption on activated carbon [202]. It was developed for sub-critical vapors in microporous solid where the adsorption follows a pore filling mechanism. A liquid-like adsorbed phase in the micropores is assumed. The D-A equation takes the following form:

$$W = W_0 \exp\left(-\left(\frac{A}{\beta E_0}\right)^N\right)$$
(8.1)

The model variables are the maximum adsorbed volume (W_0) and the characteristic adsorption energy (E_0). The parameter β is a constant which depends on the nature of the adsorbate, called the affinity coefficient. A β value of 0.97 was obtained for butadiene using the molar volume prediction [208]. The parameter A represents the Polyani adsorption potential. The value of A is equal to the difference between the chemical potential of the adsorbate in the liquid state and in the adsorbed state at the same temperature.

$$A = RT \ln\left(\frac{p_0}{p}\right)$$
(8.2)

Where p_0 is the vapor pressure, p is the adsorbate partial pressure and T is the temperature at which the adsorption experiment took place. In this model the adsorbed phase is supposed to be liquid. For sake of simplicity, the maximum adsorbed volume (cm^3 g^{-1}) is expressed as the saturation capacity (mol kg^{-1}) via the liquid molar volume. The variation of

the liquid molar volume with temperature is taken into account by the thermal expansion coefficient of the saturation capacity. This parameter has been fixed to 0.001 [209]. The full development of the D-A equations can be found in **Chapter 4**.

The isosteric adsorption enthalpy can be calculated by combining the D-A model with the van't Hoff and the Clausius-Clapeyron equations.

$$-\Delta H = \Delta H_{vap} + \beta E_0 \left(\ln\left(\frac{1}{\theta}\right) \right)^{1/N} + \frac{\beta E_0 \delta T}{N} \left(\ln\left(\frac{1}{\theta}\right) \right)^{-1/N} \tag{8.3}$$

with

$$\theta = \frac{q}{q_{max}} \tag{8.4}$$

Where ΔH_{vap} is the heat of condensation. For butadiene -22.7 kJ mol^{-1} is used [265].

The isosteric adsorption enthalpy is therefore the summation of three terms. The first represents the adsorption potential, the second is the heat of vaporization and the third expresses the influence of the maximum capacity change with temperature. The isosteric adsorption enthalpy is by definition larger than the heat of vaporization and depends on the characteristic adsorption energy (E_0) and on the adsorbent loading (θ). The maximum adsorption capacity and the characteristic adsorption energy were obtained by fitting the experimental data to equation 8.1 for all the isotherms as shown in **Figure 8.11**.
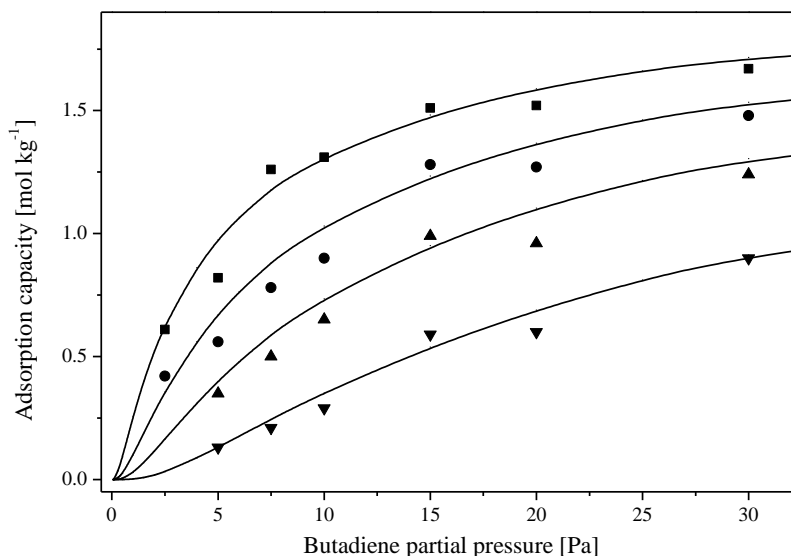
Figure 8.11 Butadiene adsorption isotherm on Na-X-H_2O fitted with the D-A model at different temperature: 298 K (■), 308 K (●), 318 K (▲), 333 K (▼)

A good fitting of the experimental points is obtained with the D-A equation. The curve determination coefficient (R^2) was 0.97. The parameters (E_0, q_{max} and N) used to fit the experimental data are presented in **Table 8.2**. The model predicts a maximum adsorption capacity at 298 K of 2.07 mol kg^{-1}. Therefore at 30 Pa (300 ppmv) a coverage close to 0.8 is already obtained indicating the efficiency of Na-X-H_2O for the adsorption of diluted butadiene. Adsorption of 2.07 mole of butadiene per kilo of adsorbent represents a volume of 0.17 cm^3 g^{-1} whereas the total pore volume calculated from the BET equation was around 0.28 cm^3 g^{-1} (**Figure 8.2**). The difference between the maximum adsorption capacity calculated with butadiene adsorption and the N_2 adsorption isotherm can be explained by the nature of the D-A equation. Since this equation considers only the micropore filling, the eventual adsorption on the zeolite outer surface is not taken into account whereas it was considered in the volume calculated from the N_2 adsorption isotherm. Considering only the microporous part of the zeolite, a volume of 0.19 cm^3 g^{-1} was calculated at p/p$_0$ = 0.2. This value is close to

the maximum butadiene volume adsorbed calculated from the D-A equation confirming the pore filling adsorption mechanism suggested by the model. At saturation butadiene is then filling almost entirely the zeolite framework.

Hence the modification of Na-X is probably occurring in the whole zeolite framework allowing an almost complete micropore filling by butadiene in Na-X-H_2O at saturation condition. Such pore filling is possible in Na-X-H_2O due to a more favorable surface chemistry obtained by the removal of extraframework Al species.

The relatively large N value obtained for the fitting of the D-A equation to the experimental data (**Table 8.2**) indicates a homogeneity of the micropore size. Indeed the exponent of the D-A equation indicates qualitatively the pore size heterogeneity. Low N values (1-2) are generally obtained when fitting non-homogeneous microporous adsorbents [201, 207] whereas N values comprised between 4 and 6 are commonly found for small and homogenous micropores such as zeolites [212].

The energetic parameter of the D-A equation (E_0) has been calculated at 21.5 kJ mol^{-1} indicating moderate adsorption strength due to the high volatility of butadiene. For comparison hexane has characteristic adsorption energy of 30 kJ mol^{-1} on carbon molecular sieve whereas it is only 17 kJ mol^{-1} for ethane on the same adsorbent [266].

Table 8.2 Parameters of the D-A equation for butadiene adsorption on Na-X-H_2O

Sample	q_{max} [mol kg^{-1}]	E_0 [kJ mol^{-1}]	N
Na-X-H_2O	2.05±0.02	21.5±0.5	6±0.05

The isosteric enthalpy of adsorption was calculated using equation 8.3 and the parameters obtained from equation 8.1. The adsorption enthalpy is obtained by a summation of the vaporization enthalpy, the energetic parameter (E_0) and the influence of the maximum capacity variation with temperature. A value of -45 kJ mol^{-1} was obtained for a fractional loading of 0.63. Since the pore size is extremely homogeneous in zeolite, the influence of the fractional loading on the enthalpy of adsorption was extremely small (~5 kJ mol^{-1}). For comparison Eder and Lercher reported a slightly lower value for butane adsorption on Na-X (-34 kJ mol^{-1}) [267] whereas -50 kJ mol^{-1} was reported on silicalite [268]. The enthalpy of adsorption of 1-butene was found by numerical simulation at -48 kJ mol^{-1}. Hence the adsorption enthalpy for butadiene on Na-X-H_2O is in the same range validating the adsorption model used.

8.3.5   Temperature-Programmed Desorption of Butadiene

The interaction between butadiene and active adsorption sites was characterized by temperature-programmed desorption. It allowed to quantify the adsorption energy and can be considered as a complementary method to adsorption isotherm. Desorption of butadiene from Na-X-H_2O was studied with different temperature ramps. The TPD profiles are presented in **Figure 8.12**.
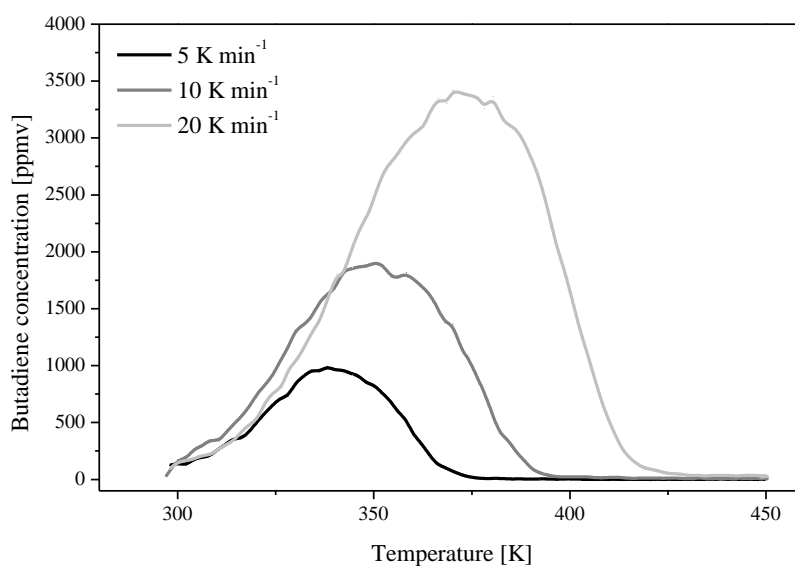
Figure 8.12 TPD profiles: desorption of butadiene from Na-X-H_2O at different temperature

ramp (100 cm^3 min^{-1})

The experiment was carried out by monitoring mass 54 corresponding to the molecular

ion of butadiene at the reactor outlet. The TPD profile shows only one desorption peak

signifying that one type of adsorption site is present in the zeolite channels. The integration of

the butadiene desorption curve revealed that all the adsorbed butadiene could not be desorbed.

The mass balance was systematically smaller than 1. Screening of other desorbed mass was

performed with the mass spectrometer but only butadiene was detected. The incomplete

desorption of butadiene was confirmed by a set of adsorption-desorption cycles where a

systematic decrease of the adsorption capacity was observed. This phenomenon suggests that

a heavy compound such as an oligomer or polymer is formed in the zeolite either during the

adsorption process or at higher temperature during the TPD.

The increase of the temperature ramps shifts the maximum desorption rate to a higher

temperature, characterized by the top of the desorption peak. The kinetic desorption

parameters, the activation energy of desorption (E_d) and the kinetic constant (k) were obtained

by numerical simulation of butadiene desorption. These two parameters were varied to obtain the best fit to the experimental points. The simulations were performed at different temperature ramps. Since in TPD experiment the temperature increases linearly, desorption rate changes. By solving the mass balance and the temperature variation simultaneously a desorption curve is obtained. The development of the equation used to simulate desorption curves is presented in **Chapter 4**. The gas phase concentration of desorbed species in function of temperature is then obtained. An example is shown in **Figure 8.13**.
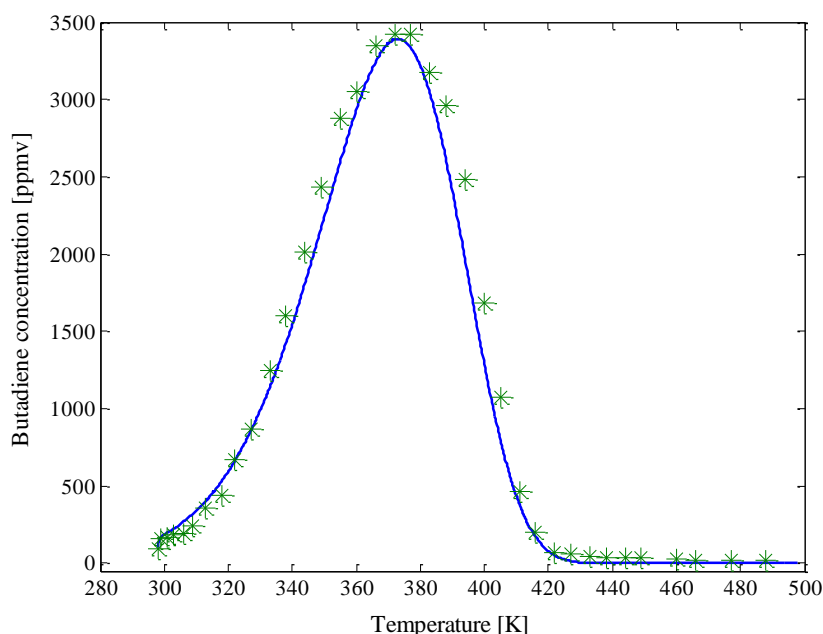
Figure 8.13 Simulation of butadiene TPD pattern on Na-X-H_2O (20 K min^{-1}, 100 cm^3 min^{-1})

The activation energy of desorption (E_d) obtained for the butadiene zeolite system was constant for all the simulations performed. The simulations fit very well the butadiene desorption data. Since the model applied supposed 1st order desorption kinetics, we suggest that such desorption kinetics take place for the butadiene/Na-X-H_2O system. The model gives

an activation energy of desorption of 47.5±2 kJ mol^{-1}. The activation energy of adsorption being negligible, the enthalpy of adsorption is represented by the activation energy of desorption.

As can be seen a good fit is obtained with the simulated curve. The mass transfer influence noticed in **Chapter 4** for toluene is apparently avoided for butadiene on Na-X-H$_2$O because of the lower quantities adsorbed. The value of adsorption enthalpy is very close to the value determined by modelling of adsorption isotherms. Moreover, they correspond to the adsorption enthalpy of 1-butene, a very similar molecule. The interactions created between the zeolite active site and butadiene coupled with the narrow microporosity of zeolite is likely the driving force of butadiene adsorption. The porosity itself is not sufficient to have a large adsorption capacity since original Na-X showed extremely limited butadiene removal.

8.4 Conclusions

This chapter reports the adsorption of diluted butadiene over zeolites. The water treatment followed by a calcination of commercial Na-X zeolites is reported to considerably increase its efficiency for butadiene removal. The two adsorbents, Na-X and Na-X-H$_2$O were compared in order to get an insight on the adsorption mechanism. Bulk characterization of Na-X and Na-X-H$_2$O revealed a similar microporosity and crystallinity whereas surface characterization by FTIR and pyridine TPD showed the removal of extraframework Al species. The presence of these species on the zeolite surface was suggested to prevent butadiene adsorption. The adsorption mechanism was studied by *in situ* FTIR adsorption of butadiene confirming this suggestion. By their removal, the adsorption capacity was considerably increased due to favorable chemical interactions and optimal microporosity of the zeolite. A set of butadiene adsorption isotherms and its modelling with the D-A equation was performed. Subsequently, the adsorption enthalpy was calculated. The value reported is

in the same range compared to 1-butene adsorption on zeolites. To further confirm the results obtained, butadiene TPD experiments were carried out. A simulation of the TPD pattern allowed a good fitting of the experimental data and adsorption enthalpy was calculated. Identical thermodynamic parameters were calculated as compared to isotherm experiments.

9 General Conclusions and Perspectives

This chapter summarizes the results obtained in this study. The general conclusions and the outlook are also presented.

9.1 Conclusions

The main objective set for this thesis was the development of efficient adsorbents for the removal of volatile organic compounds at low concentration and short contact time (20 ms). Moreover pressure drop and gas flow mal-distribution should be avoided in the adsorbent bed. In order to achieve these goals, specific surface modifications of commercial adsorbents depending on the VOC physical properties were carried out. Activated carbon fibers and zeolites were used as commercial basis for functionalized adsorbents.

Effect of ACFs morphology and surface chemistry on toluene and acetaldehyde adsorption

In a first step, the effect of the morphology of ACFs on toluene removal was studied. Two microporous ACFs with low oxygen content were used. The characterization revealed supermicroporous (d_p 1-2 nm) and ultramicroporous ($d_p < 1$ nm) adsorbents with similar surface chemistry. Toluene adsorption isotherms over two ACFs were obtained. The modelling of the isotherms suggested an adsorption mechanism by micropore filling for both microporous ACFs. The toluene adsorption enthalpy obtained from the isotherm modelling was found higher for the ultramicroporous sample. To confirm these results toluene temperature-programmed desorption was used as a method to evaluate the adsorption enthalpy and similar results were obtained.

The effect of the surface chemistry on the removal of toluene and acetaldehyde was studied using ACFs with similar morphology but different surface chemistry. The hydrophilic character of the ACFs was gradually increased by means of nitric acid treatment. The increase of the oxygen content of the ACFs was found to enhance the interactions with acetaldehyde. A hydrogen bonding mechanism was suggested. On the contrary the hydrophilic surface

decreased the toluene removal capacity due to unfavorable surface chemistry and the decrease of the micropore volume.

Hence, the effect of the surface chemistry and the ACFs morphology were studied for the removal of acetaldehyde and toluene at low concentration. Hydrophobic surfaces with ultramicroporosity were identified as the two key parameters to design an optimized adsorbent for non-polar high boiling point VOC such as toluene. For polar high boiling point VOC such as acetaldehyde, the surface chemistry is the main parameter to optimize. An increased adsorption capacity is reported for hydrophilic ACFs surface.

Creation of specific sites on ACFs for formaldehyde and acetaldehyde adsorption

Although the performance of ACFs towards acetaldehyde was significantly enhanced by a hydrophilic surface the adsorption capacities could be further increased by specific surface functionalization of ACFs. The acetaldehyde removal was improved via the deposition of basic metal oxide NPs on the surface of ACFs. Such adsorbents take advantage of the intrinsic high adsorption capacity of metal oxide NPs and avoid the problems of the pressure drop and mass transfer through the adsorbent bed due to the ACFs morphology. The deposition of NPs of MgO, CaO and La_2O_3 was found to greatly increase the adsorption capacity towards acetaldehyde. An adsorption mechanism was suggested based on the TPD pattern.

A novel adsorbent obtained by the deposition of a diethylene triamine (DETA) layer on the ACFs surface was developed for formaldehyde removal. The amino groups contained in DETA were found to interact with formaldehyde and a 50-fold adsorption capacity increase was reported as compared to original ACFs.

Hence, the functionalization of ACFs by creating specific sites for selective adsorption is a valuable strategy for diluted VOC removal.

Zeolite as specific adsorbent for butadiene

The development of a zeolite based adsorbent was performed for the adsorption of butadiene. Commercial zeolites were modified through a water treatment followed by calcination to create a more favorable surface. The removal of zeolites extraframework cations is suggested, allowing interactions between butadiene and the framework. A 50-fold increase in adsorption capacity is reported upon such surface modification. The adsorption enthalpy was obtained from adsorption isotherms and via TPD methods with conclusive results indicating strong physisorption.

9.2 Further Development

With regards to toluene adsorption on ACFs, the thermodynamic parameters governing the adsorption have been determined. However this study does not report the effect of the pore size on the adsorption kinetics. A deeper study and a modeling of the adsorption breakthrough curve supported by the thermodynamic data presented in this thesis could allow understanding the kinetic of adsorption and the mass transfer limitations [269, 270]. A comparative study of the ultramicroporous and the supermicroporous adsorbent could reveal the dependence of the adsorption kinetic on the micropore size.

The oxidation of the ACFs surface was shown to enhance the adsorption capacity towards acetaldehyde and was attributed to the largest surface oxygen content. However, the ACFs characterization revealed the presence of several types of O-containing groups and their specific contribution in the acetaldehyde adsorption process was not studied. An interesting

study would be to establish specifically the adsorption potential of each type of O-containing group.

Although a large adsorption capacity increase towards formaldehyde was noticed upon DETA deposition, a deactivation occurred during storage. Reaction between O-containing groups and DETA were suggested, but no clear evidence has been obtained. Moreover, neither the thermodynamic adsorption parameters nor the adsorption mechanism were studied. Hence, deeper studies on this adsorbent could be carried out with IR characterization and by exactly quantifying the amino groups.

The deposition of metal oxide NPs on the ACFs surface was reported to greatly increase its adsorption capacity towards acetaldehyde. A decrease of the removal capacity was also noticed for metal oxide NPs deposited on ACF-2 in presence of CO_2. However, when changing the support from ACF-2 to ACF-1, a constant adsorption capacity was reported regardless of the presence of CO_2 in the gas stream. The interactions between CO_2 and the NPs suggested by the lower adsorption capacity reported for ACF-2 are therefore not occurring with ACF-1 as a support. The reasons of the higher stability of ACF-1 are not clearly established and further studies would be needed. The effect of the pore size on the metal oxide particles size could be an explanation but deeper characterization is necessary.

Regarding the removal of butadiene, the water treatment of Na-X was suggested to remove the extraframework Al allowing interactions between butadiene and the zeolite lattice. Although the suggested interactions seemed reasonable, the exact adsorption mechanism remains unknown. Moreover since zeolites were used in the form of pellets of ~500 μm, internal mass transfer resistance and flow mal-distribution may occur. To circumvent this drawback, the deposition of zeolite microcrystals on microfibers has to be studied.

10 References

[1]   M. Tancrede, R. Wilson, L. Zeise and E.A.C. Crouch, Atmos. Environ., 21 (1987) 2187.

[2]   A.K. Ghoshal and S.D. Manjare, J. Loss Prev. Process Ind., 15 (2002) 413.

[3]   J. Dewar, Proc. R. Soc. London, 74 (1904) 127.

[4]   J. Lee, J. Kim and T. Hyeon, Adv. Mater., 18 (2006) 2073.

[5]   C.S. Cundy and P.A. Cox, Chemical Reviews, 103 (2003) 663.

[6]   A. Dabrowski, Adv. Colloid Interface Sci., 93 (2001) 135.

[7]   G.D. Parfitt and C.H. Rochester, Adsorption from solution at the solid/liquid interface, Academic Press, London ; New York, 1983.

[8]   D.M. Ruthven, Principles of adsorption and adsorption processes, New York, 1984.

[9]   R.T. Yang, Gas separation by adsorption processes, Butterworths, Boston, 1987.

[10]   R.T. Yang, Adsorbents: Fundamentals and Applications, A John Wiley & Sons, Inc., Publication, Hoboken, New Jersey, 2003.

[11]   P. Branton and R.H. Bradley, Adsorpt.-J. Int. Adsorpt. Soc., 17 (2011) 293.

[12]   K.S.W. Sing, D.H. Everett, R.A.W. Haul, L. Moscou, R.A. Pierotti, J. Rouquerol and T. Siemieniewska, Pure Appl. Chem., 57 (1985) 603.

[13]   S.D. Piccot, J.J. Watson and J.W. Jones, J. Geophys. Res.-Atmos., 97 (1992) 9897.

[14]   C.F. Wu, S.Y. Wu, Y.H. Wu, A.C. Cullen, T.V. Larson, J. Williamson and L.J.S. Liu, Environ. Int., 35 (2009) 516.

[15]   IARC Monographs on the evaluation of carcinogenic risks to humans, Re-evaluation of Some Organics Chemicals, Hydrazine and Hydrogen Peroxide, Vol. 71, 1998, p. 319.

[16]   U.S.E.P. Agency, The Plain English Guide to the Clean Air Act, Vol. 2012, EPA, 2012 (last update).

[17]   F.I. Khan and A.K. Ghoshal, J. Loss Prev. Process Ind., 13 (2000) 527.

[18]   E.N. Ruddy and L.A. Carroll, Chem. Eng. Prog., 89 (1993) 28.

[19]   K. Urashima and J.S. Chang, IEEE Trns. Dielectr. Electr. Insul., 7 (2000) 602.

[20]   J. Van Durme, J. Dewulf, C. Leys and H. Van Langenhove, Appl. Catal. B-Environ., 78 (2008) 324.

[21]   C. Lahousse, A. Bernier, P. Grange, B. Delmon, P. Papaefthimiou, T. Ioannides and X. Verykios, J. Catal., 178 (1998) 214.

[22]   M.C. Delhomenie and M. Heitz, Crit. Rev. Biotechnol., 25 (2005) 53.

[23]   C. Kennes and F. Thalasso, J. Chem. Technol. Biotechnol., 72 (1998) 303.

[24]   A. Gabelman and S.T. Hwang, J. Membr. Sci., 159 (1999) 61.

[25]   G.R. Parmar and N.N. Rao, Crit. Rev. Environ. Sci. Technol., 39 (2009) 41.

[26]   W.B. Li, J.X. Wang and H. Gong, Catal. Today, 148 (2009) 81.

[27]   K. Everaert and J. Baeyens, J. Hazard. Mater., 109 (2004) 113.

[28]   M.B. Chang and H.M. Lee, Catal. Today, 89 (2004) 109.

[29]   L. Intriago, E. Díaz, S. Ordóñez and A. Vega, Microporous Mesoporous Mat., 91 (2006) 161.

[30]   S. Delagrange, L. Pinard and J.-M. Tatibouët, Applied Catalysis B: Environmental, 68 (2006) 92.

[31]   M. Magureanu, N.B. Mandache, V.I. Parvulescu, C. Subrahmanyam, A. Renken and L. Kiwi-Minsker, Applied Catalysis B: Environmental, 74 (2007) 270.

[32]   H.H.J. Cox and M.A. Deshusses, Chem. Eng. J., 87 (2002) 101.

[33]   C. Kennes, H.H.J. Cox, H.J. Doddema and W. Harder, J. Chem. Technol. Biotechnol., 66 (1996) 300.

[34]   B. Guieysse, C. Hort, V. Platel, R. Munoz, M. Ondarts and S. Revah, Biotechnol. Adv., 26 (2008) 398.

[35]   Y.C. Chung, Y.Y. Lin and C.P. Tseng, Bioresour. Technol., 96 (2005) 1812.

[36]   C. Alonso, M.T. Suidan, G.A. Sorial, F.L. Smith, P. Biswas, P.J. Smith and R.C. Brenner, Biotechnol. Bioeng., 54 (1997) 583.

[37]   G. Busca, S. Berardinelli, C. Resini and L. Arrighi, J. Hazard. Mater., 160 (2008) 265.

[38]   G. Darracq, A. Couvert, C. Couriol, A. Amrane, D. Thomas, E. Dumont, Y. Andres and P. Le Cloirec, J. Chem. Technol. Biotechnol., 85 (2010) 309.

[39]   E. Dumont, G. Darracq, A. Couvert, C. Couriol, A. Amrane, D. Thomas, Y. Andres and P. Le Cloirec, Chem. Eng. J., 162 (2010) 927.

[40]   E. Dumont, G. Darracq, A. Couvert, C. Couriol, A. Amrane, D. Thomas, Y. Andres and P. Le Cloirec, Chem. Eng. J., 168 (2011) 241.

[41]   G. Quijano, A. Couvert, A. Amrane, G. Darracq, C. Couriol, P. Le Cloirec, L. Paquin and D. Carrie, Chem. Eng. Sci., 66 (2011) 2707.

[42]   B. Ozturk and D. Yilmaz, Process Safety and Environmental Protection, 84 (2006) 391.

[43]   R. W. Baker, N. Yoshioka, J. M. Mohr and A. J. Khan, J. Membr. Sci., 31 (1987) 259.

[44]   M. Leemann, G. Eigenberger and H. Strathmann, J. Membr. Sci., 113 (1996) 313.

[45]   H. Paul, C. Philipsen, F.J. Gerner and H. Strathmann, J. Membr. Sci., 36 (1988) 363.

[46]   K. Kimmerle, C.M. Bell, W. Gudernatsch and H. Chmiel, J. Membr. Sci., 36 (1988) 477.

[47]   H. Jüntgen, Carbon, 15 (1977) 273.

[48]   S. Sircar, T.C. Golden and M.B. Rao, Carbon, 34 (1996) 1.

[49]   M.E. Davis, Nature, 417 (2002) 813.

[50]   R.E. Morris and P.S. Wheatley, Angew. Chem.-Int. Edit., 47 (2008) 4966.

[51]   M. Kondo, T. Yoshitomi, K. Seki, H. Matsuzaka and S. Kitagawa, Angew. Chem.-Int. Edit., 36 (1997) 1725.

[52]   H. Marsh and F. Rodríguez-Reinoso, Activated carbon, Elsevier, Amsterdam ; Boston, 2006.

[53]   J.X. Jiang, F. Su, A. Trewin, C.D. Wood, H. Niu, J.T.A. Jones, Y.Z. Khimyak and A.I. Cooper, J. Am. Chem. Soc., 130 (2008) 7710.

[54]   C.D. Wood, B. Tan, A. Trewin, H.J. Niu, D. Bradshaw, M.J. Rosseinsky, Y.Z. Khimyak, N.L. Campbell, R. Kirk, E. Stockel and A.I. Cooper, Chem. Mat., 19 (2007) 2034.

[55]   S. Brunauer, P.H. Emmett and E. Teller, J. Am. Chem. Soc., 60 (1938) 309.

[56]   S.J. Gregg and K.S.W. Sing, Adsorption, surface area, and porosity, Academic Press, London ; New York, 1982.

[57]   S. Lowell, J.E. Shields, M.A. Thomas, M. Thommes and SpringerLink (Online service), Characterization of Porous Solids and Powders: Surface Area, Pore Size and Density, Particle Technology Series,, Springer Netherlands : Imprint: Springer, Dordrecht, 2004.

[58]   F. Rouquerol, J. Rouquerol and K.S.W. Sing, Adsorption by powders and porous solids : principles, methodology and applications, Academic Press, San Diego, 1999.

[59]   A.L. McClellan and H.F. Harnsberger, J. Colloid Interface Sci., 23 (1967) 577.

[60]   D. Cazorla-Amoros, J. Alcaniz-Monge and A. Linares-Solano, Langmuir, 12 (1996) 2820.

[61]   J. Garrido, A. Linaressolano, J.M. Martinmartinez, M. Molinasabio, F. Rodriguezreinoso and R. Torregrosa, Langmuir, 3 (1987) 76.

[62]   P.I. Ravikovitch, A. Vishnyakov, R. Russo and A.V. Neimark, Langmuir, 16 (2000) 2311.

[63]   T. Kyotani, Carbon, 38 (2000) 269.

[64]   E.P. Barrett, L.G. Joyner and P.P. Halenda, J. Am. Chem. Soc., 73 (1951) 373.

[65]   Dollimor.D and G.R. Heal, J. Colloid Interface Sci., 33 (1970) 508.

[66]   G. Horvath and K. Kawazoe, J. Chem. Eng. Jpn., 16 (1983) 470.

[67]   S. Storck, H. Bretinger and W.F. Maier, Appl. Catal. A-Gen., 174 (1998) 137.

[68]   J. Jagiello and M. Thommes, Carbon, 42 (2004) 1227.

[69]   Z.Y. Ryu, J.T. Zheng, M.Z. Wang and B.J. Zhang, Carbon, 37 (1999) 1257.

[70]   C. Nguyen and D.D. Do, Langmuir, 15 (1999) 3608.

[71]   K.S.W. Sing, Chem. Ind., (1968) 1520.

[72]   K.S.W. Sing, Chem. Ind., (1967) 829.

[73]   J. Choma, M. Kloske and M. Jaroniec, J. Colloid Interface Sci., 266 (2003) 168.

[74]   P.J.M. Carrott, R.A. Roberts and K.S.W. Sing, Carbon, 25 (1987) 59.

[75]   N. Setoyama, T. Suzuki and K. Kaneko, Carbon, 36 (1998) 1459.

[76]   M. Kruk, M. Jaroniec and J. Choma, Carbon, 36 (1998) 1447.

[77]   M.J. Selles-Perez and J.M. Martin-Martinez, J. Chem. Soc.-Faraday Trans., 87 (1991) 1237.

[78]   P.J. Branton, K.S.W. Sing and J.W. White, J. Chem. Soc.-Faraday Trans., 93 (1997) 2337.

[79]   M.A. Hernandez, J.A. Velasco, M. Asomoza, S. Solis, F. Rojas and V.H. Lara, Ind. Eng. Chem. Res., 43 (2004) 1779.

[80]   Q.L. Huang, H. Vinh-Thang, A. Malekian, M. Eic, D. Trong-On and S. Kaliaguine, Microporous Mesoporous Mat., 87 (2006) 224.

[81]   J.H. Choung, Y.W. Lee, D.K. Choi and S.H. Kim, J. Chem. Eng. Data, 46 (2001) 954.

[82]   Y.C. Chiang, P.C. Chiang and C.P. Huang, Carbon, 39 (2001) 523.

[83]   Y. Ueno, A. Tate, O. Niwa, H.-s. Zhou, T. Yamada and I. Honma, Chemical Communications, (2004) 746.

[84]   X. Hu, S. Qiao, X.S. Zhao and G.Q. Lu, Ind. Eng. Chem. Res., 40 (2001) 862.

[85]   K. Kosuge, S. Kubo, N. Kikukawa and M. Takemori, Langmuir, 23 (2007) 3095.

[86]   S.Z. Qiao, S.K. Bhatia and D. Nicholson, Langmuir, 20 (2004) 389.

[87]   X.S. Zhao, Q. Ma and G.Q.M. Lu, Energy Fuels, 12 (1998) 1051.

[88]   M.J. Ruhl, Chem. Eng. Prog., 89 (1993) 37.

[89]   N. Mohan, G.K. Kannan, S. Upendra, R. Subha and N.S. Kumar, J. Hazard. Mater., 168 (2009) 777.

[90]   S.W. Park, B.S. Choi and J.W. Lee, Sep. Sci. Technol., 42 (2007) 2221.

[91]   K.P. Singh, D. Mohan, G.S. Tandon and G.S.D. Gupta, Ind. Eng. Chem. Res., 41 (2002) 2480.

[92]   D. Das, V. Gaur and N. Verma, Carbon, 42 (2004) 2949.

[93]   M.A. Lillo-Rodenas, A.J. Fletcher, K.M. Thomas, D. Cazorla-Amoros and A. Linares-Solano, Carbon, 44 (2006) 1455.

[94]   D.G. Lee, J.H. Kim and C.H. Lee, Sep. Purif. Technol., 77 (2011) 312.

[95]   H. Teng and C.-T. Hsieh, Ind. Eng. Chem. Res., 37 (1998) 3618.

[96]   A. Silvestre-Albero, J.M. Ramos-Fernández, M. Martínez-Escandell, A. Sepúlveda-Escribano, J. Silvestre-Albero and F. Rodríguez-Reinoso, Carbon, 48 (2010) 548.

[97]   A. Badalyan, R. Bromball, P. Pendleton and W. Skinner, Carbon, 48 (2010) 1004.

[98]   D. Lozano-Castello, M.A. Lillo-Rodenas, D. Cazorla-Amoros and A. Linares-Solano, Carbon, 39 (2001) 741.

[99]   M.A. Lillo-Rodenas, D. Lozano-Castello, D. Cazorla-Amoros and A. Linares-Solano, Carbon, 39 (2001) 751.

[100]   M.A. Lillo-Rodenas, D. Cazorla-Amoros and A. Linares-Solano, Carbon, 43 (2005) 1758.

[101]   M.A. Lillo-Rodenas, D. Cazorla-Amoros and A. Linares-Solano, Adsorpt.-J. Int. Adsorpt. Soc., 17 (2011) 473.

[102]   A. Silvestre-Albero, J. Silvestre-Albero, A. Sepúlveda-Escribano and F. Rodríguez-Reinoso, Microporous Mesoporous Mat., 120 (2009) 62.

[103]   K.L. Foster, R.G. Fuerman, J. Economy, S.M. Larson and M.J. Rood, Chem. Mat., 4 (1992) 1068.

[104]   C.L. Mangun, M.A. Daley, R.D. Braatz and J. Economy, Carbon, 36 (1998) 123.

[105]   M.-C. Huang, C.-H. Chou and H. Teng, Aiche J, 48 (2002) 1804.

[106]   E.D. Dimotakis, M.P. Cal, J. Economy, M.J. Rood and S.M. Larson, Environ. Sci. Technol., 29 (1995) 1876.

[107]   A.J. Romero-Anaya, M.A. Lillo-Rodenas and A. Linares-Solano, Carbon, 48 (2010) 2625.

[108]   M.P. Cal, M.J. Rood and S.M. Larson, Gas Sep. Purif., 10 (1996) 117.

[109]   K.H. Park, W.G. Shim, H.K. Shon, S.G. Lee, H.H. Ngo, S. Vigneswaran and H. Moon, Sep. Sci. Technol., 45 (2010) 1084.

[110]   C. Moreno-Castilla, Carbon, 42 (2004) 83.

[111]   T. Garcia, R. Murillo, D. Cazorla-Amoros, A.M. Mastral and A. Linares-Solano, Carbon, 42 (2004) 1683.

[112]   P.A. Bazula, A.H. Lu, J.J. Nitz and F. Schuth, Microporous Mesoporous Mat., 108 (2008) 266.

[113]   J.L. Figueiredo and M.F.R. Pereira, Catal. Today, 150 (2010) 2.

[114]   H.P. Boehm, in H.P. D.D. Eley and B.W. Paul (Editors), Advances in Catalysis, Vol. Volume 16, Academic Press, 1966, p. 179.

[115]   H.P. Boehm, Carbon, 40 (2002) 145.

[116]   U. Zielke, K.J. Huttinger and W.P. Hoffman, Carbon, 34 (1996) 983.

[117]   J.L. Figueiredo, M.F.R. Pereira, M.M.A. Freitas and J.J.M. Orfao, Carbon, 37 (1999) 1379.

[118]   D. Rosenthal, M. Ruta, R. Schlogl and L. Kiwi-Minsker, Carbon, 48 (2010) 1835.

[119]   D.A. Bulushev, I. Yuranov, E.I. Suvorova, P.A. Buffat and L. Kiwi-Minsker, J. Catal., 224 (2004) 8.

[120]   B.K. Pradhan and N.K. Sandle, Carbon, 37 (1999) 1323.

[121]   Salame, II and T.J. Bandosz, J. Colloid Interface Sci., 210 (1999) 367.

[122]   D. Aggarwal, M. Goyal and R.C. Bansal, Carbon, 37 (1999) 1989.

[123]   J.H. Zhou, Z.J. Sui, J. Zhu, P. Li, C. De, Y.C. Dai and W.K. Yuan, Carbon, 45 (2007) 785.

[124]   C.L. Mangun, K.R. Benak, M.A. Daley and J. Economy, Chem. Mat., 11 (1999) 3476.

[125]   T.J. Bandosz, J. Jagiello, J.A. Schwarz and A. Krzyzanowski, Langmuir, 12 (1996) 6480.

[126]   F. Villacanas, M.F.R. Pereira, J.J.M. Orfao and J.L. Figueiredo, J. Colloid Interface Sci., 293 (2006) 128.

[127]   Y. El-Sayed and T.J. Bandosz, Abstr Pap Am Chem S, 224 (2002) U559.

[128]   I.I. Salame and T.J. Bandosz, Langmuir, 16 (2000) 5435.

[129]   Y. El-Sayed and T.J. Bandosz, J. Colloid Interface Sci., 242 (2001) 44.

[130]   Y. El-Sayed and T.J. Bandosz, Langmuir, 18 (2002) 3213.

[131]   Y. Song, W. Qiao, S.H. Yoon, I. Mochida, Q. Guo and L. Liu, J. Appl. Polym. Sci., 106 (2007) 2151.

[132]   P. Chingombe, B. Saha and R.J. Wakeman, Carbon, 43 (2005) 3132.

[133]   M. Abe, K. Kawashima, K. Kozawa, H. Sakai and K. Kaneko, Langmuir, 16 (2000) 5059.

[134]   S. Tanada, N. Kawasaki, T. Nakamura, M. Araki and M. Isomura, J. Colloid Interface Sci., 214 (1999) 106.

[135]   R.J.J. Jansen and H. Vanbekkum, Carbon, 33 (1995) 1021.

[136]   C.L. Mangun, K.R. Benak, J. Economy and K.L. Foster, Carbon, 39 (2001) 1809.

[137]   J. Economy, K. Foster, A. Andreopoulos and H. Jung, Chemtech, 22 (1992) 597.

[138]   J.P. Boudou, Carbon, 41 (2003) 1955.

[139]   F. Adib, A. Bagreev and T.J. Bandosz, Langmuir, 16 (2000) 1980.

[140]   H. Tamai, K. Shiraki, T. Shiono and H. Yasuda, J. Colloid Interface Sci., 295 (2006) 299.

[141]   C.J. Ma, X.H. Li and T.L. Zhu, Carbon, 49 (2011) 2873.

[142]   T. Hayashi, M. Kumita and Y. Otani, Environ. Sci. Technol., 39 (2005) 5436.

[143]   S. Aoki, A. Nakahira, H. Nakayama, K. Sakamoto, S. Yamaguchi and K. Suganuma, J. Phys. Chem. Solids, 65 (2004) 465.

[144]   A.M. Ewlad-Ahmed, M.A. Morris, S.V. Patwardhan and L.T. Gibson, Environ. Sci. Technol., 46 (2012) 13354.

[145]   M.H. Lim and A. Stein, Chem. Mat., 11 (1999) 3285.

[146]   Y. Matsuo, Y. Nishino, T. Fukutsuka and Y. Sugie, Carbon, 45 (2007) 1384.

[147]   Y. Matsuo, Y. Nishino, T. Fukutsuka and Y. Sugie, Carbon, 46 (2008) 1162.

[148]   K.J. Klabunde, J. Stark, O. Koper, C. Mohs, D.G. Park, S. Decker, Y. Jiang, I. Lagadic and D. Zhang, The Journal of Physical Chemistry, 100 (1996) 12142.

[149]   M. Atteya and K.J. Klabunde, Chem. Mat., 3 (1991) 182.

[150]   H.Z. Zhang, R.L. Penn, R.J. Hamers and J.F. Banfield, J. Phys. Chem. B, 103 (1999) 4656.

[151]   P. Jeevanandam, K.J. Klabunde and S.H. Tetzler, Microporous Mesoporous Mat., 79 (2005) 101.

[152]   C.L. Carnes and K.J. Klabunde, Chem. Mat., 14 (2002) 1806.

[153]   J.V. Stark and K.J. Klabunde, Chem. Mat., 8 (1996) 1913.

[154]   R. Richards, W. Li, S. Decker, C. Davidson, O. Koper, V. Zaikovski, A. Volodin, T. Rieker and K.J. Klabunde, J. Am. Chem. Soc., 122 (2000) 4921.

[155]   J.V. Stark, D.G. Park, I. Lagadic and K.J. Klabunde, Chem. Mat., 8 (1996) 1904.

[156]   A. Khaleel, P.N. Kapoor and K.J. Klabunde, Nanostruct. Mater., 11 (1999) 459.

[157]   C.L. Carnes, J. Stipp and K.J. Klabunde, Langmuir, 18 (2002) 1352.

[158]   R.T. Yang, A.J. Hernandez-Maldonado and F.H. Yang, Science, 301 (2003) 79.

[159]   A. van Miltenburg, W. Zhu, F. Kapteijn and J.A. Moulijn, Chem. Eng. Res. Des., 84 (2006) 350.

[160]   L.M. Le Leuch, A. Subrenat and P. Le Cloirec, Environ. Technol., 26 (2005) 1243.

[161]   A.J. Hernandez-Maldonado and R.T. Yang, Catal Rev, 46 (2004) 111.

[162]   A.J. Hernández-Maldonado and R.T. Yang, J. Am. Chem. Soc., 126 (2004) 992.

[163]   A.J. Hernández-Maldonado and R.T. Yang, Ind. Eng. Chem. Res., 42 (2003) 123.

[164]   A. Takahashi, F.H. Yang and R.T. Yang, Ind. Eng. Chem. Res., 41 (2002) 2487.

[165]   A.J. Hernández-Maldonado and R.T. Yang, Ind. Eng. Chem. Res., 43 (2004) 1081.

[166]   A.J. Hernández-Maldonado, F.H. Yang, G. Qi and R.T. Yang, Applied Catalysis B: Environmental, 56 (2005) 111.

[167]   S. Velu, X. Ma and C. Song, Ind. Eng. Chem. Res., 42 (2003) 5293.

[168]   A. Aşkın and C. Bilgiç, Chem. Eng. J., 112 (2005) 159.

[169]   S. Zhen and K. Seff, Microporous Mesoporous Mat., 39 (2000) 1.

[170]   X. Canet, F. Gilles, B.L. Su, G. de Weireld, M. Frere and P. Mougin, J. Chem. Eng. Data, 52 (2007) 2127.

[171]   I. Daems, P. Leflaive, A. Methivier, G.V. Baron and J.F.M. Denayer, Microporous Mesoporous Mat., 96 (2006) 149.

[172]   A. Takahashi and R.T. Yang, Aiche J, 48 (2002) 1457.

[173]   D.M. Ruthven and S.C. Reyes, Microporous Mesoporous Mat., 104 (2007) 59.

[174]   F.A. Da Silva and A.E. Rodrigues, Ind. Eng. Chem. Res., 38 (1999) 2051.

[175]   P.S. Chintawar and H.L. Greene, Appl. Catal. B-Environ., 14 (1997) 37.

[176]   J. Farrell, C. Manspeaker and J. Luo, Microporous Mesoporous Mat., 59 (2003) 205.

[177]   H.F. Cheng and M. Reinhard, Environ. Sci. Technol., 40 (2006) 7694.

[178]   N.Y. Chen, J. Phys. Chem., 80 (1976) 60.

[179]   A. Guillemot, J. Mijoin, S. Mignard and P. Magnoux, Appl. Catal. B-Environ., 75 (2007) 249.

[180]   J. Pires, A. Carvalho and M.B. de Carvalho, Microporous Mesoporous Mat., 43 (2001) 277.

[181]   A. Takahashi, R.T. Yang, C.L. Munson and D. Chinn, Langmuir, 17 (2001) 8405.

[182]   A. Takahashi, R.T. Yang, C.L. Munson and D. Chinn, Ind. Eng. Chem. Res., 40 (2001) 3979.

[183]   B.R. Goodman, W.F. Schneider, K.C. Hass and J.B. Adams, Catal. Lett., 56 (1998) 183.

[184]   A.M. Tsybulevski, L.M. Kustov, K.C. Weston, A.A. Greish, O.P. Tkachenko and A.V. Kucherov, Ind. Eng. Chem. Res., 51 (2012) 7073.

[185]   C. Wagner and K. Hauffe, Zeitschrift Fur Elektrochemie Und Angewandte Physikalische Chemie, 44 (1938) 172.

[186]   C. Wagner and K. Hauffe, Zeitschrift Fur Elektrochemie Und Angewandte Physikalische Chemie, 45 (1939) 409.

[187]   K. Tamaru, Advances in Catalysis, 15 (1964) 65.

[188]   C.O. Bennett, in W.O. Haag, B.C. Gates and H. Knozinger (Editors), Advances in Catalysis, Vol 44, Vol. 44, Elsevier Academic Press Inc, San Diego, 1999, p. 329.

[189]   J. Pei and J.S.S. Zhang, Build. Environ., 48 (2012) 66.

[190]   O. Levenspiel, Chemical Reaction Engineering, 1999.

[191]   J. Benkhedda, J.N. Jaubert, D. Barth and L. Perrin, J. Chem. Eng. Data, 45 (2000) 650.

[192]   J.-H. Yun, D.-K. Choi and S.-H. Kim, Aiche J, 45 (1999) 751.

[193]   Y.-K. Ryu, H.-J. Lee, H.-K. Yoo and C.-H. Lee, Journal of Chemical & Engineering Data, 47 (2002) 1222.

[194]   M. Popescu, J.P. Joly, J. Carre and C. Danatoiu, Carbon, 41 (2003) 739.

[195]   J.Y. San, Y.C. Hsu and L.J. Wu, Int. J. Heat Mass Transf., 41 (1998) 3229.

[196]   J.-H. Yun, K.-Y. Hwang and D.-K. Choi, Journal of Chemical & Engineering Data, 43 (1998) 843.

[197]   J.A.G. Balanay, S.A. Crawford and C.T. Lungu, J. Occup. Environ. Hyg., 8 (2011) 573.

[198]   V. Gaur, A. Sharma and N. Verma, Chem. Eng. Process., 45 (2006) 1.

[199]   I. Langmuir, J. Am. Chem. Soc., 40 (1918) 1361.

[200]   M.M. Dubinin, Chemical Reviews, 60 (1960) 235.

[201]   M.M. Dubinin and H.F. Stoeckli, J. Colloid Interface Sci., 75 (1980) 34.

[202]   M.M. Dubinin, J. Colloid Interface Sci., 23 (1967) 487.

[203]   B.P. Bering, M.M. Dubinin and Serpinsk.Vv, J. Colloid Interface Sci., 21 (1966) 378.

[204]   M.C. Almazan-Almazan, M. Perez-Mendoza, I. Fernandez-Morales, M. Domingo-Garcia, F.J. Lopez-Garzon, A. Martinez-Alonso, F. Suarez-Garcia and J.M.D. Tascon, in S. Kaskel, P. Llewellyn, F. Rodriguez-Reinoso and N.A. Seaton (Editors), Characterisation of Porous Solids Viii, Royal Soc Chemistry, Cambridge, 2009, p. 159.

[205] M.F.R. Pereira, S.F. Soares, J.J.M. Órfão and J.L. Figueiredo, Carbon, 41 (2003) 811.

[206] K.S. Pitzer and D.W. Scott, J. Am. Chem. Soc., 65 (1943) 803.

[207] M.M. Dubinin, Carbon, 27 (1989) 457.

[208] J.F. Wu, M.E. Stromqvist, O. Claesson, I.E. Fangmark and L.G. Hammarstrom, Carbon, 40 (2002) 2587.

[209] D.D. Duong, Adsorption analysis : equilibria and kinetics, Imperial College Press, London, U.K., 1998.

[210] M.V. Roux, M. Temprado, J.S. Chickos and Y. Nagano, J. Phys. Chem. Ref. Data, 37 (2008) 1855.

[211] A.P. Terzyk, P.A. Gauden and P. Kowalczyk, Carbon, 40 (2002) 2879.

[212] N.D. Hutson and R.T. Yang, Adsorpt.-J. Int. Adsorpt. Soc., 3 (1997) 189.

[213] R.J. Cvetanović and Y. Amenomiya, in H.P. D.D. Eley and B.W. Paul (Editors), Advances in Catalysis, Vol. Volume 17, Academic Press, 1967, p. 103.

[214] W. Ait-Helal, A. Borbon, S. Sauvage, J.A. de Gouw, A. Colomb, V. Gros, F. Freutel, M. Crippa, C. Afif, U. Baltensperger, M. Beekmann, J.F. Doussin, R. Durand-Jolibois, I. Fronval, N. Grand, T. Leonardis, M. Lopez, V. Michoud, K. Miet, S. Perrier, A.S.H. Prevot, J. Schneider, G. Siour, P. Zapf and N. Locoge, Atmos. Chem. Phys., 14 (2014) 10439.

[215] M.P. Cal, M.J. Rood and S.M. Larson, Energy Fuels, 11 (1997) 311.

[216] L.A. Langley and D.H. Fairbrother, Carbon, 45 (2007) 47.

[217] C.L. Mangun, R.D. Braatz, J. Economy and A.J. Hall, Ind. Eng. Chem. Res., 38 (1999) 3499.

[218] H. Tamon and M. Okazaki, Carbon, 34 (1996) 741.

[219] I.I. Salame and T.J. Bandosz, Molecular Physics, 100 (2002) 2041.

[220] V. Fierro, V. Torne-Fernandez, D. Montane and A. Celzard, Microporous Mesoporous Mat., 111 (2008) 276.

[221] J.J. Pei and J.S.S. Zhang, Chem. Eng. J., 167 (2011) 59.

[222] H.Q. Rong, Z.Y. Ryu, J.T. Zheng and Y.L. Zhang, Carbon, 40 (2002) 2291.

[223] V. Boonamnuayvitaya, S. Sae-ung and W. Tanthapanichakoon, Sep. Purif. Technol., 42 (2005) 159.

[224]   H.Q. Rong, Z.Y. Ryu, J.T. Zheng and Y.L. Zhang, J. Colloid Interface Sci., 261 (2003) 207.

[225]   D.I. Kim, J.H. Park, S.D. Kim, J.Y. Lee, J.H. Yim, J.K. Jeon, S.H. Park and Y.K. Park, J. Ind. Eng. Chem., 17 (2011) 1.

[226]   K. Kaneko, K. Shimizu and T. Suzuki, J. Chem. Phys., 97 (1992) 8705.

[227]   E.M. Carter, L.E. Katz, G.E. Speitel and D. Ramirez, Environ. Sci. Technol., 45 (2011) 6498.

[228]   D.M. D'Alessandro, B. Smit and J.R. Long, Angew. Chem.-Int. Edit., 49 (2010) 6058.

[229]   S. Choi, J.H. Drese and C.W. Jones, ChemSusChem, 2 (2009) 796.

[230]   S. Couck, J.F.M. Denayer, G.V. Baron, T. Remy, J. Gascon and F. Kapteijn, J. Am. Chem. Soc., 131 (2009) 6326.

[231]   E. Lucas, S. Decker, A. Khaleel, A. Seitz, S. Fultz, A. Ponce, W.F. Li, C. Carnes and K.J. Klabunde, Chem.-Eur. J., 7 (2001) 2505.

[232]   F. Rodríguez-reinoso, Carbon, 36 (1998) 159.

[233]   E. Auer, A. Freund, J. Pietsch and T. Tacke, Applied Catalysis A: General, 173 (1998) 259.

[234]   J.C. Lavalley, Catal. Today, 27 (1996) 377.

[235]   G. Pacchioni, J.M. Ricart and F. Illas, J. Am. Chem. Soc., 116 (1994) 10152.

[236]   A. Auroux and A. Gervasini, J. Phys. Chem., 94 (1990) 6371.

[237]   M.G. Plaza, C. Pevida, A. Arenillas, F. Rubiera and J.J. Pis, Fuel, 86 (2007) 2204.

[238]   R. Kakkar, P.N. Kapoor and K.J. Klabunde, J. Phys. Chem. B, 110 (2006) 25941.

[239]   A. Corma and S. Iborra, in B.C. Gates and H. Knozinger (Editors), Advances in Catalysis, Vol 49, Vol. 49, Elsevier Academic Press Inc, San Diego, 2006, p. 239.

[240]   W.Q. Shen, G.A. Tompsett, R. Xing, W.C. Conner and G.W. Huber, J. Catal., 286 (2012) 248.

[241]   H. Tsuji, F. Yagi, H. Hattori and H. Kita, J. Catal., 148 (1994) 759.

[242]   A.M. Frey, S.K. Karmee, K.P. de Jong, J.H. Bitter and U. Hanefeld, ChemCatChem, 5 (2013) 594.

[243]   K. Tanabe and K. Saito, J. Catal., 35 (1974) 247.

[244]   T. Seki, H. Kabashima, K. Akutsu, H. Tachikawa and H. Hattori, J. Catal., 204 (2001) 393.

[245]   C. Baerlocher, L.B. McCusker, W.M. Meier, B. Olson, ebrary Inc. and International Zeolite Association. Structure Commission., Atlas of zeolite framework types, 6th rev. ed., Published on

behalf of the Structure Commission of the International Zeolite Association by Elsevier, Boston ; Amsterdam, 2007.

[246]   D. Barthomeuf, Materials Chemistry and Physics, 17 (1987) 49.

[247]   A. Corma, J. Catal., 216 (2003) 298.

[248]   N. Katada, H. Igi, J.H. Kim and M. Niwa, J. Phys. Chem. B, 101 (1997) 5969.

[249]   L. Rodriguez-Gonzalez, F. Hermes, M. Bertmer, E. Rodriguez-Castellon, A. Jimenez-Lopez and U. Simon, Appl. Catal. A-Gen., 328 (2007) 174.

[250]   B.L. Su and D. Barthomeuf, Appl. Catal. A-Gen., 124 (1995) 81.

[251]   J.N. Kondo and K. Domen, J. Mol. Catal. A-Chem., 199 (2003) 27.

[252]   X. Du and E. Wu, J. Phys. Chem. Solids, 68 (2007) 1692.

[253]   J. Datka, B. Gil and P. Baran, Journal of Molecular Structure, 645 (2003) 45.

[254]   A. Maijanen, E.G. Derouane and J.B. Nagy, Applied Surface Science, 75 (1994) 204.

[255]   M. Bevilacqua, T. Montanari, E. Finocchio and G. Busca, Catal. Today, 116 (2006) 132.

[256]   A. Janin, M. Maache, J.C. Lavalley, J.F. Joly, F. Raatz and N. Szydlowski, Zeolites, 11 (1991) 391.

[257]   S. Khabtou, T. Chevreau and J.C. Lavalley, Microporous Materials, 3 (1994) 133.

[258]   T. Barzetti, E. Selli, D. Moscotti and L. Forni, J. Chem. Soc.-Faraday Trans., 92 (1996) 1401.

[259]   F. Lonyi and J. Valyon, Thermochim. Acta, 373 (2001) 53.

[260]   S.H. Li, A.M. Zheng, Y.C. Su, H.L. Zhang, L. Chen, J. Yang, C.H. Ye and F. Deng, J. Am. Chem. Soc., 129 (2007) 11161.

[261]   G.L. Woolery, G.H. Kuehl, H.C. Timken, A.W. Chester and J.C. Vartuli, Zeolites, 19 (1997) 288.

[262]   B. Louis, S. Walspurger and J. Sommer, Catal. Lett., 93 (2004) 81.

[263]   R.J. Gorte and D. White, Top. Catal., 4 (1997) 57.

[264]   S. Jakobtorweihen, N. Hansen and F.J. Keil, Molecular Physics, 103 (2005) 471.

[265]   V. Majer and V. Svoboda (Editors), Enthalpies of vaporization of organic compounds : a critical review and data compilation, Blackwell Scientific Publ., Oxford ; Boston etc., 1985.

[266]   G.O. Wood, Carbon, 39 (2001) 343.

[267]   F. Eder and J.A. Lercher, Zeolites, 18 (1997) 75.

[268]   T.J.H. Vlugt, R. Krishna and B. Smit, The Journal of Physical Chemistry B, 103 (1999) 1102.

[269]   L. Fournel, P. Mocho, R. Brown and P. Le Cloirec, Adsorpt.-J. Int. Adsorpt. Soc., 16 (2010) 147.

[270]   T.B. Cheng, Y. Jiang, Y.P. Zhang and S.Q. Liu, Carbon, 42 (2004) 3081.

11 Curriculum Vitae

Education

2011 - *2015*   EPFL PhD in chemical engineering

2009 - 2011   EPFL Master in chemical and biochemical engineering
Master project in UC Berkeley (California, USA)

2006 - 2009   EPFL Bachelor of science in chemistry

2003 - 2006   Gymnase de Nyon, Maturity in chemistry and biology. Complementary option sport

Work experiments

2010   Tamoil Suisse SA: Process engineer in diesel production (5 months internship)
Optimization of a diesel synthesis unit leading to 15% increase in production capacity. Day-to-day unit management.

2008 - 2010   EPFL: Student assistant for general chemistry lesson

2004 - 2008   Rolex SA, Genève: (summer internships)
Assembly and stock inventory on a production line.

Projects

Cigarette filters development for toxic smoke compounds removal

- PhD thesis project supported by Phillip Morris International.
- Designed and built experimental setup reproducing cigarette filters conditions for **realistic smoke constituent removal**.
- Development and testing of innovative activated carbon based material for cigarette filters. **90% reduction of selected smoke constituents** in lab scale experiments.
- The novel developed filters were **tested in real cigarettes** achieving **50% smoke constituent removal**.

- Scale-up process under development for future process industrialization. Considerable **business opportunities for tobacco industry**.
- Supervision of **two master projects.**

Natural gas to gasoline conversion

- Master project supported by BP USA.
- Development of a solid catalyst for gas phase transformation of **natural gas to gasoline**.
- Successful conversion of natural gas to gasoline obtained by **combining nickel and zeolites**.
- Business opportunities for large scale industrialization process. Possible implementation to a refinery.

Publications

- Anton N. Mlinar, Guillaume B. Baur, Gerry G. Bong, Andrew Getsoian, Alexis T. Bell. *Propene oligomerization over Ni-exchanged Na-X zeolites*. Journal of Catalysis 296, 2012, 156-164.
- Guillaume B. Baur, Igor Yuranov, Lioubov Kiwi-Minsker. *Activated carbon fibers modified by metal oxide as effective structured adsorbents for acetaldehyde*. Catalysis Today 249, 2015, 252-258.
- Guillaume B. Baur, Oliver Beswick, Jonathan Spring, Igor Yuranov, Lioubov Kiwi-Minsker. *Activated carbon fibers for efficient VOC removal from diluted streams: the role of surface functionalities*. Adsorption-Journal of the International Adsorption Society 21, 2015, 255-264.
- Guillaume B. Baur, Igor Yuranov, Albert Renken, Lioubov Kiwi-Minsker. *Activated carbon fibers for efficient VOC removal from diluted streams: the role of surface morphology*. Adsorption-Journal of the International Adsorption Society (in press).
- Guillaume B. Baur, Florent Héroguel, Jonathan Spring, Jeremy S. Luterbacher, Lioubov Kiwi-Minsker. *Zeolite as an efficient adsorbent for diluted butadiene*. (under preparation)
- Guillaume B. Baur, Florent Héroguel, Jonathan Spring, Jeremy S. Luterbacher, Lioubov Kiwi-Minsker. *Formaldehyde removal on amine modified activated carbon fibers*. (Under preparation)

Conferences

- SCS Fall meeting 2012, September 2012. Zurich, Switzerland. Guillaume B. Baur, Oliver A. Beswick, Micaela Crespo-Quesada, Igor Yuranov, Lioubov Kiwi-Minsker. *Activated carbon fibers as effective adsorbent for VOCs removal.*

- European Summerschool, June 2013. Rolduc Abbey, the Netherlands. Guillaume B. Baur, Igor Yuranov, Lioubov Kiwi-Minsker. *Activated carbon fibers as efficient sorbent for oxygenated VOCs removal.*
- Carbocat VI. June 2014. Trondheim, Norway. *Metal oxide modified activated carbon fibers as efficient structured adsorbent for VOCs removal.*
- SCS Fall meeting 2014, September 2012. Zurich, Switzerland. *Activated carbon fibers as efficient structured adsorbent for VOCs removal.*

Languages

French   Native speaker

English   Fluent
      Master project and PhD thesis in English
German   High school level

Extra professional activities

- Playing football since 1995 at competitive level (2-4$^{\text{ème}}$ ligue)
- Challenge 2010: ski challenge between EPFL and ETHZ
  Logistic manager in the Challenge 2010 committee. *Event joining 350 people. Budget 200 000 CHF.*
- Baramine 2009: collecting of money for a study trip

Prizes and awards

- EPFL teaching awards 2014 for the management of lab projects for 45 students with 12 teaching assistants and the supervision of two master thesis